Paleopole Investigation of Martian Magnetic Field Anomalies

vorgelegt von
Diplomgeophysiker
Paul Thomas
ORCID: 0000-0001-6884-6422

Von der Fakultät II - Mathematik und Naturwissenschaften
der Technischen Universität Berlin
zur Erlangung des akademischen Grades

Doktor der Naturwissenschaften
-Dr. rer. nat.-

genehmigte Dissertation

Promotionsausschuss:

Vorsitzender: Prof. Dr. Mario Dähne
Gutachter: Prof. Dr. Dieter Breitschwerdt
Gutachter: Dr. Nicola Tosi
Gutachter: Prof. Dr. Uwe Motschmann

Tag der wissenschaftlichen Aussprache: 29.04.2019

Berlin 2019

If Mars formed life, then life on Earth could have been seeded by life on Mars, making every life form on Earth descended from Martians.
-Neil deGrasse Tyson-

Ever since the start of the space era, magnetometer carrying spacecrafts were sent to measure the magnetic fields of the Earth and other terrestrial planets in the solar system. The first attempt to measure the magnetic field of Mars was during the flyby of the Mariner 4 spacecraft and it was concluded that unlike Earth a current core dynamo is absent. Even though magnetometer carrying spacecrafts approached Mars in the following decades, it was not until 1997 that the Mars Global Surveyor (MGS) mission discovered a strong remanent magnetic field originating from the Martian crust. Ever since, the results of MGS were integrated in local and global magnetic field models, which were eventually used for paleopole reconstruction. By comparing all paleopole investigations since the year 2001 it was revealed that determined paleopole locations are widely spread all over the Martian surface and it was therefore an objective of this study to find the reason for the spread and give an estimate of uncertainty for paleopole locations on Mars. From synthetic tests, as well as tests on real data, it can be concluded that perturbation in the measured magnetic signal causes residuals in the determined paleopole location, which explains the spread found in earlier studies. Eight Martian magnetic field anomalies were investigated in detail and the determined areas of admissible paleopole locations show a mean surface coverage of 35.5%. These areas constrain paleopole locations to either the northern or southern hemisphere as well as an area in the mid-latitudes. It could therefore be concluded that Mars underwent at least one polar reversal and an event of true polar wander in its past.

Mit Beginn der Raumfahrt war es möglich magnetische Messungen im Orbit der Erde und anderer terrestrischer Planeten durchzuführen. Durch Einsatz der Mariner 4 Sonde wurde zum ersten Mal während eines Vorbeiflugs versucht das Magnetfeld des Mars zu messen. Jedoch konnte das an Bord befindliche Magnetometer kein signifikantes Magnetfeld detektieren. Dies führte zu dem Schluss, dass der Planet Mars zum momentanen Zeitpunkt keinen Dynamo in seinem Kern aufrecht erhalten kann. Der Mariner 4 Sonde folgten weitere Missionen, doch es dauerte bis zum Jahr 1997 bis die Mars Global Surveyor (MGS) Sonde ihre Mission im Orbit des Mars antrat und ein deutliches Magnetfeld detektierte, dessen Ursprung in der Kruste des Planeten liegt. Die gewonnenen Daten wurden für die Erstellung von lokalen und globalen Magnetfeldmodellen genutzt, welche wiederum dazu dienten die Positionen von magnetischen Paläopolen zu bestimmen. Die Analyse der seit dem Jahr 2001 durchgeführten Untersuchungen zeigte, dass sich die errechneten Paläopolpositionen kaum auf einen definierten Bereich auf der Marsoberfläche einschränken lassen. Das Ziel dieser Arbeit ist es die Ursachen der weiträumigen Verteilung der Paläopole zu untersuchen und ein Maß für die mögliche Streuung von Paläopolpositionen zu definieren. Hierzu wurden synthetische Magnetfeldanomalien erzeugt, sowie reale Anomalien des Mars untersucht, welche zu dem Ergebnis führten, dass die weiträumige Verteilung durch die Überlagerung von Magnetfeldsignalen hervorgerufen wird und das Ausmaß der jeweiligen Signalveränderung abgeschätzt werden muss. Im Detail wurden acht Magnetfeldanomalien des Mars untersucht und für jede Anomalie konnte ein Bereich erlaubter Paläopolpositionen (area of admissible paleopole locations) definiert werden. Im Mittel bedecken die errechnteten Bereiche 35,5% der Marsoberfläche, wodurch Paläopolpositionen auf die nördliche und südliche Hemisphäre, sowie auf einen Bereich mittlerer Breite beschränkt werden können. Die Verteilung von Paläopolpositionen lässt den Schluss zu, dass in der Vergangenheit des Mars mindestens eine Polumkehr (polar reversal), sowie eine ausgeprägte Polwanderung (true polar wander) stattgefunden haben muss.

PUBLICATIONS

A part of this work was published in the Journal of Geophysical Research (Planets):

Thomas, P., M. Grott, A. Morschhauser, and F. Vervelidou (2018).
"Paleopole reconstruction of Martian magnetic field anomalies."
J. Geophys. Res.: Planets 123. doi: 10.002/2017JE005511.

ACKNOWLEDGEMENTS

First of all I would like to thank my family for giving me the possibility to study and supported me throughout school, university and my time as a PhD student.

A big thank you goes out to my great colleagues at the German Aerospace center and the head of the departement of Planetary Physics, Prof. Doris Breuer. Two of my colleagues I would like to mention here are Dr. Tina Rückriemen-Bez and Maximilian Hamm, who were not only colleagues but became good friends over the past years. We shared nice lunch breaks and business trips together, which I will sadly miss in the future. Probably my biggest gratitude goes out to Dr. Matthias Grott, who first of all gave me the opportunity to work at the DLR and helped me with my research, my publications and with the writing of this thesis. I thank him for his patience, time and his kind personality as well as his knowledge of which I and my thesis could benefit from. Furthermore, I would like to thank Dr. Nicola Tosi as a colleague and moreover for his advice and his dedication to my PhD thesis at the TU-Berlin. Also I would like to thank Dr. Frank Sohl with whom I had the chance to start a project, even though we were not able to finish it at the end. Thank you Frank for your enthusiasm and your commitment.

I would further like to thank Dr. Achim Morschhauser and Dr. Foteini Vervelidou from the GFZ in Potsdam for their constructive help and interesting meetings we had in the past three years. Especially, I thank Dr. Morschhauser for his many helpful advices and his spherical harmonic model without which my thesis would not have been possible.

I also would like to thank André Miede for providing the classicthesis template for LaTeX, which was used to typeset this thesis.

Last but not least I would like to thank my wonderful wife Nele. You are my partner in crime, my best friend and without you this work would have been much harder. Thank you for the previous years we have been together and for the years that stand before us, in particular with our baby boy Alvar.

– Alvar this one is for you. May you witness the first human setting foot on Mars. –

CONTENTS

Part I

MAGNETIC FIELD PROPERTIES

In the following two chapters an overview of the origin and characteristics of magnetic fields specific for the examples of Earth and Mars are given in combination with a presentation of former paleopole investigations for Mars in the first chapter. The second chapter has its focus on how the magnetic field data from Mars has been acquired and processed and further depicts the characteristics of the Martian magnetic field.

1 OVERVIEW

The planet we live on provides the best observable magnetic field in the solar system. From its observation in combination with other data sets a solid understanding of the processes which generate and preserve magnetic fields was achieved. The models and constraints for Earth are used to derive information about other planets such as Mars. In this chapter the common theory for generating a global dynamo is introduced and it is explained how secondary magnetic fields are generated within the atmosphere and inside the lithosphere. In the end of this chapter the principles for paleopole reconstruction are introduced and former investigations are presented.

1.1 INTRODUCTION

From the earliest magnetic field investigations for navigational purposes, magnetic field instruments are now commonly applied for terrestrial resource exploration, or for investigating planetary magnetic fields. Small scale, or large scale investigations can likewise reveal important information about historical features of the observed magnetic field and conclusions on the interior and dynamic of a planet are possible. The most basic investigation is the determination of the magnetic North or South Pole, e.g. for navigating ships. The magnetic pole locations are points where the magnetic inclination reaches a dip of $\pm 90°$ (Garland, 1979). Earth's main magnetic field is predominantly dipolar and therefore only two locations with inclinations of $\pm 90°$ remain when the magnetic field is observed from a distance. The present magnetic pole location varies $\sim 11.4°$ from the rotational axis and has continuously moved in the past. These so called polar excursions can be reconstructed in time by analysing the magnetization of seamounts, continental volcanoes or rock samples and determined former magnetic pole locations are denoted paleopoles.

Due to the appearance of continental drift on Earth the plate movements have to be substracted to reconstruct the actual pole location. Prior to the acceptance of the theory of plate tectonics it was debated that some sort of true polar wander (TPW) must have happend, where the whole Earth has moved relative to its rotational axis (Garland, 1979). The reconstruction of the plate movements lead to similar paleopole locations from different observations and TPW seemed as an implausible explanation. However, for other terrestrial planets TPW events, due to mass redistributions are a possible scenario and must therefore be investigated (Sec. 1.4).

During the investigation of paleopole locations it was further observed that some samples show an opposite magnetic orientation to the present days main magnetic field and it was concluded that the magnetic North and South Pole must have switched in the past. Further investigations, especially of the magnetization of oceanic crust revealed that these polar reversals (PRs) are recurrent events on Earth (Sec. 1.2.1) and the observed samples hold information on the appearance and periodicity of these events and can therefore help to understand the behavior of the magnetic field generating dynamo.

The comprehensive determination of extraterrestrial magnetic fields is currently constrained to orbital observations and therefore lacks the resolution achieved on Earth,

which strongly depends on the distance between magnetic source and instrument. The first attempt to measure the Martian magnetic field was made by the Mariner 4 spacecraft in 1965. The majority of people might have been disappointed about pictures taken by the on board cameras, revealing a hostile, Moon like landscape, but the fact that no significant magnetic field was measured is of great importance, because without a main magnetic field there is no protection from the solar wind.

Even though magnetometer carrying spacecrafts approached Mars in the following decades it was not until 1997 that the strong remanent magnetic field originating from the Martian crust was identified by the "Mars Global Surveyor" (MGS) mission. The MGS spacecraft operated for nine years and provided magnetic field data with the best spatial resolution until 2014, when the "Mars Atmosphere and Volatile EvolutioN" (MAVEN) mission arrived at Mars. The information gathered was used to create local and global models of the magnetic field in order to increase the resolution and interpolate for missing data. The magnetic field models as well as the track data itself were further used for specific investigations of Martian magnetic field anomalies, e.g. to reconstruct paleopole locations of the former core field. The earliest investigations from 2001 concluded that the Martian paleopole locations were altered by polar reversals (PR) and true polar wander (TPW). In the following years more investigations followed, commonly assuming that either TPW, PR or both appeared. The comparison of results predating 2016 show a wide spread of paleopole locations across the Martian surface (Sec. 1.4). Therefore, it was of great interest to verify the robustness of given results and investigate possible reasons for their wide spread. For this purpose synthetic tests (Sec. 4) were performed in order to determine the impact of field alterations on the observed magnetic field, prior to additional paleopole investigations.

For the current paleopole investigation the most precise global Martian magnetic field model to date was chosen as input. It is a regularized spherical harmonic (SH) model up to degree and order 110, with a low noise level and robustness when being downward continued to the surface. It holds the opportunity to investigate the magnetic field at locations not covered by the orbital tracks and for example generate equally distributed observation points over a distinct area. Using the SH-model a global magnetic field map was generated and used to identify magnetic anomalies for local magnetic field investigations (Sec. 5.1 / 5.6) and the determination of magnetic orientations, as well as corresponding paleopole locations (Sec. 5.2 / 5.6).

Within this study eight Martian magnetic field anomalies were chosen for detailed investigation (Sec. 5.1 / 5.6). After the reconstruction of paleopole locations using the SH-model, the investigation was later applied on the track data of MGS (Sec. 5.4.2) and the new data from the MAVEN mission (Sec. 5.4.4).

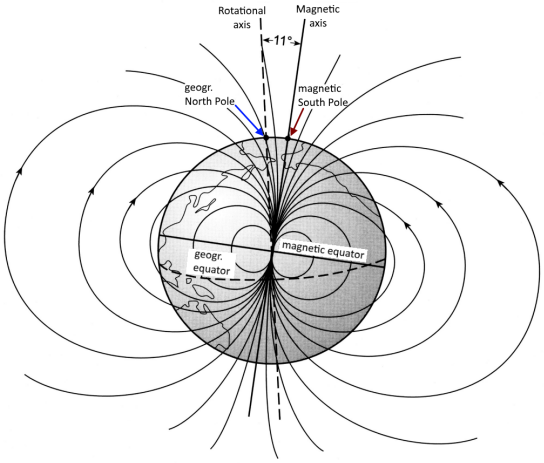

Figure 1: Sketch of Earth's main magnetic field represented by a perfect dipole field originating from the center of the planet (after Berckhemer (1997)). The magnetic poles are in opposing orientation to the geographic poles, with magnetic south being ~ 11° apart from geographic north.

1.2 PLANETARY MAGNETIC FIELDS

The observation of planetary magnetic fields are in general a combination of measurements of different magnetic sources and processes. The Earth's magnetic field for example has three major magnetic sources, which can roughly be separated into the main, crustal, and the ionospheric magnetic field (Telford et al., 1990). To be more specific these sources are a self-sustaining dynamo, remanent and induced magnetizations in rocks, as well as magnetospheric currents. The latter can not only be found in the ionosphere of Earth, Mars, or Venus, but also in the saltwater Oceans of the moons Europa, Ganymede and Callisto (Spohn et al., 2014).

1.2.1 *Origin of the main magnetic field*

Earth's main magnetic field contributes around 99% to the measured signal and influences the crustal and ionospheric field. It has a long wavelength with predominantly dipole characteristics and originates from dynamo processes in the core (Lowrie, 2007; Spohn et al., 2014; Telford et al., 1990). The best representation of Earth's dynamo is the canonical planetary dynamo, which is defined by a solid inner core surrounded by fluid motions in an electrical conducting spherical shell (Spohn et al., 2014). The outer core consists of mainly iron and nickel in fluid phase and its material is moved by buoyancy differences due to an unstable thermal stratification during the cooling process. Further buoyancy is generated by radiogenic heat sources, compositional convection and the release of light element-rich fluid at the base of the liquid core during the inner cores freeze-out (Spohn et al., 2014). The buoyancy in combination with helical and differential flows, as well as an initial magnetic field, such as toroidal or poloidal fields, creates a dynamo which can be self-sustaining if the flows are capable to regenerate the initial magnetic field. In a picturesque analog those currents are similar to electromagnetic coils, generating a dipole field with a magnetic North and South Pole (Fig. 1).

On Earth the main magnetic field has a magnitude of around 50.000 nT at the surface and the dipole axis alignment varies only 11.4° from the rotational axis. Therefore, the magnetic inclination and latitude are strongly related, with an inclination of around $\pm 90°$ at the poles and 0° inclination at the equator. The field undergoes sporadically appearing

polar reversals roughly every 0.5 Ma and further shows a pole movement of around $10\frac{\mathrm{km}}{\mathrm{a}}$ (Lowrie, 2007; Spohn et al., 2014). These pole variations are often the target of paleomagnetic investigations (Lowrie, 2007; Telford et al., 1990), e.g. during polarity investigations of the oceanic crust.

In comparison, planet Mars currently has no main magnetic field, but the observed crustal magnetic field suggests that an active dynamo was present in its past (Acuña et al., 1999). This ancient dynamo of Mars generated a field strength comparable to the Earth's field (Gubbins and Herrero-Bervera, 2007; Lillis et al., 2013) between 5 and 50.000 nT (Weiss et al., 2002). After Acuña et al. (1999), Connerney et al. (2001) and Lillis et al. (2013) the intensity of the observed magnetic field is only possible with large volumes of coherently magnetized regions within fields with periods of uniform magnetization which last at least 1 Ma (Dietrich and Wicht, 2013). Due to the dichotomy in the Martian magnetic field (Sec. 2.2) and its unknown origin it was conversely suggested by Stanley et al. (2008) that unlike Earth, the Martian magnetic dynamo could have been constrained only to the southern hemisphere of the planet. A dynamo model by Dietrich and Wicht (2013) suggests that a single hemisphere dynamo would undergo oscillations with reversal periods of 0.01 Ma. Assuming that a single hemisphere dynamo might not be capable to generate the strong remanent magnetization found on Mars it is a reasonable assumption that the ancient dynamo was similar to Earth a global dynamo (Dietrich and Wicht, 2013), with the difference, that the Martian dynamo deceased in the early stage of the planetary evolution, prior to 4.1 Ga (Lillis et al., 2013; Vervelidou et al., 2017b). Paleopole investigations can possibly give an estimate on the periodicity of polar reversal events and might clarify if these events appeared at intervals of 0.01 or 1 Ma (Sec. 1.4).

1.2.2 *The ionospheric magnetic field*

The sun permanently emits ultraviolet and X-ray radiation as well as charged particles in form of, e.g. ions and electrons (Meschede, 2005). These emissions come in contact with the upper atmospheres of terrestrial planets. Eventually the sun's plasma can be trapped and more plasma is generated by ionization processes caused by the radiation. The free electrons and ions create a highly conductive layer which moves due to diurnal temperature changes and tidal forces, generating a magnetic field. These daily magnetic field variations depend on latitude, season, time of day and the sun's activity. For example on Earth at around 50° N the Down-component of the magnetic field shows a daily variation of -10 nT to -40 nT (Berckhemer, 1997). The daily drift is further altered by less than 10 min lasting pulsations and variations of more than 10 min (Kertz, 1985). The surface magnetic fields are usually not influenced and the change in the ionospheric field can be neglected for surface observations. This is not the case for orbital magnetic field observations. During periods of high sun activity magnetic storms can appear, forcing field alterations of up to 3 μT in the Earth's field and therefore changing the measured field at surface altitude as well (Meschede, 2005). Even though Mars has a thin atmosphere, with $\sim$ 7 mbar at the surface (Spohn et al., 2014), and is at greater distance to the sun, ionospheric magnetic fields with an intensity of 40 nT were detected (Connerney et al., 2015a). At an altitude of around 300 km the field varies from 20 nT to 40 nT in between the terminator and near the subsolar point, respectively (Akalin et al., 2010). The ionospheric field is of the same order as the detected crustal field at that altitude and great care should be taken when this data is used for investigation of the lithospheric magnetic field.

1.2.3 *The lithosphere's magnetic field*

Magnetization of matter

On an atomic scale all substances are magnetic, because every electrical charge is capable to generate a magnetic field (Meschede, 2005; Tarling, 2007). As an example electrons move in orbitals and spin, which eventually generates a magnetic field (Kopitzki, 1989; Tarling, 2007).

Within solid matter, every crystal consists of a crystal grating in the shape of an ordered network of atoms, where exchange forces always have a structure relative to the grating. Every grating allocates "easy" axes (Tarling, 2007) on which a magnetization is easier performed. Crystals form grains and the size and composition of a grain controls the energy necessary to perform direction changes in dependence of the easy axes. Small crystal grains with homogeneous composition change direction more easily, whereby in larger grains magnetic alignment appears parallel or anti-parallel to the easy axes and magnetostatic forces are increased as two poles on the surface of the grain. A large grain can therefore form a magnetized volume element of the matter called "domain". Within such a domain the electron spins are coupled and neighboring domains mutually interact, reducing the magnetostatic forces. The domain walls (Bloch walls) are directly linked to imperfections of the crystal grating, especially at the surface of a grain (Tarling, 2007).

An observed particle can be single domain, where two poles on the surface appear, or multidomain, where various spin orientations are present in the different sub-domains. If a multidomain particle is exposed to an external magnetic field, domain walls of subdomains which are aligned to the magnetic field eventually unroll and their volumes increase. If the external field is weak and the temperature is constant, the domain walls are relocated to their original places at the time of field removal. For strong fields, the domain walls exceed the energy boundaries defined by the crystal grating impurities and domain walls might retain at their new locations, after the field has vanished, leading to remanent magnetization.

The energy to overcome the internal barriers can as well be achieved under weak field conditions, due to the addition of energy from thermal vibrations. Thermal vibration is always present for temperatures above 0 K and hence some electrons will have sufficient energy to overcome the internal barriers (Tarling, 2007). Given enough time, eventually all electrons will pass the barriers and the domain walls remain in place after the field removal. In general this is an unrealistic scenario, because the necessary time highly exceeds the period of a natural constant external field.

However, temperature is in fact just a statistical measure of thermal vibrations (Tarling, 2007), therefore, increasing the temperature allows for more electrons to pass the internal barriers in a certain amount of time and potentially leading to a remanent magnetization. The applied temperature and the volume of the domain further control the specific relaxation time of the domain and its preserved magnetization. The relaxation time describes the time it takes for the domain to acquire a magnetization with a component in the direction of the external field. Domains of low relaxation time will orient along new field orientations faster than domains with high relaxation time. It is calculated as follows (Tarling, 2007):

$$\tau = \frac{1}{c} exp\left(\frac{v\kappa}{kT}\right) = \frac{1}{c} exp\left(\frac{vH_a M_s}{2kT}\right) \tag{1.2.1}$$

With $c \propto 10^{10} \frac{1}{s}$ as the frequency factor, v as the volume of the domain, H_a the anisotropy of the field, M_s the saturation magnetization, κ the anisotropy constant, k as the Boltz-

mann constant, and T defining the absolute temperature. From Eq. 1.2.1 it follows that the relaxation time mainly depends on the volume of the domain and the temperature $\log\tau \propto \frac{v}{T}$. Leading to the conclusion that a single domain particle of constant volume will obtain a logarithmic increase in its relaxation time while cooling, or while the particle grows at constant temperature. These two scenarios can either appear in form of thermo-remanent magnetization (TRM), or chemical-remanent magnetization (CRM), respectively. This gives rise to an issue regarding the age analysis of remanent magnetization. A possible secondary magnetization can arise, having a higher stability than the primary magnetization, due to crystal growth at constant temperature and maybe increasing coercivity. Furthermore, parts with low relaxation time are continuously influenced if they are placed within an ambient magnetic field, leading to a viscous magnetization which is different from the original magnetization. If the majority of the material has low relaxation times, then a remanence dominated by viscous components might pursue and measurements could be biased.

However, the early decease of the Martian dynamo suggests that only magnetization with high stability (high relaxation time and high coercivity), likely preserved by single domain particles, remain today (Dunlop and Arkani-Hamed, 2005).

Crustal magnetization

Due to interactions of the long wave main magnetic field with magnetizable minerals in the crust, crustal magnetic fields of shorter wavelengths are generated. When a core field is still present, this field consists of the induced crustal field M_I and remanent crustal magnetization M_r which can be linked with the Koenigsberger ratio $Q = \frac{M_r}{M_I}$ (Blakely, 1996; Garland, 1979). An existing magnetic field can be preserved as remanent magnetization if magnetizable minerals are influenced during petrogenetic processses, or during alteration processes. Magnetizable materials are differentiated in 5 categories. The first three, diamagnetic materials, paramagnetic, and antiferromagnetic materials, interact with an inducing field but vanish when the field deceases, or only retain weak magnetization (Meschede, 2005). The remaining two material categories have the ability to generate and preserve the strongest magnetizations. They are called ferromagnetic and ferrimagnetic materials. Their susceptibility χ is larger than 0, leading to a magnetic orientation which is aligned with the inducing field, but the strength of magnetization depends on the strength of the inducing field and already existing magnetization of the material. Ferromagnetic materials are able to preserve the induced field as remanent magnetization (M_r) and the preserved magnetization persists when the inducing field changes. Its magnetization process is visualized through the hysteresis curve (Fig. 2).

Fig. 2 shows the increasing magnetization M in an unmagnetized material within an increasing magnetic field H. It can be seen that M has an upper boundary, defined by the saturation magnetization M_s. If the inducing field is reduced, the magnetization decreases, but the ferromagnet preserves a remanent magnetization M_r (Gubbins and Herrero-Bervera, 2007; Meschede, 2005). Ferrimagnetic materials are similar to ferromagnetics, but the possible M_s is smaller and not all of the magnetic moments inside the material are uniformly aligned. Therefore, the overall strength of magnetization is smaller.

Ferro-, or ferrimagnetic materials only exist in the solid phase. Furthermore, the remanent magnetization is lost even before a change in the aggregate phase is reached. The boundary is set by the Curie-temperature (T_c) (Gubbins and Herrero-Bervera, 2007; Meschede, 2005) for ferro- and ferrimagnetic materials and by the Néel temperature (T_N) for the not further discussed antifferomagnetic materials.

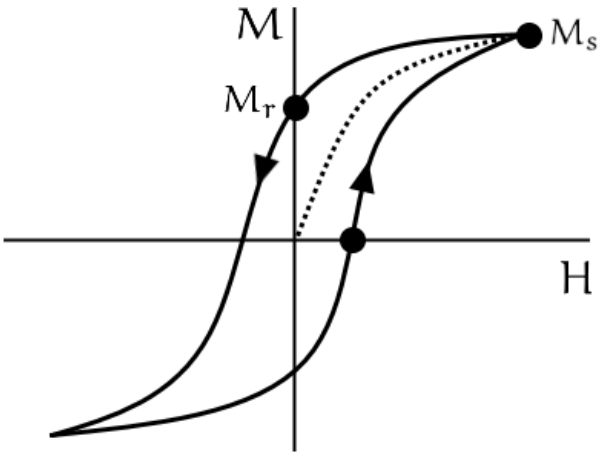

Figure 2: This diagram shows an idealized hysteresis curvature for a magnetization process, with the magnetic field H on the abscissa and the magnetization M on the ordinate. Arrows indicate the increase and decrease of magnetization with M_s indicating the point of saturation and M_r the preserved remanent magnetization.

Material of remanent magnetization can be further distinguished depending on the petrogenetic processes forming them. The most common processes are TRM (thermo-remanent magnetization), CRM (chemical-remanent magnetization), DRM (detrital-, or depositional-remanent magnetization), and SRM (shock-remanent magnetization) (Gubbins and Herrero-Bervera, 2007; Lowrie, 2007; Telford et al., 1990). The strongest magnetic fields are preserved within sources formed due to TRM. It specifies the preservation of magnetization due to temperature variations, where a heated material ($T \geqslant T_c$) surrounded by an inducing magnetic field is cooled down below T_c. A good example for TRM can be observed at mid ocean ridges on Earth. The continuously erupting lava at the diverging plates has susceptibilities of $0 \leqslant \chi \leqslant 14.5 \cdot 10^{-3}$ (Jacobshagen et al., 2000) and preserves the magnetization of the main magnetic field. It is a catalogue of Earth's polar reversal events for the last 180 Ma (Spohn et al., 2014). On smaller scales TRM also exists in volcanic systems, such as magma chambers, volcanoes and solidified lava flows and even in antropogenous products like bricks, or pottery. TRM can therefore be assumed on terrestrial planets with deceased or ongoing volcanic activity and an existing, or former main magnetic field.

This is the case for the Martian magnetic field (Acuña et al., 1999). The Martian dynamo shut down 4.1 Ga ago (Lillis et al., 2013; Vervelidou et al., 2017b) and with the absence of a core field the strongest magnetization remains within the crust (Sec. 2.2). The crustal field is mainly spread over the southern hemisphere, following the Martian dichotomy. In the region of Terra Cimmeria and Terra Sirenum the magnetic field reaches ~ 12000 nT at surface. In comparison, the Northern Lowlands (Fig. 10 / App. B) are nearly free of crustal magnetization. These specific features could be observed in the MGS data (Acuña et al., 1999), the subsequent models, e.g. Arkani-Hamed (2001a), Morschhauser et al. (2014), as well as in the recent data from the MAVEN spacecraft (see Sec. 2.2.1, 2.2.2).

The strongest magnetization in the Martian crust is probably carried by FeTi-oxides like titanohematites and titanomagnetites, whereby magnetites are more likely, because hematite was not rated as primary mineral in the Martian meteorites (Rochette et al., 2005). Additionally, a single domain magnetite has a high Curie-temperature ($T_c = 580°C$) and therefore could preserve magnetization down to a crustal thickness of 50 km (Dunlop and Arkani-Hamed, 2005). In comparison, a monoclinic pyrrhotite, which has been discovered

in Martian meteorites as well (Weiss et al., 2002) destabilizes at around $T_c = 260°C$ and would only allow magnetization down to ~ 9 km depth (Gubbins and Herrero-Bervera, 2007).

1.3 PALEOPOLE RECONSTRUCTION

Under the assumption that the observed remanent magnetization was preserved under the influence of a global magnetic field of dipolar character, a paleopole location (P) can be calculated from the location of the source of magnetization (S) in longitude Φ_s, and latitude λ_s, in combination with the source's magnetic orientation in inclination I_m and declination D_m (Fig. 3 / Butler, 1992). I_m and D_m are hereby defined as $-90° \leqslant I_m \leqslant 90°$ and $0° \leqslant D_m \leqslant 360°$.

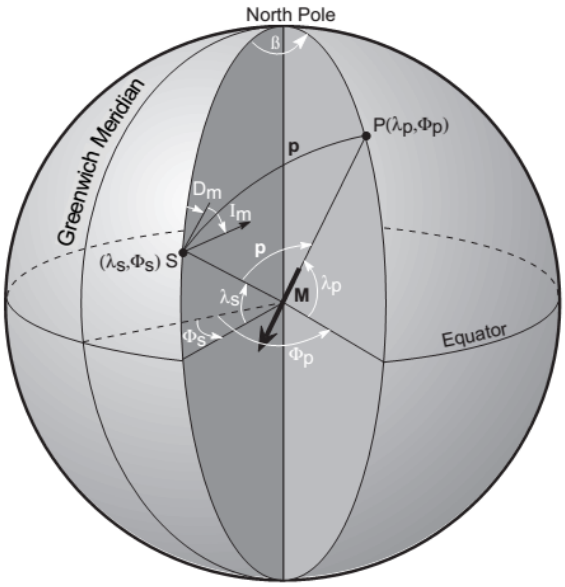

Figure 3: Parameter dependencies to determine the latitude Φ_p and longitude λ_p of a paleopole location P from a given magnetic orientation (I_m / D_m) at site S located at latitude Φ_s and longitude λ_s. **M** is the idealized geocentric dipole, p is the great circle distance, and β is the longitudinal difference between the source and paleopole location (Butler, 1992).

From the potential of a magnetic field on a sphere it follows that the inclination and colatitude can be related (Garland, 1979). This colatitude is indifferent to $90° - \lambda_s$ and is further called the magnetic colatitude p (Fig. 3), or the great circle distance between the source location and the paleopole position, which can be determined by

$$p = \tan^{-1}\left(\frac{2}{\tan(I_m)}\right) \tag{1.3.1}$$

Here it is important to notice that negative values of p must be handled by the addition of 180°. This avoids false accumulation of paleopole locations, due to the fact that inverse function of the tangens will only give values of p for on half of the spherical shell. Given the magnetic colatitude p, the paleopole latitude can be calculated according to

$$\Phi_p = \sin^{-1}\left[\sin(\Phi_s)\cos(p) + \cos(\Phi_s)\sin(p)\cos(D_m)\right] \tag{1.3.2}$$

Next, the longitudinal difference β between the source and paleopole location is calculated,

$$\beta = \sin^{-1}\left(\frac{\sin(p)\sin(D_m)}{\cos(\Phi_p)}\right) \tag{1.3.3}$$

and it needs to be distinguished between two cases for the paleopole longitude λ_p:

1. if $\cos(p) \geqslant \sin(\Phi_s)\sin(\Phi_p)$, then:

$$\lambda_p = \lambda_s + \beta \tag{1.3.4}$$

2. if $\cos(p) < \sin(\Phi_s)\sin(\Phi_p)$, then:

$$\lambda_p = \lambda_s + 180° - \beta \tag{1.3.5}$$

Φ_p and λ_p then represent the longitude and latitude of the paleomagnetic South Pole location (Fig. 3).

1.4 PALEOPOLE STUDIES

As presented in Sec. 1.2.3 a magnetic field can be preserved as remanent magnetization within magnetizable material. By the time magnetic field instruments became sensitive enough for detailed observations it was soon observed that some measured fields of crustal origin are oriented in the opposing direction to the main field. Due to the fact that many rocks do not have the mineralogical composition to enable self-reversal (Garland, 1979; Tarling, 2007) it was concluded that a full reversal of the global magnetic field must have happened. With the possibility to determine the age of a magnetized rock by methods of geochronology it is now well known that the Earth's magnetic field undergoes a 180° change in orientation at geologically frequent, but irregular intervals (Garland, 1979; Gubbins and Herrero-Bervera, 2007). Periods of stagnant polarity can last between some ten thousand years up to millions of years, with an average time of ~ 300.000 years (Garland, 1979). It was further observed that the magnetic poles show varying displacements from the geographic pole locations, which are called polar excursions.

Age determination of the magnetized rocks further gave essential paleomagnetic evidence for the appearance of continental drift, because by dating paleopole locations which presented a significant offset to the geographical poles it was possible to determine their paths on the Earth's surface in time. The investigations showed that the paths of observations from different continents did only coincide if the plates itself have moved (Garland, 1979). Before, scientists debated the appearance of True Polar Wander (TPW), which is defined as the rotation of either the planetary body or the whole lithosphere relative to the spin axis, triggered by mass redistributions.

Today it is known that polar reversals (PR) and polar excursions are recurrent events in the Earth's history and evolution of its main magnetic field. Assuming a former global Martian magnetic field with dipole characteristics (Sec. 1.2.1), Mars possibly underwent polar reversal events as well. Furthermore, under the assumption that Mars has no plate tectonics (Spohn et al., 2014) it is possible that Mars underwent a TPW event in its past.

Ever since MGS gave a detailed view on the Martian magnetic field several investigations to reveal its origin or to determine paleopole locations were made. A list of investigations by date is given in Tab. 1. Apart from Langlais and Purucker (2006), these

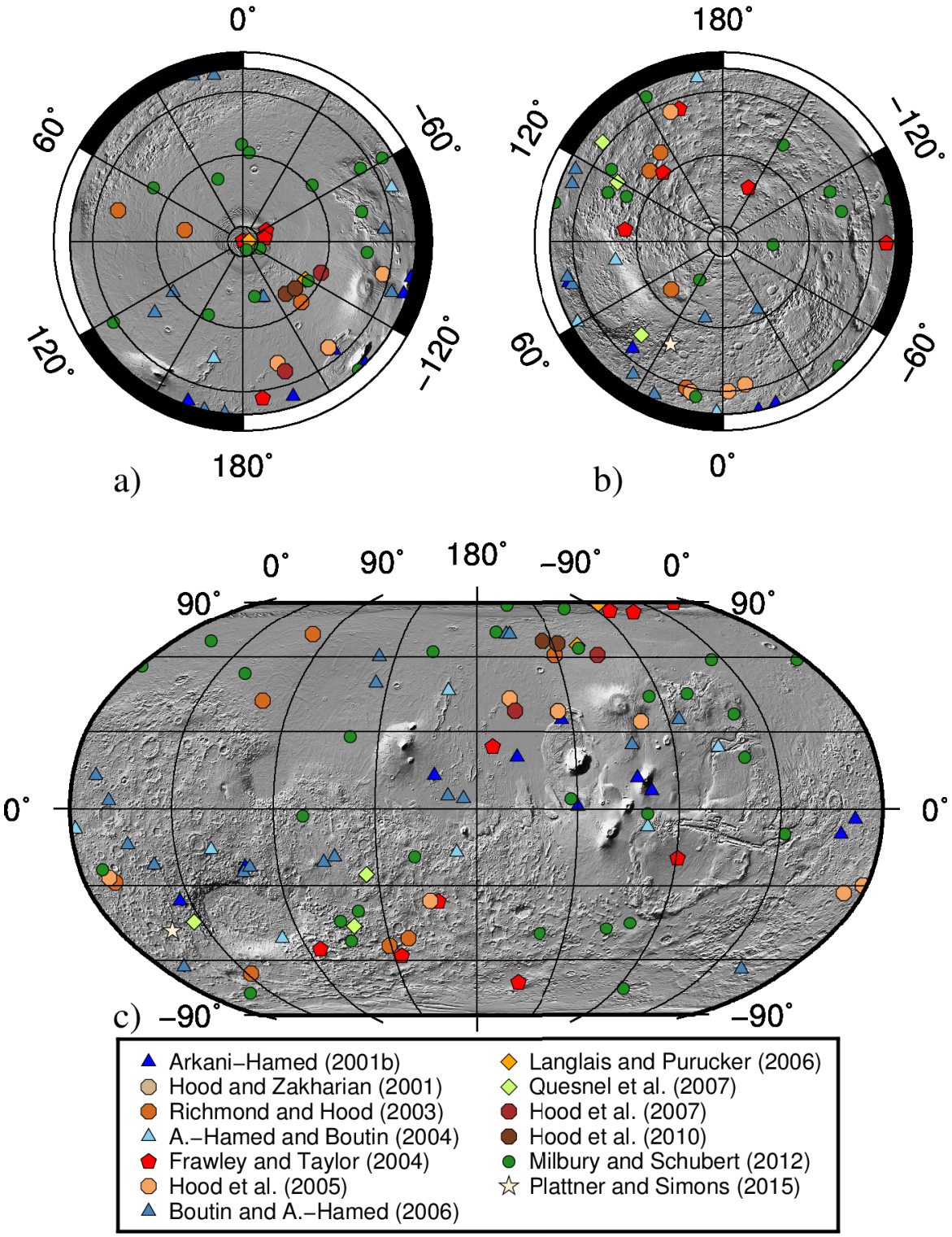

Figure 4: All published paleopole locations since 2001 were combined in this figure (Thomas et al., 2018) showing the derived paleopole locations from Arkani-Hamed (2001b), Hood and Zakharian (2001), Arkani-Hamed and Boutin (2004), Frawley and Taylor (2004), Hood et al. (2005), Boutin and Arkani-Hamed (2006), Langlais and Purucker (2006), Hood et al. (2007) and Quesnel et al. (2007), and Milbury and Schubert (2012) who suggested true polar wander has appeared on Mars, and the determined paleopole locations from Arkani-Hamed (2001b), Arkani-Hamed and Boutin (2004), Frawley and Taylor (2004), Boutin and Arkani-Hamed (2006), and Milbury and Schubert (2012) suggesting that the Martian dynamo underwent full polar reversals.

investigations followed the same approach by simulating the source of the observed magnetic fields with simple geometric shapes, such as vertical prisms, spheres, or disks. And again all but one (Plattner and Simons, 2015) concluded that PRs, TPW, or both occurred on Mars. The resulting paleopole locations from all investigations listed in Tab. 1 are shown in Figure 4. While individual investigations report distinct paleopole locations at low latitudes and in the vicinity of the Tharsis region, others show paleopole locations at high latitudes. The compilation of results since 2001 displays a wide spread of paleopole locations all over the Martian surface, questioning the robustness of the results. Additionally Arkani-Hamed and Boutin (2004) observed that differences in derived paleopole locations can reach 15° for small changes in the chosen source geometry and it was concluded by Biswas and Ravat (2005) that the overall present ambiguity in potential theory (Tarling, 2007; Telford et al., 1990) in combination with a coalescence effect of magnetic anomalies at satellite altitude and the assumption of uniform magnetic orientation results in even greater scatter ($> 50°$).

The shown paleopoles in Fig. 4 suggest between 20° and 60° TPW for Mars. Kite et al. (2009) and Bouley et al. (2016) assume that the formation of the Tharsis bulge has changed the moment of inertia and caused the TPW, but geologic investigations suggest TPW of less then 60° (Kite et al., 2009) and maybe only a TPW of $10° - 25°$ in the last 10^8 years (Bouley et al., 2016; Murray and Malin, 1973). With the mentioned uncertainties in mind it was of great interest to determine a quantitative measure for the possible, or expected spread in calculated paleopole locations (Sec. 3.3) and clearify if Mars underwent PR and TPW.

Table 1: Previous investigations of paleopole locations on Mars, listed with the data used, technique used for the inversion and the results and conclusions

Reference	Data / Inversion technique	Results and Conclusions
Arkani-Hamed (2001b)	SH-model with $l = m = 50$ at 120 km altitude / Magnetized vertical prisms of elliptical cross section	North and South magnetic poles within a 30° wide region, centered at 25° N / 230° E, suggesting 65° of TPW & PR
Hood and Zakharian (2001)	Along track data below 200 km altitude / Circular prisms near surface	30° of TPW with poles centered at 50° N / 225° E and 45° error
Arkani-Hamed and Boutin (2004)	SH-model with $l = m = 50$ / Vertical prisms of elliptical cross section with uniform magnetization and the top of the prism at the surface	$50° - 60°$ TPW & PR
Frawley and Taylor (2004)	Track data from 28 d cycle and the vector magnetic field components processed with Fourier series and screening for external field effects / Single dipole or prism	TPW & PR
Hood et al. (2005)	2780 orbits from MPO with wavelength filter for external field contributions / Circular prisms like Hood and Zakharian (2001) and uniform magnetized thin circular plates on surface	Pole clustering at $34° \pm 10°$ N / $202° \pm 58°$ E, with suggested $50° - 60°$ TPW
Boutin and Arkani-Hamed (2006)	Night time high altitude data with $\sim 28.8 \cdot 10^6$ data points / Same as Arkani-Hamed and Boutin (2004)	In agreement with Arkani-Hamed (2001b)

Reference	Data / Inversion technique	Results and Conclusions
Langlais and Purucker (2006)	Along track data below 250 km altitude / Equivalent source dipoles with uniform and non-uniform magnetizations and a regular least square fit	Preferred paleopole at 65° S / 59° E with ~ 25° of TPW
Quesnel et al. (2007)	MPO and AB data set in generalized, non-linear inversion / Uniformly magnetized spheres with the center beneath the maximum field strength of the anomaly	between $40° - 60°$ TPW
Hood et al. (2007)	68 orbits with 2D filtering for equally spaced arrays / Circular disks at shallow depths (< 50 km)	~ 30° of TPW with pole clustering in Terra Cimmeria / Sirenum
Hood et al. (2010)	Low orbit tracks / Same as Hood et al. (2007)	Poles at 65° N / 228° E and 67° N / 219° E with uncertainties of 13° and 16° and suggested TPW of ~ 25°
Milbury and Schubert (2012)	Track by track correlation with Langlais et al. (2004) / Equivalent source dipole technique from Langlais and Purucker (2006) with dipole depths between 0 km and 25 km and non-uniform magnetization	TPW during Noachian-Hesperian & PR
Plattner and Simons (2015)	Localized SH-model with $l = m = 130$ / Single dipole as magnetic source	Pole clustering around 48° N / 207° E with paleopole spread in between ~ 10° N to ~ 70° N and ~ 30° E to ~ 300° E

2

INVESTIGATING MAGNETIC FIELD DATA

Chapter two gives an overview on how magnetic fields are measured during space observations. It further presents the data sets of the Mars Global Surveyor (MGS) and Mars Atmosphere and Volatile EvolutioN (MAVEN) missions and the SH-model by Morschhauser et al. (2014), which allows to calculate the components of the vector magnetic field at any given coordinate.

2.1 MAGNETIC FIELD INSTRUMENTS

Several instruments for ground based magnetic field investigations are used for small, or large scale observations. In spacecrafts, the commonly used instrument is the fluxgate, or saturation induction magnetometer (Musmann and Afanassiev, 2009). To achieve the least magnetic disturbance from the spacecraft, the magnetometers are usually mounted on booms, or at the tips of solar panels and the remaining electromagnetic field of the spacecraft is subtracted to determine the measured field data.

In the following the basic principles and equations to describe how fluxgate magnetometers work are introduced. Further information is given by Musmann and Afanassiev (2009).

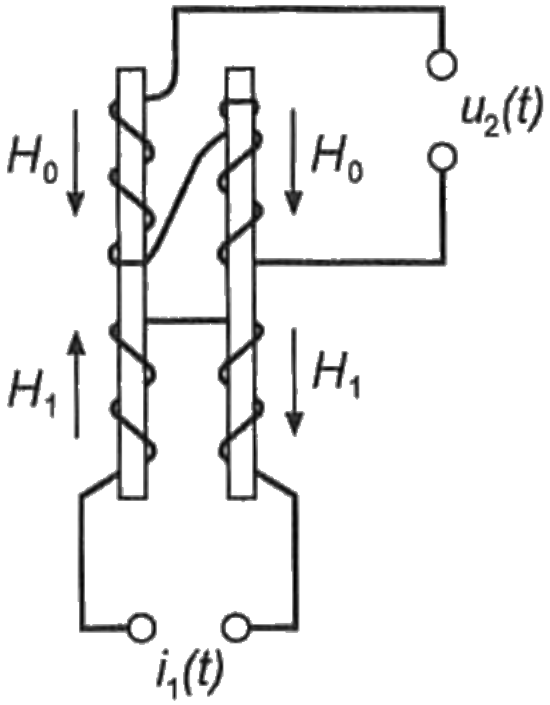

Figure 5: Schematic of a rod core fluxgate magnetometer with parallel scalar fields H_0 and H_1 wereby H_1 is derived from the inducing current $i_1(t)$ and $u_2(t)$ is the output voltage (Musmann and Afanassiev, 2009).

A fluxgate magnetometer in the easiest configuration consists of two coil systems. The first system is the so called drive coil, the other is called sense coil. At first an alternating

magnetic field H_1 is generated, saturating the cores of the drive coil. Then an electric current is induced from the drive coil's field in combination with the background magnetic field (H_0) within the sense coil. This is called electromotive force (EMF). The EMF is derived from the electromagnetic induction law:

$$U(t) = -n_c \frac{d\phi}{dt} = -n_c \frac{\vec{s} \cdot d\vec{B}}{dt} \tag{2.1.1}$$

Where $U(t)$ is the induced voltage in dependence of the time t. Further, n_c is the number of turns in the sense coil, ϕ is the magnetic flux, and $\vec{s}$ is the cross-sectional area of the fluxgate coils. $\vec{B}$ is the induction vector inside homogeneously magnetized (saturated) cores and depends on the sum $\vec{H}_\Sigma$ of the fields $\vec{H}_0$ and $\vec{H}_1$ and the vector function ρ which defines the nonlinear, anisotropic qualities of the cores.

$$\vec{B} = \rho\left(\left[\vec{H}_\Sigma\right]\right) \tag{2.1.2}$$

The square brackets indicate that the function is multivalued due to the hysteresis of magnetization. If hysteresis (Sec. 1.2.3) processes and anisotropy are neglected, Eq. 2.1.2 can be redefined (Eq. 2.1.4), only considering the nonlinear character of the cores and using the norm:

$$H_\Sigma = \sqrt{H_0^2 + 2H_0H_1\cos(\alpha) + H_1^2} \tag{2.1.3}$$

Where α is the angle between $\vec{H}_0$ and $\vec{H}_1$. With the reduction of the vector function ϕ to a scalar f this leads to:

$$B = f\left(H_\Sigma\right) \tag{2.1.4}$$

The combined measurement of $\vec{H}_1$ and $\vec{H}_0$ makes it possible to measure a constant background magnetic field $H_0 = const$. In the following this will be explained using a rod core fluxgate with parallel fields (Fig. 5). Rod core fluxgates were among others used for the Mariner 2, Sputnik 3 and the German AZUR spacecrafts. If the fields $\vec{H}_0$ and $\vec{H}_1$ are parallel ($\alpha = 0°$) the norm (Eq. 2.1.3) becomes $H_\Sigma = H_0 \pm H_1$ and the magnetic inductions in each of the cores are:

$$\begin{aligned} B' &= f(H_0 + H_1) \\ B'' &= f(H_0 - H_1) \end{aligned} \tag{2.1.5}$$

B' describes the magnetic induction in the first core and B'' defines the induction in the second core, leading to the induced voltage

$$U(t) = -n_c s \frac{d}{dt}(B' + B'') \tag{2.1.6}$$

with s being the cross-sectional area of one of the cores. If $B(H)$ would be linear it would follow $U(t) = 0$, but for the nonlinear dependence with two positive approximation coefficients a and b Eq. 2.1.4 can be written as:

$$B = a(H) - b(H)^3 \tag{2.1.7}$$

This then leads to the magnetic induction of both cores.

$$\begin{aligned} B' &= aH_0 + aH_1 - bH_0^3 - 3bH_0^2H_1 - 3bH_0H_1^2 - bH_1^3 \\ B'' &= aH_0 - aH_1 - bH_0^3 + 3bH_0^2H_1 - 3bH_0H_1^2 + bH_1^3 \end{aligned} \tag{2.1.8}$$

and

$$B' + B'' = 2aH_0 - 2bH_0^3 - 6bH_0H_1^2 \tag{2.1.9}$$

The last term of the equation creates the EMF and is defined by the product of the external and drive field. In combination with Eq. 2.1.6 it follows for $H_0 = const$:

$$U(t) = 6bsn_cH_0\frac{d}{dt}H_1^2 \neq 0 \tag{2.1.10}$$

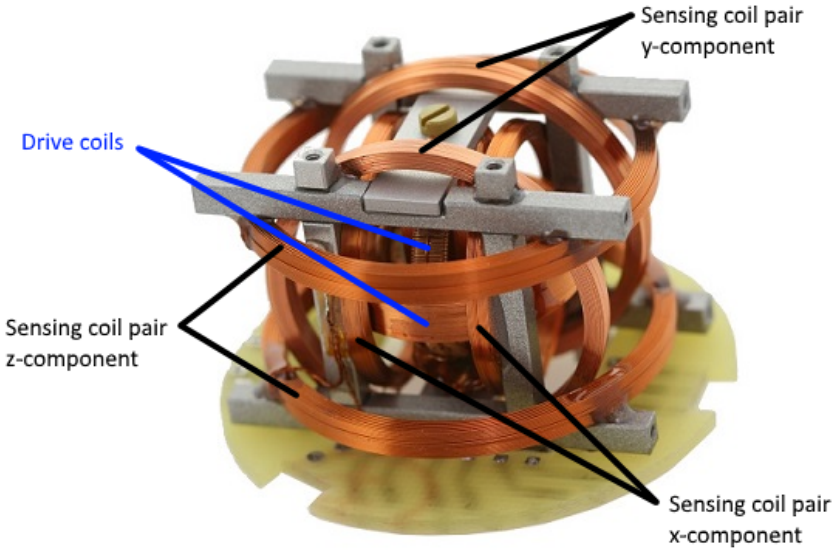

Figure 6: Ring core magnetometer with three sensing coil pairs to measure the x, y, and z-component of the vector magnetic field and two driving coils in the xz and yz plane. ©Magson GmbH

The main information in Eq. 2.1.10 is that even without a change in the external field H_0 a measurement is taken, because the field H_1 is time dependent and H_0 multiplies the EMF. Therefore, Fluxgate magnetometers can be used as immobile reference stations on the ground as well as on moved platforms.

However, the described rod core magnetometers require high drive power and the common fluxgates are now ring core magnetometers (Fig. 6). These magnetometers have a reduced power consumption, a higher precision, and are more convenient on spacecrafts. They were first used in space for the Lunar Surface Magnetometer package during the Apollo 16 mission in 1972. The MGS spacecraft carried two instruments called MAG, which consisted of two tri-axial ring core fluxgate magnetometers (Acuña et al., 1992) mounted to the tips of its solar panels to avoid disturbances from the spacecraft. In addition, the solar panels were designed to be magnetically clean (Acuña et al., 2001).

A three-axis magnetometer can be realized with two ring shaped driving coils in the xz and yz plane as well as three sensing coils in the xy, xz, and yz plane, respectively (Fig. 6). The magnetometers for MGS and MAVEN followed the design by Mario Acuña from Goddard Space Flight Centre, using only two sensing coils measuring two orthogonal directions of the vector magnetic field simultaneously (Connerney et al., 2015a). This way the MAVEN-MAG instrument can in principle achieve a resolution of 0.008 nT.

2.2 THE MARTIAN MAGNETIC FIELD

2.2.1 *Data*

*Mars Global Surveyor (**MGS**)*

The Mars Global Surveyor spacecraft started to operate in Martian orbit in 1997 and provided the most complete magnetic survey until it stopped its operation in 2006. Using two tri-axial magnetometers MGS was able to measure ambient fields from ± 4 nT to ± 1550 nT (Morschhauser et al., 2014) at altitudes between 80 km and 400 km and sampling rates of 32 Hz. The full MGS-MAG data set is available on the Planetary Data System (PDS) and contains $\sim 176.2 \cdot 10^6$ data points from the Mapping Phase Orbit (MPO) period and $\sim 3.04 \cdot 10^6$ data points from the AeroBraking (AB) and Science Phase Orbit (SPO) periods. It was possible to work with processed data in terms of data weighting and exclusion of outliers, provided from the model development of Morschhauser et al. (2014). Therefore, the number of data points and the computational time to process this data is reduced. In detail MPO, AB, and SPO data was handled as follows by Morschhauser et al. (2014).

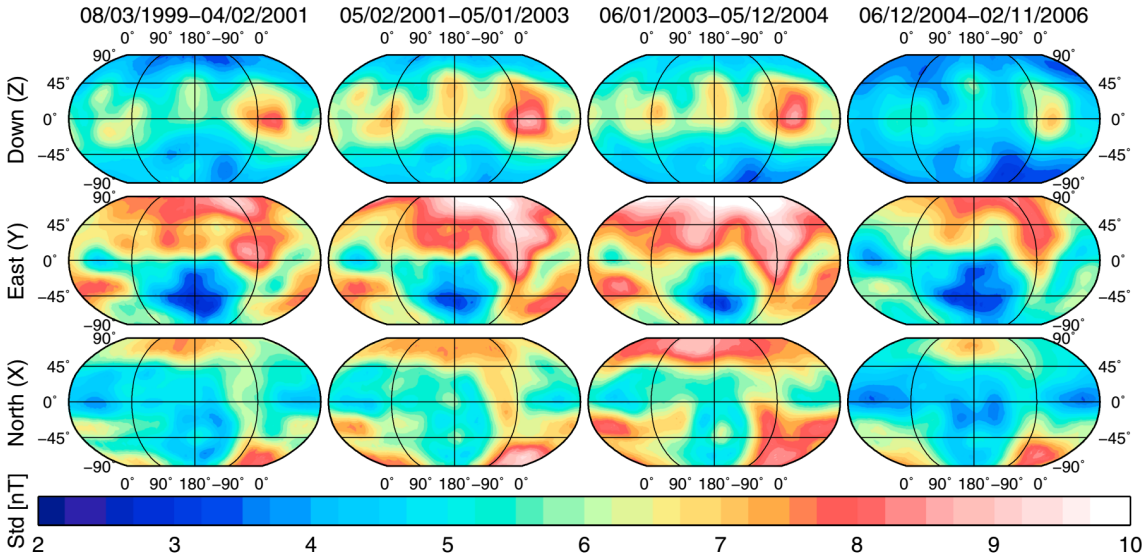

Figure 7: Figure 2 of Morschhauser et al. (2014), showing the estimated, and smoothed standard deviations (STDs) which were used to weight the MPO data. Each column shows one of the four Martian annual epochs and the STDs for every component of the vector magnetic field in the rows. The data weights were obtained by estimating the STDs in bins of constant altitude which were then fitted to spherical harmonic functions of degree and order 8. It can be seen, that the Down-component shows lower STDs than the North- or East-component

The MPO data set provides a dense global coverage at a locally nearly constant altitude, which varies from 422.1 km at the geographic North Pole down to 348.6 km at the South Pole. When projected on a constant planetary radius of $R_M = 3393.5$ km the average data density totals to $\sim 0.390\ \text{km}^{-2}$ (Morschhauser et al., 2014). It was concluded by Brain et al. (2003) that the dayside magnetic field is dominated by non-crustal contributions, e.g. from ionospheric currents, down to an altitude of ~ 200 km. To reduce the influence of the induced ionospheric currents MPO's dayside data was excluded. Thus the number of MPO data points was reduced to $\sim 56.3 \cdot 10^6$, leading to data gaps of 4.42° at the North Pole and 2.86° at the South Pole, due to the different orbit altitudes (Morschhauser et al.,

2014). Data was further reduced to $\sim 2.58 \cdot 10^6$ data points only choosing one point every 80 km of the satellites track projected onto the surface.

In a next step the data was split into four epochs, respectively four annual data sets. Then the data weights were estimated by using the stable MPO orbit and binning the data in sections of constant altitude and subsequently calculating the variances in each bin, resulting in 77 to 91 data points per bin. The resulting standard deviations (STDs) show a global trend and vary between neighboring bins, due to insufficient numbers of data points in each bin (Morschhauser et al., 2014). The remaining values were then weighted with the number of data points in each bin and fit to a SH function of degree and order 8. This led to smoothed STDs for all three components of the vector magnetic field, which were then used to weight the MPO data (Fig. 7).

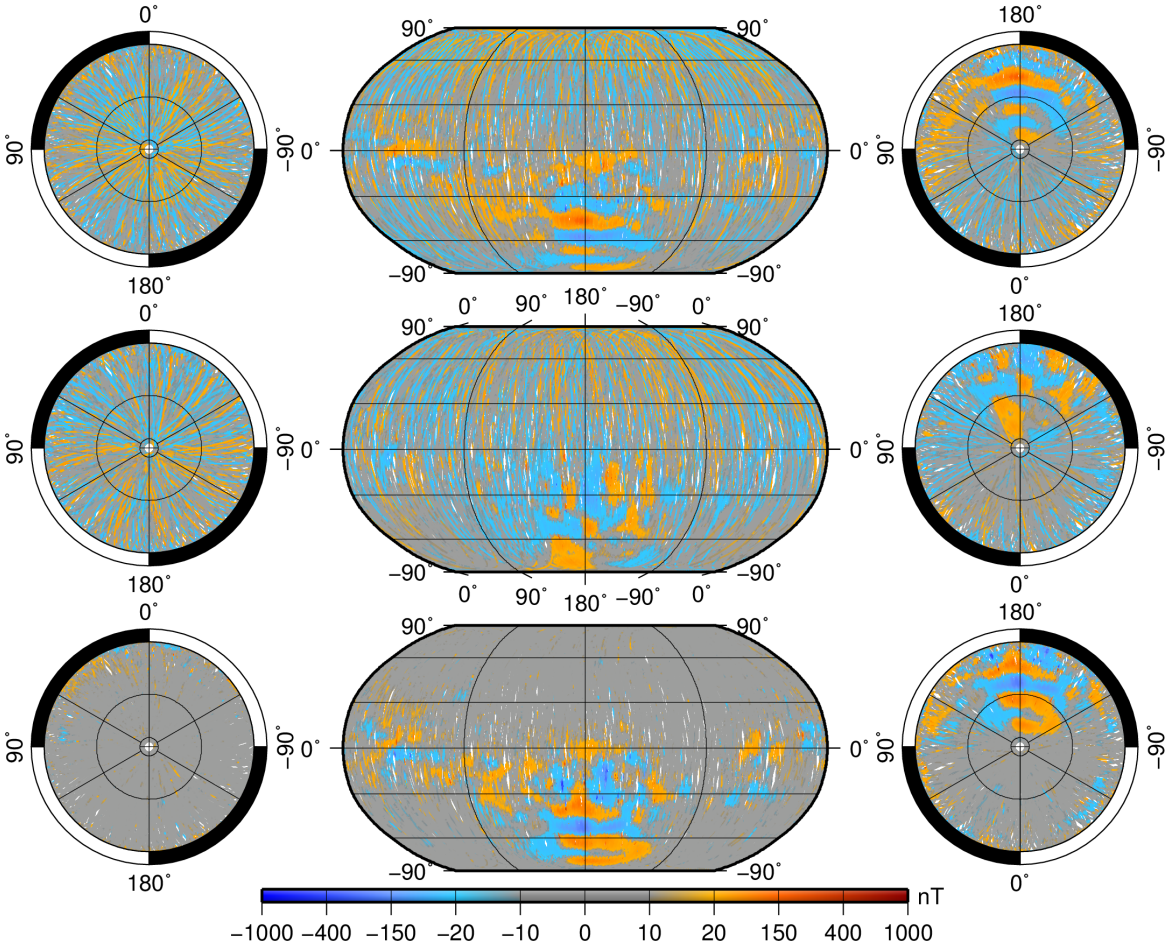

Figure 8: Magnetic field data coverage and field strength during the AeroBreaking and Science Phase Orbits below the altitude of 180 km. The top part of the figure shows the B_x-, or North-component, the middle part shows the B_y-, or East-component, and the bottom part is the B_z-, or Down-component. All parts have a spherical projection of the North Pole to the left, a spherical projection of the South Pole to the right and a Robinson projection in the middle.

As shown in Fig. 7, the Down-component in the top row of the figure provides lower STDs than the East- and North-component of the magnetic field. This agrees with previous observations by e.g. Acuña et al. (1999) and Arkani-Hamed (2004) who concluded that the Down-component is less effected by external magnetic fields. It can be further seen, that STDs increase from the first to the third epoch in all three components. These higher STDs are a direct cause of an increased geomagnetic storm activity in the Martian

ionosphere, due to the beginning of the declining phase of the solar cycle (Echer et al., 2008, 2013). The changing solar activity is another reason to primary work with nightside data, or data measured below the altitude of 200 km. Therefore, the AB and SPO data sets were further processed and then integrated into the SH-model by Morschhauser et al. (2014).

As mentioned earlier, the AB and SPO data set additionally provided $\sim 3.04 \cdot 10^6$ vector measurements to the MPO data set, but less than $0.5 \cdot 10^6$ measurements were taken below the minimum altitude (348 km) reached during the MPO. Furthermore, $\sim$ 99.39% of this data was obtained at the dayside of Mars (Morschhauser et al., 2014). The magnetic field signal from the crustal magnetization is altered by the solar wind (Cain et al., 2003) at the dayside down to an altitude of 200 km (Brain et al., 2003). Therefore, Morschhauser et al. (2014) excluded all dayside data above the altitude of 200 km from the data set which led to less than $0.3 \cdot 10^6$ data points with a data density of ~ 0.0051 km^{-2} (Fig. 8), or a planetary data coverage of $\sim$ 39%, respectively. In the next step of data processing, Morschhauser et al. (2014) calculated the STDs from the residuals of the AB/SPO data to a preliminary model weighted by the MPO data. Then the STDs were fitted to a Gaussian distribution to determine the data weights.

*Mars Atmosphere and Volatile EvolutioN (**MAVEN**)*

The MAVEN spacecraft launched in November 2013 and arrived at Mars in September 2014. In November of the same year the mission started its one Earth-year Primary Science Phase (Jakosky et al., 2015). It had a nominal periapsis altitude of $\sim$ 150 km ("deep dip") and an apoapsis altitude of 6220 km, with a period of 4.5 h and an orbital inclination of 75°. The mission then went on with Continued Science Operations, lasting for two years and is now in the Long Duration Extended Mission Science and Relay Phase (Jakosky et al., 2015). Among other scientific instruments the MAVEN spacecraft carried two tri-axial fluxgate sensors mounted on small booms at the end of the solar arrays (Connerney et al., 2015a). The fluxgate magnetometers had the same design as the MGS-MAG (Sec. 2.1) with a measurable amplitude of up to 65536 nT and an achievable resolution of 0.008 nT. Due to the high ellipticity of MAVEN's orbit, low altitude data became available and MAVEN data now shows a more uniform spatial coverage than the previous MGS mission data below the altitude of $\sim$ 400 km (Mittelholz and Johnson, 2017). The new data agrees well with the model by Morschhauser et al. (2014) with descrepancies mostly in amplitude of the crustal magnetic field. It seems likely that unmodeled signals increase residuals between the SH-model and measured data at low altitudes (Mittelholz and Johnson, 2017). The MAVEN data set could therefore resolve more details of observed anomalies or even reveal other small-scale anomalies which have not been previously detected. In order to use the MAVEN magnetic field data for the following investigations, the data set was downloaded from the PDS server, downsampled to 1 Hz, and the components of the vector magnetic field were transformed into the North-East-Down coordinate system. The data was then reduced by only choosing data below an altitude of 180 km (Fig. 9), to avoid ionospheric alterations of the crustal magnetic field signal (Brain et al., 2003) and get a better resolution towards small-scale and low wavelength anomalies. After the processing $\sim 1.784 \cdot 10^6$ data points remained for the following investigation.

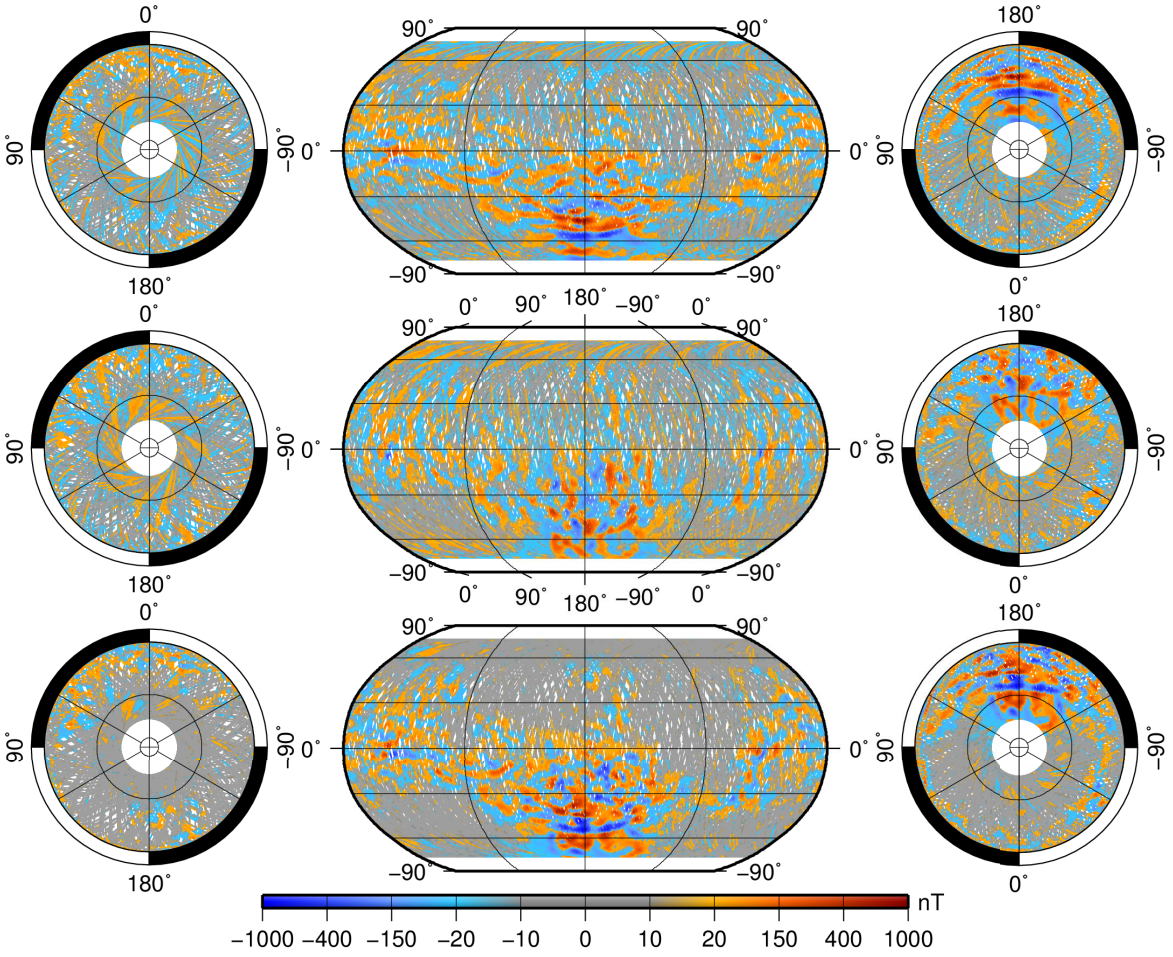

Figure 9: Same as Fig. 8 but for the MAVEN magnetic field data. It can be seen, that no data is available above ±80° latitude.

2.2.2 *Models*

Soon after the MGS measurements achieved a global coverage of the Martian magnetic field, several magnetic field models were developed (Arkani-Hamed, 2001a, 2002, 2004; Morschhauser et al., 2014; Plattner and Simons, 2015). All those cited use SH-functions to describe the observed magnetic field. The earliest global model by Arkani-Hamed (2001a) was cut off at order and degree 50, while the latest, model by Plattner and Simons (2015) reached degree and order 130. In this thesis the SH representation of the field derived by Morschhauser et al. (2014) is used. The field has been expanded to SH degree and order 110 and been regularized by minimizing the horizontal gradient of the vertically down component of the field at surface altitude. The model is characterized by a low noise level and it is robust when downward continued to the surface (Morschhauser et al., 2014).

An observed magnetic field can be modeled by using SH-functions, because they solve the Laplace-equation using spherical coordinates (Blakely, 1996). The modeling is done in terms of magnetostatics, using the reduced Maxwell equations, and the assumption that no time dependent currents alter the magnetic field (**B**). The remaining Maxwell equations are:

$$1.\quad \nabla \cdot \mathbf{B} = 0 \qquad\qquad 2.\quad \nabla \times \mathbf{B} = \mu \vec{j} \tag{2.2.1}$$

The first Eq. in 2.2.1 is derived from the Coulomb gauge and describes that a magnetic flux going through a closed surface is zero, or shortly "magnetic monopoles do not exist". In the second Eq. in 2.2.1 it is defined, that electric currents $\vec{j}$ generate magnetic field lines in closed loops (Ampères law). The strength of the magnetic field depends on the magnetic permeability μ. For air or vacuum conditions μ is reduced to $\mu_0 = 4\pi \cdot 10^{-7} \frac{Vs}{Am}$. If it is assumed that no macroscopic currents ($\vec{j} = 0$) are present, Ampères law is reduced to $\nabla \times \mathbf{B} = 0$. After the Helmholtz-theorem the magnetic field can now be expressed as the gradient of a scalar potential Ψ (Blakely, 1996; Meschede, 2005), with

$$\mathbf{B} = -\nabla\Psi \,. \tag{2.2.2}$$

If the Martian surface is approximated by a spherical surface with the coordinates r, θ, and ϕ, then the magnetic field at a given location $\mathbf{r}_j = (r, \theta, \phi)^T$ is calculated as follows

$$\mathbf{B}_{SH}(\mathbf{r}_j) = -\nabla \left(a \sum_{l=1}^{L} \left(\frac{a}{r}\right)^{(l+1)} \sum_{m=-l}^{l} g_l^m Y_l^m(\theta, \phi) \right) \,. \tag{2.2.3}$$

Where r is the observation radius, $a = 3393.5$ km is the reference radius of the model, and $Y_l^m(\theta, \phi)$ denote the Schmidt semi-normalized SH-functions:

$$Y_l^m(\theta, \phi) = \begin{cases} \sin(|m|\phi) P_l^{|m|}(\cos\theta), & \text{if } m < 0 \\ \cos(m\phi) P_l^m(\cos\theta), & \text{if } m \geqslant 0 \end{cases} \tag{2.2.4}$$

The SH-functions depend on latitude (θ) and longitude (ϕ) and the Legendre Polynomials P_l^m, calculated from

$$P_l^m(x) = \frac{(-1)^m}{2^l l!} (1 - x^2)^{\frac{m}{2}} \frac{d^{l+m}}{dx^{l+m}} (x^2 - 1)^l \,. \tag{2.2.5}$$

Degree and order of the respective SH-function are denoted with l and m, with L as the maximum degree of the expansion ($L = 110$ for the SH-model by Morschhauser et al., 2014). The parameter g_l^m are the internal Gauss coefficients. Using Eq. 2.2.3, the field can be evaluated at any location by a simple coordinate transformation and the single components of the magnetic vector field can be calculated from:

$$B_x = \frac{1}{r} \frac{\partial \Psi}{\partial \theta} = \sum_{l=1}^{L} \sum_{m=-l}^{l} \left[\left(\frac{a}{r}\right)^{l+2} g_l^m \right] \frac{\partial Y_l^m}{\partial \theta}$$

$$B_y = -\frac{1}{r \sin\theta} \frac{\partial \Psi}{\partial \phi} = -\frac{1}{\sin\theta} \sum_{l=1}^{L} \sum_{m=-l}^{l} \left[\left(\frac{a}{r}\right)^{l+2} g_l^m \right] \frac{\partial Y_l^m}{\partial \phi}$$

$$B_z = \frac{\partial \Psi}{\partial r} = -\sum_{l=1}^{L} \sum_{m=-l}^{l} \left[(l+1) \left(\frac{a}{r}\right)^{l+2} g_l^m \right] Y_l^m \tag{2.2.6}$$

Fig. 10 shows the three components of the vector magnetic field derived from the SH-model of Morschhauser et al. (2014), evaluated at surface altitude. It can be seen that

the gaps in the AB/SPO data (Fig. 8) disappeared and the crustal field was downward continued from orbit altitude (80 km - 200 km) to the surface. It is now possible to study the high magnetized regions in Terra Cimmeria and Terra Sirenum in more detail. Additionally, distinct magnetic features in regions of low magnetic field intensity, e.g south of Hellas Planetia or in the Northern Lowlands can now be further investigated.

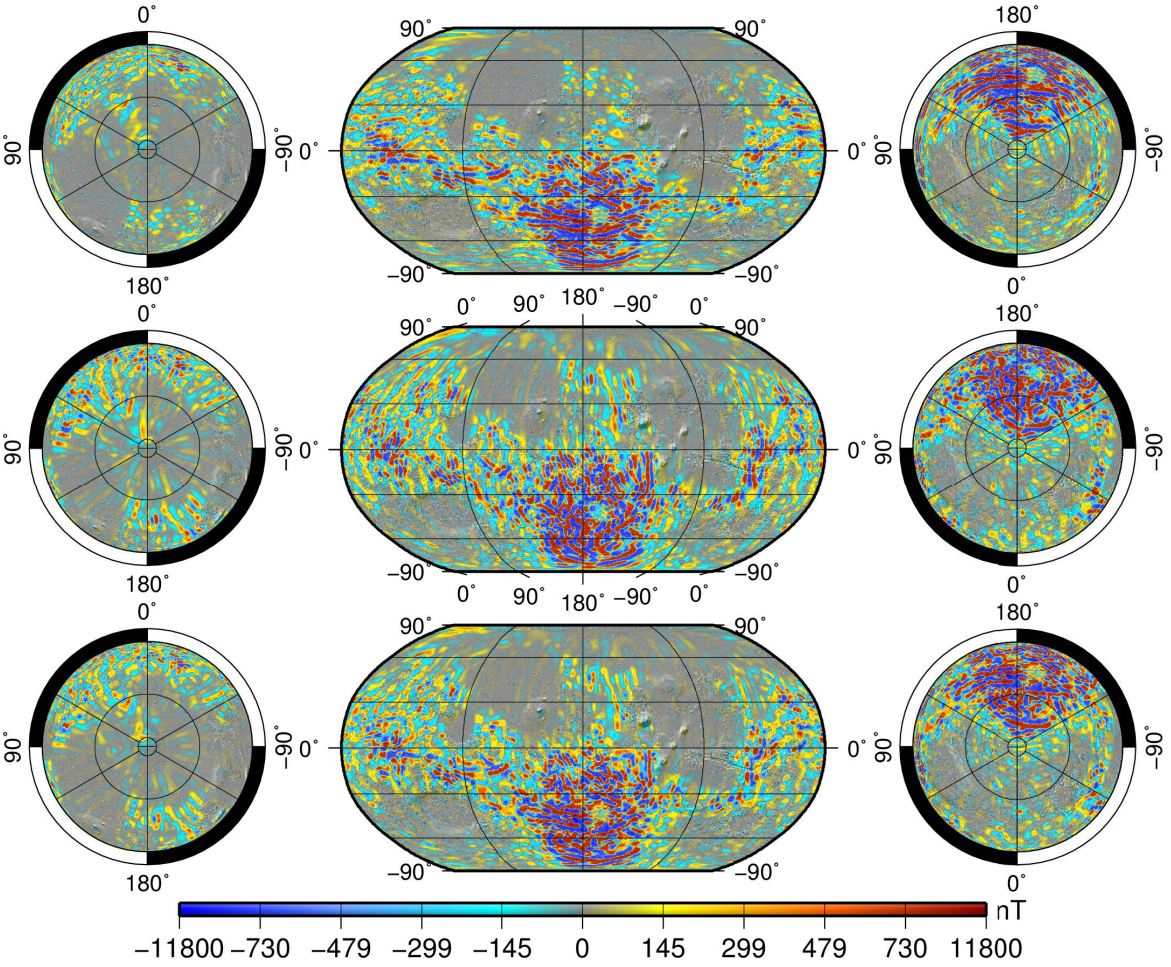

Figure 10: Maps of the vector magnetic field as derived from the SH-model by Morschhauser et al. (2014) superposed on a MOLA shaded relief map. The B_x- (top), B_y- (middle), and the B_z-component (bottom) at surface altitude are shown. On the left and right hand side of the figure spherical projections of the Martian North and South Pole are shown in combination with a global map in Robinson projection in the middle.

2.2.3 *Characteristics of the field*

The Martian magnetic field is very different from the Earth's crustal magnetic field in intensity and distribution (Acuña et al., 1999; Connerney et al., 2001). While Earth holds a nearly global coverage of crustal magnetization, the magnetization on Mars is mostly reduced to one hemisphere with strong magnetic fields covering around two-thirds of the Southern Highlands (Fig. 10 / App. B). The origin of the so called Martian magnetic dichotomy is still debated (App. B / white line). Its generation might be linked to the formation of the Northern Lowlands, with the suggestion that the formation erased the majority of the existing topography and magnetization. In this context it was suggested by Gubbins and Herrero-Bervera (2007) that the preserved magnetic anomalies in the

northern hemisphere could be the remains of stronger anomalies that existed before the Lowlands formed.

As mentioned in Sec. 1.2.1 another suggestion to explain the magnetic dichotomy was given by Stanley et al. (2008), who proposed that the Martian magnetic field was formed by a single hemisphere dynamo. Proceeding from the assumption that the magnetized layer within the Martian crust is at average around 30 km thick (Langlais et al., 2004; Lewis and Simons, 2012; Nimmo and Gilmore, 2001), and maybe up to 100 km thick (Nimmo and Gilmore, 2001; Ruiz, 2009; Ruiz et al., 2006) it was in contrary suggested by Dietrich and Wicht (2013) that the magnetic field preserved in the crust could not reach the observed amplitudes, because a single hemisphere dynamo would have a PR period of ~ 0.01 Ma, and the magnetized layers would average to zero.

Another theory about the topographic and magnetic dichotomy's origin is a giant impact, the so called Borealis (Andrews-Hanna et al., 2008; Marinova et al., 2008; Wilhems and Squyres, 1984). This could have demagnetized the Northern Lowlands due to the impact (Nimmo et al., 2008), as well as parts of the Southern Highlands through shock and thermal effects (compare Fig. 10). After Citron and Zhong (2012), this impact had the potential to demagnetize the crustal magnetic field on a global scale, because thermal blanketing of the ejecta deposition can appear.

On a smaller scale the large impact basins Hellas (41° S / 70° E), Argyre (50° S / 316° E), and Isidis (13° N / 88° E) are good examples for such a scenario. The basins formed by large impact events around 4 Ga ago. The energetic impacts resulted in shock pressures and high temperatures which demagnetized the crust underneath the basins (Hood et al., 2003; Kletetschka et al., 2004; Mohit and Arkani-Hamed, 2004). As a result that the crust beneath the basins is completely demagnetized to a distance of ~ 0.8 times the basins radius and partially demagnetized up to ~ 1.4 times the radius of the basin (Gubbins and Herrero-Bervera, 2007). In comparison, smaller craters between 200 km and 500 km diameter show no or only negligible demagnetization, which led Mohit and Arkani-Hamed (2004) to the conclusion that the magnetic carriers of the Martian crust have high coercivity. The resulting demagnetization effect strongly depends on coercivity of the magnetic minerals, e.g. a shock of 1 GPa can remove $\sim 50\%$ of the magnetization of a single domain pyrrhotite with a coercivity of around 300 mT and it is fully demagnetized under a pressure of 2.75 GPa (Rochette et al., 2003). Within the large basins pressures of 3 GPa could be reached in the center, which decreased to ~ 2 GPa towards the edges. The magnetic signal within a pyrrhotite would have been destroyed. The preservation of the magnetic signal in small impact craters is therefore partly due to difference in pressure and the over all high coercivity of magnetic carriers in the Martian crust.

Other explanations for the origin of the dichotomy suggested that TRM processes were constrained to only one hemisphere (Citron and Zhong, 2012), or that regional differences in CRM conditions led to the differently magnetized hemispheres (Hood et al., 2005; Quesnel et al., 2009). However, all of the proposed scenarios remain to be proven and from the available data it is impossible to derive if a subsurface magnetic source originated from TRM, CRM or if it has been partly demagnetized by thermal blanketing. Further constraints could be derived by dating the magnetized rocks, but the real age and magnetization of a rock can always be altered by post-formational metamorphic or thermal events (Garland, 1979; Gubbins and Herrero-Bervera, 2007).

Another distinct feature of the Martian magnetic field is the much weaker magnetization at the Tharsis bulge (App. B) in comparison to the magnetization south of it (Fig. 10). The Tharsis bulge itself formed through major volcanic activities in the Noachian (prior

3.7 Ga) and early Hesperian ($3.7 - 3.4$ Ga) (Spohn et al., 2014) and it most certainly has formed in the absence of a core dynamo (Arkani-Hamed, 2004). Additionally to Tharsis, its surroundings hold many topographic features, e.g. the shield volcanoes Olympus, Arsia, Pavonis, and Ascreaus Mons as well as the canyon Valles Marineris (App. B). All of these distinct topographic features generate no significant magnetic signal, because their formation followed the dynamo decease (Hood and Hartdegen, 1997). After Gubbins and Herrero-Bervera (2007) magnetic edge effects should be expected if their formation demagnetized the preexisting crust, but this requires a strongly magnetized Tharsis buldge prior the formation of the volcanoes and the canyon. Only in the east of Valles Marineris a magnetic signal is preserved (Fig. 10).

In addition, Martian volcanoes demagnetized the crust rather than preserved magnetization in it due to TRM. This is especially a drawback for dating magnetic alterations. One approach to estimate the reversal periodicity was to analyze the magnetic signals of short-lived volcanoes and combine the results with their estimated formation age. Apart from the volcanoes a derivation of the formation age is possible for the numerous craters on the Martian surface, but links between the crater formation and the underlying magnetic signal are not certain. Therefore, we must await detailed paleomagnetic studies on samples, which give clear estimates of the ages of an observed magnetized layer.

Part II

METHODS

There are many different techniques to determine the magnetization strength and magnetic orientation of an unknown source body, thus the obstacle is to use the technique with the right assumptions. Because it is unclear whether an assumption is accurate or not it seems plausible to make use of a technique which uses the least restrictive assumptions to avoid false interpretation. For this reason a special version of the Equivalent Source Dipole method was chosen in this investigation to model the magnetic orientation of Martian magnetic field sources. In the following the necessary assumptions and mathematical techniques to use this method are given and synthetic model magnetizations are used to evaluate the capacities and robustness of the implemented model.

3

INVERSION

In this chapter the major assumptions and techniques for magnetic source modeling using Equivalent Source Dipoles (ESDs) are given. This chapter further explains how a confidence limit threshold was determined to constrain areas of admissible paleopole locations. Therefore, two mathematical methods are presented and further an observational method (Sec. 3.3.3) is shown, which illuminates possible disturbances of the field and how these disturbances can be estimated to determine a measure of confidence.

3.1 INVERSION APPROACH

The Martian crustal magnetic field originates from a former main magnetic field which was either global and aligned with the rotational axis (Dietrich and Wicht, 2013; Langlais et al., 2004; Lillis et al., 2013), or only constrained to a single hemisphere (Stanley et al., 2008). To reconstruct paleopole locations from a given magnetic field it is necessary that the magnetic orientation can be related to the latitude and longitude on the planet (Sec. 1.3). This is only possible for a global dipolar magnetic field. In this thesis it is therefore assumed that the crustal magnetic field of Mars was generated under the influence of a global, dipolar magnetic field (Sec. 1.2.1). Due to the relatively strong crustal magnetization this is a reasonable assumption (Dietrich and Wicht, 2013; Lillis et al., 2013).

Comparable to the main field on Earth the former Martian magnetic field possibly underwent long-term variations such as polar reversals (PRs) and true polar wander (TPW), which can be preserved in the crust (Sec. 1.4). We furthermore need to assume petrogenetic processes which are short in comparison to the timescale of potential long term variations, such as PRs of the main field (Sec. 1.4). Only then a single cycle of stagnant magnetic orientation can be saved as remanent magnetization within a geologic formation. In the modeling it is therefore assumed that studied anomalies posses unidirectional magnetization, as would for example be attained by cooling of magma below the Curie temperature, thus acquiring TRM.

Most methods for modeling crustal magnetic field anomalies assume that the magnetized region is of simple geometric shape, as this enables a derivation of closed expressions for the predicted field (Sec. 1.4 / Tab. 1). The geometry parameters and the orientation of the magnetizing field can be varied to obtain the best fit between predicted and observed fields. However, the observed field could in principle be the result of an infinite number of differently shaped sources (Blakely, 1996; Telford et al., 1990) and it was shown that common methods for paleopole inversions introduce strong implicit assumptions concerning the null space as well as the full spectral content of the magnetization distribution (Vervelidou et al., 2017a). It is therefore reasonable to choose a method with the least constraints, because then the chances to violate the underlying assumptions are minimized (Vervelidou et al., 2017a).

In the published investigation (Thomas et al., 2018) the method of Parker (1991) was implemented, which has the advantage that no assumptions concerning depth, susceptibility or lateral extent of the sources are required (Mayhew, 1979; Parker, 1991). The magnetic sources are synthesized by a regular distribution of dipoles on the surface above the magnetic anomaly (ESDs). This is possible due to the fact, that uniformly magnetized

regions are enclosed by equipotential surfaces (Parker, 1975, 1991), which can not be disconnected from the boundary of the magnetized volume. In his paper from 1991 Parker explained this theory as follows:

A set of data d_j can be modeled by characterizing parameters M_p using a certain function g_j describing the model (Aster et al., 2013), of which some model is capable to solve with an exact fit (Parker, 1991). In terms of magnetics, d_j are the measured vector magnetic field components or the vector magnetic field as derived from the SH-model. The parameters M describe the unknown magnetic moments which are later on denoted with $\mathbf{m}_i$ and the model function g_j is defined by the locations of the distributed sources and observation points.

$$d_j = g_j(M_p) \quad \text{with } j = 1, 2, 3, ...K \tag{3.1.1}$$

If the model is not able to obtain an exact fit, a model can be found solving with the **2-norm**, or Euclidean length (Aster et al., 2013; Parker, 1991).

$$T = \|d_j - g_j M_p\|_2 = \sqrt{\sum_{j=1}^{K} (d_j - g_j M_p)^2} \tag{3.1.2}$$

It is now an objective to minimize T rather than using it as a constraint for the model and an upper bound M_0 on M_p is used as new constraint. It was shown by Parker (1975) that T is a minimized subject to $0 \leqslant M_p \leqslant M_0$ and the best solution is given by a magnetic ideal body of uniformly magnetized regions which are enclosed by equipotential surfaces. Those magnetized zones can not be disconnected from the boundary of the magnetized volume V_M (Parker, 1991). V_M is a factor to the force of the magnetic moment $\mathbf{m}$. In Parker's method the volume contribution is neglected and hence the missing factor must be compensated. This is done by assuming that the magnetization strength M_i has no upper boundary. As mentioned earlier, the magnetized zone can not be disconnected from V_M, the dipoles with $M_i \to \infty \frac{A}{m}$ must therefore accumulate on the surface. An included revision on Parker (1991) from Gary Egbert which I found helpful, stated the findings as follows:

If there is no exact solution but one with $T > 0$ generating anomaly data d'_j, then there exists a solution M'_p within the surface ∂V_M with similar magnetic anomaly values as in V_M. Therefore, a search constrained to ∂V_M is sufficient to find a model with some misfit $T > 0$, which includes the best fitting model with $T = 0$.

3.2 THE ESD METHOD FOR MAGNETIC FIELD MODELING

In order to model a given crustal magnetic anomaly, N dipoles are distributed at locations $\mathbf{s}_i$ in the study area. We chose an equal distanced distribution pattern in the shape of a hexagonal grid. The smallest distribution contains 7 dipoles with one dipole in the center and six dipoles building the edges of the hexagon at a distance R_0, which is in the following denoted as the dipole distribution radius. Around each dipole a new hexagon with radius $\frac{1}{2}R_0$ can be build to distribute a total number of 19 dipoles within R_0. By continuously bisecting the radius it is possible to distribute more and more dipoles within R_0. For example, at an interdipole distance of $\frac{1}{8}R_0$, 241 dipoles are distributed in the circular region defined by R_0. Similar to the dipole distribution, observation points are distributed within a region of radius R_s using a hexagonal grid. R_s is in the following denoted as the observation point distribution.

Generally, the magnetic field $\mathbf{B}_j$ at the location $\mathbf{r}_j$ generated by the dipoles with magnetic moment $\mathbf{m}_i = M_i\hat{\mathbf{m}}_i$ at the location $\mathbf{s}_i$ is given by (e.g. Blakely, 1996)

$$\mathbf{B}_j(\mathbf{r}_j) = \frac{\mu_0}{4\pi}\sum_{i=1}^{N}\frac{M_i}{|\mathbf{r}_j-\mathbf{s}_i|^5}\left(3(\mathbf{r}_j-\mathbf{s}_i)[\hat{\mathbf{m}}_i\cdot(\mathbf{r}_j-\mathbf{s}_i)]-\hat{\mathbf{m}}_i|\mathbf{r}_j-\mathbf{s}_i|^2\right), \tag{3.2.1}$$

where μ_0 is the magnetic permeability in vacuum and the sum extends over all dipole contributions to the observed field. By evaluating the field at $K \geqslant N$ locations $\mathbf{r}_j$, a linear system of equations is obtained and the magnetic field $\mathbf{B}_j$ can be calculated using equation 3.2.1, rewritten in matrix form:

$$\mathbf{B}_j(\mathbf{r}_j) = \mathbf{A}_{ji}(\mathbf{r}_j,\mathbf{s}_i)\mathbf{m}_i \tag{3.2.2}$$

where

$$\mathbf{A}_{ji}(\mathbf{r}_j,\mathbf{s}_i) = \frac{\mu_0}{4\pi\cdot\Delta r_{ji}^5}\begin{pmatrix} 3(r_j^x-s_i^x)^2-\Delta r_{ji}^2 & 3(r_j^x-s_i^x)(r_j^y-s_i^y) & 3(r_j^x-s_i^x)(r_j^z-s_i^z)\\ 3(r_j^x-s_i^x)(r_j^y-s_i^y) & 3(r_j^y-s_i^y)^2-\Delta r_{ji}^2 & 3(r_j^y-s_i^y)(r_j^z-s_i^z)\\ 3(r_j^x-s_i^x)(r_j^z-s_i^z) & 3(r_j^y-s_i^y)(r_j^z-s_i^z) & 3(r_j^z-s_i^z)^2-\Delta r_{ji}^2\end{pmatrix} \tag{3.2.3}$$

is a matrix defined by the three dimensional North-East-Down coordinate system of size 3×3. Here, $\Delta r_{ji} = |\mathbf{r}_j-\mathbf{s}_i|$ and superscripts x, y, and z denote the components of the respective vectors. Now, given N magnetic sources and K observation points, the above formulation can be generalized by rearranging the vectors $\mathbf{r}_j$ and $\mathbf{m}_i$ according to $\mathbf{r} = (\mathbf{r}_1,\ldots,\mathbf{r}_K)^T$ and $\mathbf{m} = (M_1\hat{\mathbf{m}}_1,\ldots,M_N\hat{\mathbf{m}}_N)^T$. Then,

$$\mathbf{B}(\mathbf{r}) = \mathbf{J}(\mathbf{r}_1,...,\mathbf{r}_K,\mathbf{s}_1,...,\mathbf{s}_N)\mathbf{m} \tag{3.2.4}$$

where

$$\mathbf{J}(\mathbf{r}_1,...,\mathbf{r}_K,\mathbf{s}_1,...,\mathbf{s}_N) = \begin{pmatrix} \mathbf{A}_{11}(\mathbf{r}_1,\mathbf{s}_1) & \mathbf{A}_{12}(\mathbf{r}_1,\mathbf{s}_2) & ... & \mathbf{A}_{1N}(\mathbf{r}_1,\mathbf{s}_N)\\ \mathbf{A}_{21}(\mathbf{r}_2,\mathbf{s}_1) & \mathbf{A}_{22}(\mathbf{r}_2,\mathbf{s}_2) & ... & \mathbf{A}_{2N}(\mathbf{r}_2,\mathbf{s}_N)\\ ... & ... & ... & ...\\ \mathbf{A}_{K1}(\mathbf{r}_K,\mathbf{s}_1) & \mathbf{A}_{K2}(\mathbf{r}_K,\mathbf{s}_2) & ... & \mathbf{A}_{KN}(\mathbf{r}_K,\mathbf{s}_N)\end{pmatrix} \tag{3.2.5}$$

is a matrix consisting of $N\times K$ matrices $\mathbf{A}_{ji}$ with a total size of $3N\times 3K$.

Due to short period petrogenesis (Sec. 3.1) it is assumed that all dipoles share a common magnetic orientation $\hat{\mathbf{m}}$ (Parker, 1991) and Eq. 3.2.4 can be further simplified by separation of the magnetization strength $\mathbf{M} = (M_1,\ldots,M_N)^T$ and the magnetic orientation. It is therefore possible to rearrange Eq. 3.2.3 including $\hat{\mathbf{m}}$, $\tilde{\mathbf{A}}_{ji}(\mathbf{r}_j,\mathbf{s}_i,\hat{\mathbf{m}}) = \mathbf{A}_{ji}(\mathbf{r}_j,\mathbf{s}_i)\hat{\mathbf{m}}$ to obtain

$$\mathbf{G}(\mathbf{r}_1,...,\mathbf{r}_K,\mathbf{s}_1,...,\mathbf{s}_N,\hat{\mathbf{m}}) = \begin{pmatrix} \tilde{\mathbf{A}}_{11}(\mathbf{r}_1,\mathbf{s}_1,\hat{\mathbf{m}}) & \tilde{\mathbf{A}}_{12}(\mathbf{r}_1,\mathbf{s}_2,\hat{\mathbf{m}}) & ... & \tilde{\mathbf{A}}_{1N}(\mathbf{r}_1,\mathbf{s}_N,\hat{\mathbf{m}})\\ \tilde{\mathbf{A}}_{21}(\mathbf{r}_2,\mathbf{s}_1,\hat{\mathbf{m}}) & \tilde{\mathbf{A}}_{22}(\mathbf{r}_2,\mathbf{s}_2,\hat{\mathbf{m}}) & ... & \tilde{\mathbf{A}}_{2N}(\mathbf{r}_2,\mathbf{s}_N,\hat{\mathbf{m}})\\ ... & ... & ... & ...\\ \tilde{\mathbf{A}}_{K1}(\mathbf{r}_K,\mathbf{s}_1,\hat{\mathbf{m}}) & \tilde{\mathbf{A}}_{K2}(\mathbf{r}_K,\mathbf{s}_2,\hat{\mathbf{m}}) & ... & \tilde{\mathbf{A}}_{KN}(\mathbf{r}_K,\mathbf{s}_N,\hat{\mathbf{m}})\end{pmatrix} \tag{3.2.6}$$

and calculate the vector magnetic field:

$$\mathbf{B}(\mathbf{r}) = \mathbf{G}(\mathbf{r}_1,...,\mathbf{r}_K,\mathbf{s}_1,...,\mathbf{s}_N,\hat{\mathbf{m}})\mathbf{M} \tag{3.2.7}$$

By including $\hat{\mathbf{m}}$ the matrices $\mathbf{A}_{ji}$ are reduced to column vectors $\tilde{\mathbf{A}}_{ji}$ of the size 3×1 and therefore the size of $\mathbf{G}$ is reduced to $3N \times K$ and Eq. 3.2.7 can then be inverted to yield

$$\mathbf{M} = \left(\mathbf{G}^T\mathbf{G}\right)^{-1}\mathbf{G}^T\mathbf{B} \tag{3.2.8}$$

The above calculation uses the full magnetic field vector. Parker (1991) was able to further simplify his calculation without loss of generality by using only the component aligned with the main magnetic field for the inversion. Oliveira and Wieczorek (2017), used Parkers approach, but chose the radial Down-component of the magnetic field in spherical coordinates. In this investigation we chose the one component of the vector magnetic field in the local North-East-Down coordinate system that maximized the signal to noise ratio (see Sec. 3.3.3). Because of the usually higher amplitude and less noise (Morschhauser et al., 2014) the vertical Down-component (B_z) is generally used. By only choosing one component, the size of the matrix in Eq. 3.2.6 can be further reduced. If for example the B_z-component is chosen only every third row of Eq. 3.2.6 is used for the inversion.

$$\vec{a}_{ji}(\mathbf{r}_j, \mathbf{s}_i) = \frac{\mu_0}{4\pi \cdot \Delta r_{ji}^5}\begin{pmatrix} 3(r_j^x - s_i^x)(r_j^z - s_i^z) & 3(r_j^y - s_i^y)(r_j^z - s_i^z) & 3(r_j^z - s_i^z)^2 - \Delta r_{ji}^2 \end{pmatrix} \tag{3.2.9}$$

Similar to $\tilde{\mathbf{A}}(\mathbf{r}_j, \mathbf{s}_i, \hat{\mathbf{m}})$ the magnetic orientation is included and the row vectors ($\vec{a}_{ji}$) become scalars $\tilde{\mathbf{a}}(\mathbf{r}_j, \mathbf{s}_i, \hat{\mathbf{m}})$, leading to an altered $\mathbf{G}$-matrix (Eq. 3.2.6) $\mathbf{G}_2$ with a size of $N \times K$:

$$\mathbf{G}_2(\mathbf{r}_1, ..., \mathbf{r}_K, \mathbf{s}_1, ..., \mathbf{s}_N, \hat{\mathbf{m}}) = \begin{pmatrix} \tilde{\mathbf{a}}_{11}(\mathbf{r}_1, \mathbf{s}_1, \hat{\mathbf{m}}) & \tilde{\mathbf{a}}_{12}(\mathbf{r}_1, \mathbf{s}_2, \hat{\mathbf{m}}) & ... & \tilde{\mathbf{a}}_{1N}(\mathbf{r}_1, \mathbf{s}_N, \hat{\mathbf{m}}) \\ \tilde{\mathbf{a}}_{21}(\mathbf{r}_2, \mathbf{s}_1, \hat{\mathbf{m}}) & \tilde{\mathbf{a}}_{22}(\mathbf{r}_2, \mathbf{s}_2, \hat{\mathbf{m}}) & ... & \tilde{\mathbf{a}}_{2N}(\mathbf{r}_2, \mathbf{s}_N, \hat{\mathbf{m}}) \\ ... & ... & ... & ... \\ \tilde{\mathbf{a}}_{K1}(\mathbf{r}_K, \mathbf{s}_1, \hat{\mathbf{m}}) & \tilde{\mathbf{a}}_{K2}(\mathbf{r}_K, \mathbf{s}_2, \hat{\mathbf{m}}) & ... & \tilde{\mathbf{a}}_{KN}(\mathbf{r}_K, \mathbf{s}_N, \hat{\mathbf{m}}) \end{pmatrix} \tag{3.2.10}$$

The magnetization strengths can now be calculated with the shortened $\mathbf{G}_2$-matrix in combination with a vector generated from only one component of the magnetic field (here B_z) of each observation point and a size of $K \times 1$.

$$\mathbf{M} = \left(\mathbf{G}_2^T\mathbf{G}_2\right)^{-1}\mathbf{G}_2^T\vec{B}_z \tag{3.2.11}$$

Since magnetization is assumed to be uniform, a reversal of orientation within the magnetized matter is prohibited and it is required that $M_i \geqslant 0\frac{A}{m}$ to not violate this assumption (Parker, 1991). Therefore, in order to determine $\mathbf{M}$ a nonnegative least squares algorithm is used instead of Eq. 3.2.11 (Lawson and Hanson, 1974 / App. A).

These calculations are consistently done for all possible orientations defined by the unit sphere, and the standard deviations (STDs / σ) of the SH-model ($\mathbf{B}_{SH}$) and the ESD-model ($\mathbf{B}_{ESD} = \mathbf{GM}$) are calculated with:

$$\sigma = \frac{1}{\sqrt{K}}\|\mathbf{B}_{SH} - \mathbf{B}_{ESD}\|_2 \tag{3.2.12}$$

The minimum standard deviation (σ_{min}) thereby defines the best fitting model.

Using trigonometry (Butler, 1992 / Sec. 1.3), and the calculated magnetic orientation in combination with the center location of the anomaly it is possible to calculate the best fitting magnetic South Pole position. In a similar way, pole locations of each of the magnetic orientations defined by the unit sphere can be determined to generate a confidence interval, displaying standard deviations according to their location on the Martian surface (Fig. 4.3).

3.3 CONSTRAINING MODELING RESULTS

To constrain the number of possible magnetic orientations within the confidence interval, a measure $\mathbf{I}_{min}$ was defined as the confidence limit threshold. It has to satisfy $\mathbf{I}_{min} \geqslant \sigma_{min}$ and ideally $\mathbf{I}_{min} < \sigma_{max}$. In order to define $\mathbf{I}_{min}$ different approaches have been implemented and tested, which are presented in the following section. In the beginning it was tested if the SH-model's covariance matrix (Morschhauser et al., 2014) can be used to calculate the errors ΔB_x, ΔB_y, and ΔB_z of every observation point. Next it was tested if the number of calculated models can be minimized by testing if the components of $\mathbf{B}_{ESD}$ lie within the K-dimensional error ellipsoid, which can be determined from the covariance matrix and its specific Eigenvalues and Eigenvectors. In a last approach it was investigated how magnetic anomalies in the vicinity of the observation (Oliveira and Wieczorek, 2017) and non-uniformly magnetized regions alter the observed magnetic signal and how this alteration transfers to an altered paleopole location.

3.3.1 *Error estimation using the covariance matrix of the SH-model*

The covariance is an attribute in stochastics for the connection between two random variables. Each covariance value gives insight if high values of one parameter either correlate with high, or low values of another parameter. In a simple example with two parameters x and y, high values of x correlate with high values of y and low values correlate with low values if the covariance > 0. If the covariance < 0, low values of x correlate with high values of y, and vice versa. In the case covariance = 0, no monotone dependencies are present between x and y.

The covariance matrix $\mathbf{C}$ contains information about the scatter, e.g. in a random data vector $\vec{d} = (x_1, ..., x_n)^T$ and the correlation of its components can be written as (Aster et al., 2013):

$$\mathbf{C}(d) = \left[A(x_i, x_j)\right]_{i,j=1,...,n} = \begin{pmatrix} C(x_1, x_1) & C(x_1, x_n) \\ C(x_n, x_1) & C(x_n, x_n) \end{pmatrix} \tag{3.3.1}$$

The matrix contains the variances of the random vector in its main diagonal, therefore every element on the diagonal is larger than zero. A real covariance matrix is symmetric and positive semidefinite. This implies that the matrix can be split into a real orthogonal matrix $\mathbf{Q}$ of Eigenvectors $\mathbf{P}$ and a real diagonal matrix Λ of Eigenvalues $\mathbf{A}$.

$$\mathbf{C} = \mathbf{Q}\Lambda\mathbf{Q}^T \tag{3.3.2}$$

In the case of independent and regularly distributed errors Δd within $\vec{d}$, the covariance matrix for the data vector is calculated as

$$\mathbf{C}(d) = \Delta d^2 \cdot E_m \tag{3.3.3}$$

with E_m as the unit matrix.

Now the covariance matrix of the characterizing parameters of the model (Sec. 3.2), e.g. the magnetization strength **M**, are

$$\mathbf{C}(\mathbf{M}) = \Delta d^2(\mathbf{G}^T\mathbf{G})^{-1} \tag{3.3.4}$$

For a general case with a random error distribution the covariance matrix for the inversion result (Eq. 3.2.8) is calculated using an inversion matrix weighted by the errors ($\mathbf{G}_w$) and a weighted covariance matrix for the data vectors $\mathbf{C}(d_w)$ (Aster et al., 2013).

$$\mathbf{C}(\mathbf{M}) = (\mathbf{G}_w^T\mathbf{G}_w)^{-1}\mathbf{G}_w^T\mathbf{C}(d_w)\mathbf{G}_w(\mathbf{G}_w^T\mathbf{G}_w)^{-1} \tag{3.3.5}$$

From the covariance matrix, we can now take the 95% confidence interval to obtain error bars for the inversion result. Note that for the inversion described in Sec. 3.2 the result is the vector of magnetization strength **M** of the distributed dipoles and therefore the calculated error bars relate to the confidence limit threshold in magnetization strength:

$$\Delta\mathbf{M} = \pm 1.96 \cdot diag(\mathbf{C}(\mathbf{M}))^{\frac{1}{2}} \tag{3.3.6}$$

To calculate the error bars of the vector magnetic field components derived from the ESD-model, $\Delta\mathbf{M}$ has to be multiplied with the inversion matrix **G** (Eq. 3.2.6).

$$\Delta\mathbf{B}_{ESD} = \mathbf{G}\Delta\mathbf{M} \tag{3.3.7}$$

Using only the diagonal of the covariance matrix is usually sufficient to estimate the errors related to the inversion results. However, the off-diagonal components can hold relevant information for the definition of the confidence limit threshold (Fig. 11). To include the off-diagonal components the covariance matrix has to be inverted. Then the Eigenvectors **P** and Eigenvalues **A** together with the 95th percentile $F^{-1}_{\chi^2,N}(0.95)$ have to be determined. The 95th percentile depends on the χ^2 distribution and hence on the degrees of freedom (N) used in the inversion. The 95% ellipsoid semi-major axis lengths are then given by:

$$A_L = \sqrt{F_{\chi^2,N}}^{-1} \cdot \frac{1}{\mathbf{A}} \tag{3.3.8}$$

Finally the variations $\Delta\mathbf{M}$ are calculated and the maximum variation is taken as the confidence limit threshold for the modeling results, where

$$\Delta\mathbf{M} = |\mathbf{P} \cdot A_L|. \tag{3.3.9}$$

The covariance matrix provided by Morschhauser et al. (2014) for the SH-model contains the covariances between the Gauss coefficients g_l^m (Sec. 2.2.2). The first coefficient defines the row and the second coefficient defines the column in which the covariance is written and it is distinguished between three cases:

1. The row, or column of a coefficient with $m > 0$ is $l^2 + 2|m| - 1$
2. The row, or column of a coefficient with $m < 0$ is $l^2 + 2|m|$
3. The row, or column of a coefficient with $m = 0$ is l^2

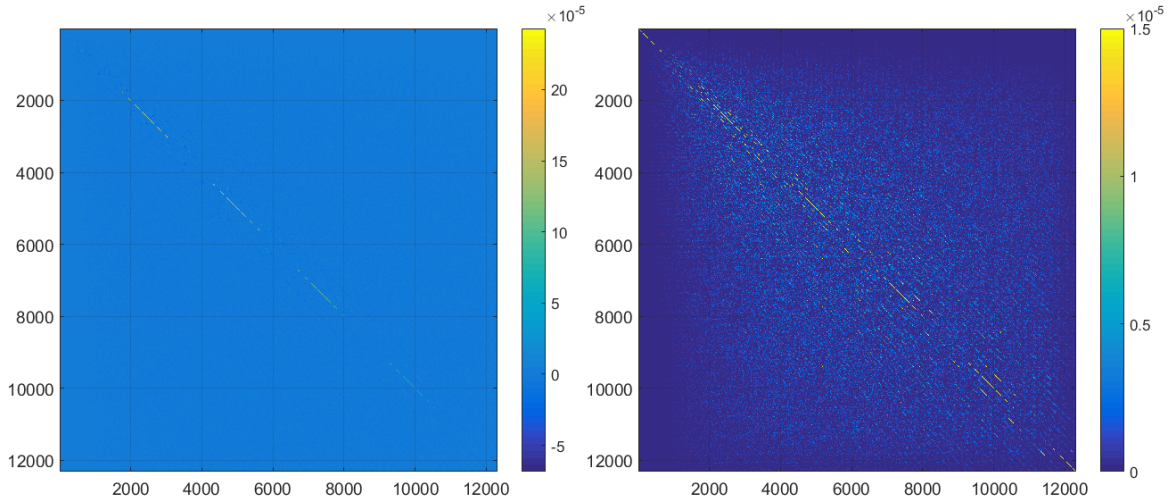

Figure 11: The left side of the figure shows the variances of the gauss coefficients in full range from the minimum of $-6.845 \cdot 10^{-5}$ to the maximum variance on the main diagonal of $24.294 \cdot 10^{-5}$. On the right side the range was limited to variances between 0 and $1.5 \cdot 10^{-5}$ to show the off-diagonal variances.

Using Eq. 2.2.6 to calculate the components of the vector magnetic field under exclusion of the Gauss coefficients, each covariance matrix ($\mathbf{C}_x$, $\mathbf{C}_y$, $\mathbf{C}_z$) for every component of the vector magnetic field can be determined under full use of the covariance matrix of the Gauss coefficients. Each matrix has a size of 12320×12320 given by the degree and order 110. The minimum value in the covariance matrix is $-6.845 \cdot 10^{-5}$ and the maximum value is $24.294 \cdot 10^{-5}$. Due to the fact that the diagonal contains only elements that are larger than zero, the negative values indicate that the off-diagonal components show significant variances. This is shown in Fig. 11. On the right side of the figure the variances are reduced to a range between 0 and $1.5 \cdot 10^{-5}$ and apart from the highest variances which lie on the main diagonal it can be seen that variances larger than zero can be found in the off-diagonal which decrease towards $\mathbf{C}(x_1, x_n)$ and $\mathbf{C}(x_n, x_1)$. Therefore, it seemed necessary to use the full covariance matrix to determine the errors. However, while the determined errors obtained from the diagonal only did not exceed 0.1 nT, the full content of the covariance matrix led to a significant increase with errors reaching 1000% of the vector magnetic fields magnitude. For this reason it was not possible to use the covariance matrix to determine a confidence limit threshold for the uncertainty of the model, because the limit was either to small to even include the best fitting model, or to large and therefore allow for all models to be admissible.

3.3.2 *Error ellipsoid fit using the covariance matrix and the principal axis theorem*

As explained in the previous section, an estimate of the error could not be determined from the covariance matrix. However, in principle a K-dimensional error ellipsoid can be determined from the Eigenvalues **A** and Eigenvectors **P** and it can be tested if the results $\mathbf{B}_{ESD}$ fit within the ellipsoid.

In the following the principal axis theorem is explained for the two-dimensional and three-dimensional case, to create axially parallel error ellipsoids and test if a data point of a certain data set lies inside the ellipsoid. A two-dimensional ellipse in the x-y-coordinate system can be described by

$$ax^2 + 2bxy + cy^2 + dx + ey + f = 0 \tag{3.3.10}$$

Where a and c control the elongation of the ellipse, b its orientation in the coordinate system, d and e the location of the center and f scales the semi-major axis lengths. If $b = 0$ the ellipse is axially parallel in the x-y-coordinate system and it can easily be tested if a point with the coordinates (x_1, y_1) lies within the ellipse. However, if $b \neq 0$ and the ellipse is not axially parallel to x and y, a new coordinate system has to be found. Therefore, the principal axis theorem is used. To do so Eq. 3.3.10 is changed into matrix form

$$(x \;\; y) \cdot \begin{bmatrix} a & \frac{b}{2} \\ \frac{b}{2} & c \end{bmatrix} \cdot \begin{pmatrix} x \\ y \end{pmatrix} + [d \;\; e] \cdot \begin{pmatrix} x \\ y \end{pmatrix} + f = 0 \tag{3.3.11}$$

As an example let us consider the following two-dimensional ellipse:

$$9x^2 - 2\sqrt{3}xy + 7y^2 - 20 = 0 \tag{3.3.12}$$

Choosing: $\mathbf{C} = \begin{bmatrix} a & \frac{b}{2} \\ \frac{b}{2} & c \end{bmatrix} = \begin{bmatrix} 9 & -\sqrt{3} \\ -\sqrt{3} & 7 \end{bmatrix}$ it is now possible to determine the Eigenvalues $\mathbf{A}$ and the Eigenvectors $\mathbf{P} = [\vec{e}_1 ... \vec{e}_n]$ from the characterizing polynomial:

$$\mathbf{A} = \begin{pmatrix} \lambda_1 \\ \lambda_2 \end{pmatrix} = \begin{pmatrix} 10 \\ 6 \end{pmatrix} \text{ and } \mathbf{P} = [\vec{e}_1 \;\; \vec{e}_2] = \begin{bmatrix} -3 & 1 \\ \sqrt{3} & \sqrt{3} \end{bmatrix}$$

Using $\mathbf{P}$ a coordinate transformation from the x-y- into the ξ-η-coordinate system can be performed with:

$$x = -3\xi + 1\eta \text{ and } y = \sqrt{3}\xi + \sqrt{3}\eta \tag{3.3.13}$$

and the ellipse equation is determined:

$$\lambda_1 \xi^2 + \lambda_2 \eta^2 = 20 \quad \rightarrow \quad \frac{\xi^2}{2} + \frac{3\eta^2}{10} = 1 \tag{3.3.14}$$

This leads to the semi-major axis $h_a = \sqrt{2}$ and $h_b = \sqrt{\frac{10}{3}}$ and the apex points $\left(\pm\sqrt{2}, 0\right)$, $\left(0, \pm\sqrt{\frac{10}{3}}\right)$ in the ξ-η-coordinate system. With the apex points in the ξ-η-coordinate system the apex points of the x-y-coordinate system can be calculated using Eq. 3.3.13. As for a three dimensional principal axis transformation the method is the same, starting with an equation including the three dimensions.

$$(x_1 \;\; x_2 \;\; x_3) \cdot \begin{bmatrix} a & b & c \\ b & d & e \\ c & e & f \end{bmatrix} \cdot \begin{pmatrix} x_1 \\ x_2 \\ x_3 \end{pmatrix} + (g \;\; h \;\; i) \cdot \begin{pmatrix} x_1 \\ x_2 \\ x_3 \end{pmatrix} + j = 0 \tag{3.3.15}$$

Leading to the ellipsoid equation

$$\frac{(\xi_1 - \alpha_1)^2}{h_a^2} + \frac{(\xi_2 - \alpha_2)^2}{h_b^2} + \frac{(\xi_3 - \alpha_3)^2}{h_c^2} = 1, \tag{3.3.16}$$

with α_1, α_2 and α_3 as the coordinates of the center of the ellipsoid, whereby the ellipsoids center lies at (0,0,0) if $\alpha_1 = \alpha_2 = \alpha_3 = 0$. The K-dimensional ellipsoid is defined in a way similar to Eq. 3.3.15, using a vector $\vec{X}$ with length K, including the coordinates of a point, the K by K matrix $\mathbf{C}$, a column-vector $\vec{H}$ with K parameters and a constant j.

$$\vec{X}^T \cdot \mathbf{C} \cdot \vec{X} + \vec{H} \cdot \vec{X} + j = 0 \tag{3.3.17}$$

The equations of the error ellipsoids for $\Delta\vec{B}_x$, $\Delta\vec{B}_y$ and $\Delta\vec{B}_z$, and therefore the corresponding $\vec{H}$ and j are unknown, but with the covariance matrix of the Gauss coefficients the matrices $\mathbf{C}_x$, $\mathbf{C}_y$, $\mathbf{C}_z$ can be determined and this leads to the Eigenvectors $\mathbf{P}_x$, $\mathbf{P}_y$, $\mathbf{P}_z$ and the corresponding Eigenvalues $\mathbf{A}_x$, $\mathbf{A}_y$ and $\mathbf{A}_z$. With the χ^2-distribution of the Gauss coefficients, the lengths of the K semi-major axis can be calculated.

If the original ellipsoid is off center the coordinate systems origin (Eq. 3.3.16) the off center components also have to be calculated. Therefore, the center points in the $x_1 - x_K$, $y_1 - y_K$, and $z_1 - z_K$ coordinate systems are transformed into new ξ_1 - ξ_K (3.3.18), η_1 - η_K (3.3.19), and ρ_1 - ρ_K (3.3.20) coordinate systems, respectively.

$$\vec{\xi} = \left(\mathbf{P}_x^T \cdot \mathbf{P}_x\right)^{-1} \cdot \vec{x} \tag{3.3.18}$$

$$\vec{\eta} = \left(\mathbf{P}_y^T \cdot \mathbf{P}_y\right)^{-1} \cdot \vec{y} \tag{3.3.19}$$

$$\vec{\rho} = \left(\mathbf{P}_z^T \cdot \mathbf{P}_z\right)^{-1} \cdot \vec{z} \tag{3.3.20}$$

In the same way as the center points, the values from the inversion are transformed into the new coordinate system using the Eq. 3.3.18, 3.3.19 and 3.3.20, with the negative of the center points being the off-center points ($\vec{\alpha}$, $\vec{\beta}$, $\vec{\gamma}$).

Now it can be tested if a value of the vector magnetic field derived from the model lies within the error ellipsoid. As an example, Eq. 3.3.16 is reduced to the three dimensional case.

$$\begin{aligned} F(\xi_1, \xi_2, \xi_3) = (\xi_1 - \alpha_1)^2 \cdot h_b^2 h_c^2 + (\xi_2 - \alpha_2)^2 \cdot h_a^2 h_c^2 \\ + (\xi_3 - \alpha_3)^2 \cdot h_a^2 h_b^2 - h_a^2 h_b^2 h_c^2 \end{aligned} \tag{3.3.21}$$

It is stated, that for

- $F(\xi_1, \xi_2, \xi_3) = 0$ the observed point lies on the ellipsoids surface
- $F(\xi_1, \xi_2, \xi_3) < 0$ the observed point lies within the ellipsoid
- $F(\xi_1, \xi_2, \xi_3) > 0$ the observed point lies outside the ellipsoid

K-dimensional error ellipsoids were calculated and it was tested if the calculated components of the vector magnetic field $\mathbf{B}_{ESD}$ fit within their respective ellipsoids. It could be observed that the more dimensions are introduced, the more the differences increase between the minimum and maximum semi-major axis length. As an example the ellipsoid calculation for an anomaly at the location 64.5° S / 28.5° E was chosen and the magnetic field in the altitude of 120 km was calculated within a radius of 7°. Dipole distributions of 7, 19, 61, and 241 were chosen to calculate the vector magnetic field and the corresponding ellipsoids were derived for every component of the vector magnetic field. The number of dimensions for each ellipsoid is equal to the number of distributed observation points. For comparison, the smallest ($\mathbf{s}_c$), and longest ($\mathbf{s}_a$) semi-major axis for the discussed dimensions are listed in Tab. 2, in combination with a third length $\mathbf{s}_b$ selected from positions 4, 9, 31, and 121 of the semi-major axis length's array.

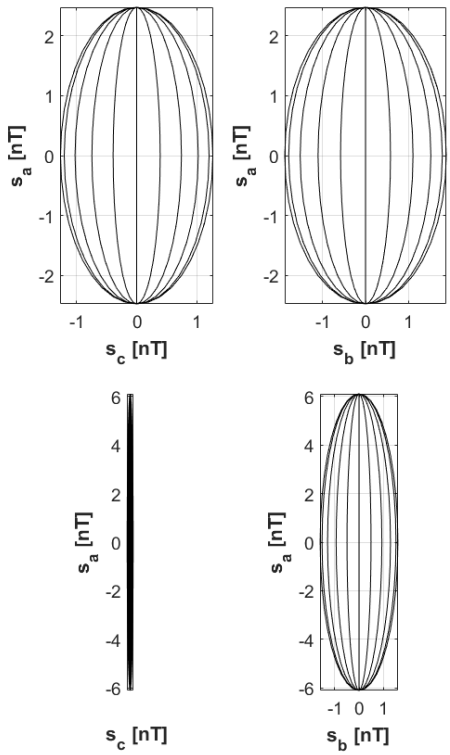

Figure 12: Shown are the shortest ($\mathbf{s}_c$) and longest ($\mathbf{s}_a$) semi-major axis, as well as an axis $\mathbf{s}_b$ selected from a mean position of the semi-major axis array. Lengths were obtained from the B_z-component of 7 observation points (top) and 19 observation points (bottom).

In Tab. 2 and Fig. 12 it can be seen that the differences between the semi-major axis lengths increase dependent on the number of dimensions. While for 7 dimensions the lengths $\mathbf{s}_a$, $\mathbf{s}_b$, and $\mathbf{s}_c$ are in the same order of magnitude, the $\mathbf{s}_c$ axis for 19 dimensions is more then ten times smaller than the corresponding $\mathbf{s}_b$ axis. This becomes obvious in the bottom part of Fig. 12 where the three chosen axes of the 19-dimensional ellipsoid are shown. The 2D representation of the ellipsoid on the left hand side shows a close to string like ellipse, which is not surprising with a more than 50 times longer $\mathbf{s}_a$-axis in comparison to the $\mathbf{s}_c$-axis.

In comparison, the lengths of the 7-dimensional ellipsoid are more balanced (top of Fig. 12 / Tab. 2). Therefore, fitting data in the 7 dimensional ellipsoid could be possible, as long as the best fitting STD is smaller than the shortest semi-major axis length ($\mathbf{s}_c$). However, for ellipsoids of higher dimensions, the ellipsoids shape becomes more and more string like and already for 19 dimensions a model fit in direction of $\mathbf{s}_c$ seems unlikely, because a STD below 0.12 nT needs to be achieved (Fig. 12 / bottom). The strongest variation for this example is found for the 241-dimensional case, with a difference of 10^9 nT between the shortest and largest semi-major axis (Tab. 2).

For the investigation we generally use 241 dipoles. With a difference between minimum and maximum semi-major axis of $\sim 10^9$ nT the resulting ellipsoids had string like shapes for all investigated anomalies, whereby the calculated vector magnetic field components fit the longest semi-major axis, but none fit the shortest. Therefore, similar to the investigation of the covariance matrix it was not possible to estimate a confidence limit threshold $\mathbf{I}_{min}$ from the calculation of the error ellipsoids. In the beginning it was thought that due to the principal axis theorem a constraint could be estimated, but the high length

variations are a direct cause of the strong variances (Sec. 3.3.1) within the covariance matrix, which define the Eigenvalues and therefore scale the lengths of the semi-major axes.

Table 2: Given are the lengths in nT of the longest ($\mathbf{s}_a$), shortest ($\mathbf{s}_c$) and a third axis ($\mathbf{s}_b$) from the semi-major axis array for four different n-dimensional ellipsoids.

Dimensions	$\mathbf{s}_a$ [nT]	$\mathbf{s}_b$ [nT]	$\mathbf{s}_c$ [nT]
7	2.47	1.88	1.26
19	6.11	1.59	0.12
61	19.28	0.03	$1.49 \cdot 10^{-5}$
241	25.09	$4.57 \cdot 10^{-7}$	$5.48 \cdot 10^{-8}$

3.3.3 *Estimation of data noise*

A different approach to estimate a confidence limit threshold was introduced by Oliveira and Wieczorek (2017). It is based on the assumption that a measured magnetic signal of an observed magnetic anomaly is altered by perturbing signals from magnetic anomalies in the vicinity. In addition, signal alterations from inside the anomaly can be present, because a completely uniform magnetization is rather unlikely under natural conditions. The actual orientation of single volume elements of the sources main body can differ compared to the main orientation due to e.g. different cooling periods, varying mineral compositions or a rare event of self reversal (Gubbins and Herrero-Bervera, 2007; Tarling, 2007). Non-uniformity might appear more frequently at the edges of anomalies, due to higher chances of varying petrogenetic environments. Therefore, the strongest signal alteration should appear at the boundary of the observed anomaly and the calculation of the average field at that location gives an estimate of the confidence limit threshold $\mathbf{I}_{min}$.

In the modeling process the anomaly's size is estimated with R_0. By choosing the observation point distribution $R_s = R_0 + 1°$, an annulus with a thickness of 1° is created at the boundary of the observed anomaly. It is now possible to determine the average field in this annulus by calculating the root mean square, in the following denoted $\mathbf{I}$, of all observation points which are located in the annulus.

It is an objective to find the radii combination R_0 and R_s with the least perturbation that minimizes $\mathbf{I}$, which is then taken as the confidence limit threshold $\mathbf{I}_{min}$. For this purpose a method was developed to automatically search for the minimum $\mathbf{I}$, using varying sizes and center locations of R_0. Fig. 13 (left) is a scheme of the basic principle of this method. Imagine the visually detected center of the anomaly lies at 0° longitude and 0° latitude at the location marked 25. Now a grid of 49 locations is generated within a square of $6° \times 6°$ around the center. Starting with location number 1 at −3° longitude / 3° latitude $\mathbf{I}(R)$ is calculated for increasing radii R at this location. R defines the inner radius of the annulus starting with $R = 0.5°$ and continuing with an increment of 0.5° until $R = 10.5°$ is reached. For each location (1 to 49) a curvature $\mathbf{I}(R)$ (Fig. 13 / right) is determined with $\mathbf{I}_0^n$ as the average field of $\mathbf{B}_{SH}$ for $R < 0.5°$ and $\mathbf{I}_{min}^n$ ($1 \leqslant n \leqslant 49$) as the confidence limit threshold at that location. With the obtained values for $\mathbf{I}_0^n$ and $\mathbf{I}_{min}^n$ the signal to noise ratio (SNR) as a measure of the anomalies isolation is calculated

$$SNR = \mathbf{I}_0^n / \mathbf{I}_{min}^n \tag{3.3.22}$$

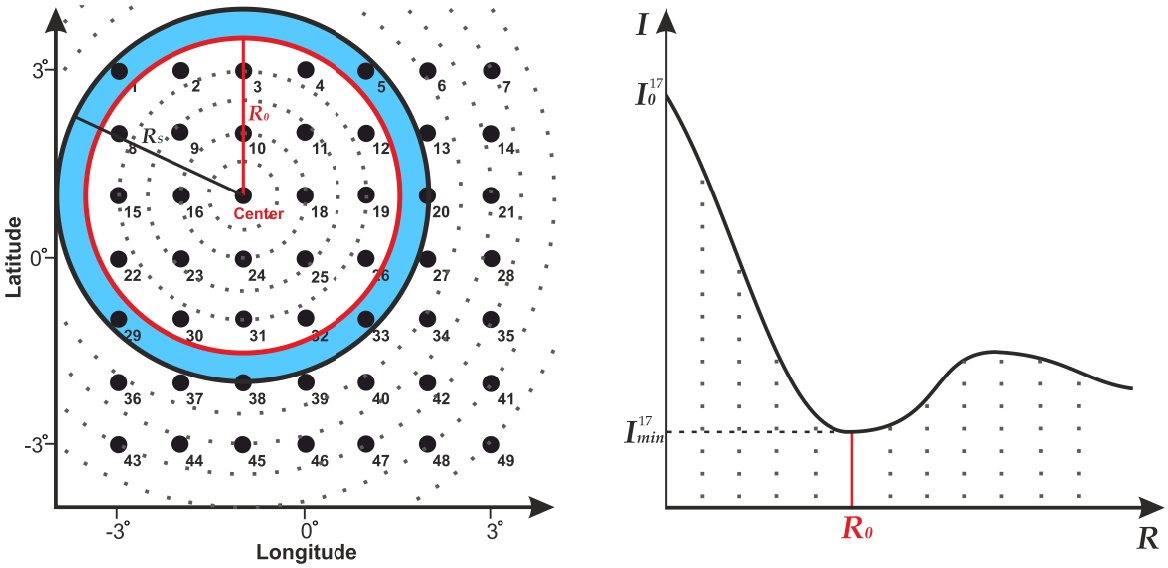

Figure 13: Illustration of the method to determine the minimum confidence limit threshold $\mathbf{I}_{min}$ and the dipole distribution radius R_0. The visually selected center of the anomaly is located at point 25, and a regular grid of 6° by 6°, with 7 points distributed on 6°, is generated around the visual center. $\mathbf{I}(R)$ is determined for each grid point as shown on the right side of the figure by calculating the the root mean square of the magnetic field within rings (blue) of increasing radii (dotted circles). The center of observation (**Center**) is then chosen to be the grid point at which $\mathbf{I}_0$ and $\mathbf{I}_{min}^n$, $1 \leqslant n \leqslant 49$, maximize the SNR and $\mathbf{I}_{min}$, R_0 (red circle), and R_s (black circle) are determined for this center location. A similar figure was published in Thomas et al. (2018).

and the maximum SNR obtained from the 49 locations defines the most suitable configuration. The radius R at which the maximum SNR was determined then equals R_0. In the shown example (Fig. 13) the highest SNR was obtained at location 17 (marked **Center**), with $\mathbf{I}_{min}^{17}$ as the confidence limit threshold maximizing the SNR. The radius R_0 at which $\mathbf{I}_{min}^{17}$ was determined is shown as a red circle in combination with R_s and the corresponding circle in black, bounding the annulus (blue).

In the beginning of this section it was explained that it is an objective for the determined confidence limit threshold to be larger than the minimum STD ($\mathbf{I}_{min} \geqslant \sigma_{min}$), in order for the model to fit and ideally $\mathbf{I}_{min} < \sigma_{max}$, to be able to constrain the number of admissible models. As explained in Sec. 3.2 a model for every possible orientation on the unit sphere is calculated and the corresponding STDs determine the confidence interval. Each orientation is related to a location on the planet and therefore each location is linked to a STD. If $\mathbf{I}_{min}$ is smaller than σ_{max} admissible locations are reduced to those whose STD is equal to $\mathbf{I}_{min}$ or below. The remaining locations form the area of admissible paleopole locations. Its areal coverage is calculated using a Delaunay-triangulation, which combines triplets of the remaining locations to form triangles. Then the area of each triangle is calculated and the sum gives the total area of admissible paleopole locations.

With this method it is possible to search for isolated magnetic field anomalies according to the SNR, using the SH-model by Morschhauser et al. (2014) (Sec. 5.1). Furthermore, by constraining areas of admissible paleopole locations with the value of $\mathbf{I}_{min}$ an uncertainty in determined paleopole locations is given, which was often missing in previous studies (Sec. 1.4).

4

MODEL EVALUATION AND SENSITIVITY ANALYSIS

After implementing the ESD method and evaluating constraints, different synthetic analyses were performed in order to test the determined results and the robustness of noise related constraints on the area of admissible paleopole locations. Therefore, simple magnetic sources were generated and reconstructed using ESDs (Sec. 4.1). These simple sources were then altered by noise (Sec. 4.2) and by a second anomaly in the vicinity of observation (Sec. 4.3).

4.1 SIMPLE SOURCE RECONSTRUCTION

At first a simple test scenario was generated to investigate if the implemented inversion can precisely reconstruct a given magnetic orientation. For this test we consider a global magnetic field with a magnetic South Pole location at 50° S / 130° E, which magnetizes a spherical source. A 2D-scheme of this configuration is shown in part a of Fig. 14. The synthetic source, represented by the red-blue circle, has a radius of 5 km and is located at a depth of 20 km from the surface, at 30° S / 90° E. Its magnetization strength is $5 \cdot 10^3 \frac{A}{m}$, with a magnetic orientation of $I = 70°$ and $D = 135°$ (black arrow). At the locations marked with black dots the magnetic field $\mathbf{B}_o$, generated by the spherical source, is calculated. Further, the B_z-component (gray line) with a magnitude of $\sim$ 150 nT at an altitude of 120 km is shown. As explained in Sec. 3.2 the spherical source is now synthesized with a distribution of 241 dipoles (ESDs) of uniform orientation within a radius R_0 (Fig. 14 / b) and again the magnetic field $\mathbf{B}_{ESD}$, now generated by the ESD distribution, is determined for observation point distributions within the radius R_s.

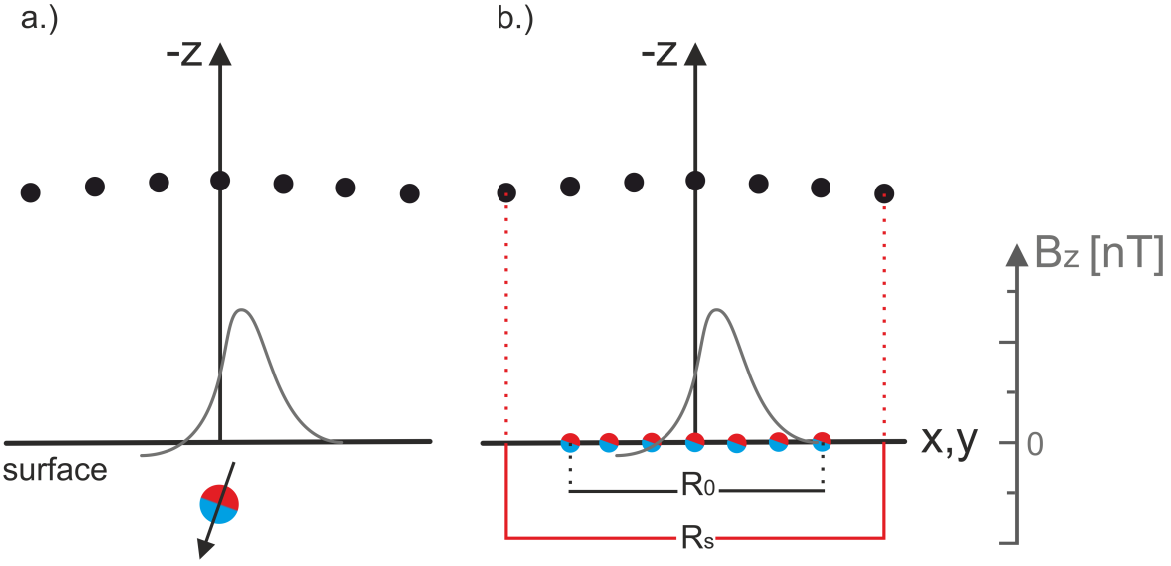

Figure 14: Representation of the magnetic fields B_z-component in a local North-East-Down (x, y, and z) coordinate system as derived from a single spherical source in a depth of 20 km (a) and from a distribution of equal distanced dipoles at the surface (b). Black dots indicate the locations of observation points at an altitude z, which are distributed within the radius R_s. R_0 coresponds to the dipole distribution radius.

It was an objective to vary the radii R_0 and R_s in size to obtain a configuration where the misfit between $\mathbf{B}_0$ and $\mathbf{B}_{ESD}$ is minimized. Similar to Sec. 3.3.3 the radius R_0 was therefore stepwise increased in size from 1° to 10°, with $R_s = R_0 + 1°$ and the magnetic fields $\mathbf{B}_0$ and $\mathbf{B}_{ESD}$ where calculated and analysed. As an example, Fig. 15 shows the three components of the vector magnetic field (B_x, B_y, and B_z) as derived from the spherical source at the top, the three components calculated from the ESD-model in the middle and the calculated residuals at the bottom of the figure for a radius of $R_0 = 4°$ (red circle). It is evident from Fig. 15 that an overall good fit of the ESD-model in comparison to the magnetic field from the spherical source exists. Residuals are around 3 nT, or 0.2% of the magnitude of the magnetic field, respectively. The highest residuals tend to be found at the edges of the model, a feature which can similarly be found in all observations from $R_0 = 1°$ up to $R_0 = 10°$. The absolute value of the residuals decreases with increasing R_0. For example for a dipole distribution radius of $R_0 = 1°$ residuals exceed 3 nT, whereby at $R_0 = 10°$ only residuals of 0.01 nT remain. This is due to a consistent pattern which was found in the dipole distribution. The strongest dipole is located in the center of the observation with a magnetization strength of $\sim 6 \cdot 10^{14} \frac{A}{m}$. This central dipole is surrounded by six dipoles at 1° distance to the center, which show only around one third of the central magnetization strength. All remaining dipoles show either no magnetization, or their strength is reduced by at least one order of magnitude. The high magnetization at the off-center location leads to the high residuals at the edges for smaller radii, because the most distant observation points are close to the off-center dipoles. This imprints also on the calculated confidence interval which significantly decreases towards greater radii.

However, a homogeneous spherical source might possibly be not a realistic representation of a magnetic source, due to a possible decrease in the achievable strength of magnetization at the edges of the embedded volume, caused by varying conditions during the petrogenesis. For this reason rather than a spherical source, an equidistant distribution of point sources was chosen. Therefore, 241 point sources were distributed in a radius of 2.5°. The magnetization strengths of the sources followed a Gaussian distribution. As a result the strongest magnetic field was obtained in the center of the anomaly and the field decreased to ~ 10% of the signals strength, at 2.5° distance from the center. Due to this configuration, the residuals were no longer reduced to the periphery only, if the radius R_0 for the inversions dipole distribution was of similar size, or larger than 2.5°. The edge effects caused by the spherical source of constant magnetization vanished and residuals were decreased. For example, the residuals were at maximum ~ 0.1 nT for radii under three times the source radius ($R_0 < 7.5°$), but increased for larger radii. This implies that for a more natural magnetization strengths distribution the model obtaining the lowest residuals is not necessarily the model with the highest R_0, as it was obtained for the spherical source, but the model with the radius R_0 being similar to the size of the anomaly's source body. As a matter of fact the lowest residuals were achieved for a dipole distribution within a radius of $R_0 = 2.5°$.

Anyways, independent of the chosen source, the model was always able to determine the input orientation of $I = 70° / D = 135°$.

4.2 THE INFLUENCE OF NOISE ON THE SOURCE RECONSTRUCTION

In order to asses how a randomly oriented background field influences the determined paleopole location another test case with a source of 2.5° radius and a distribution of 241

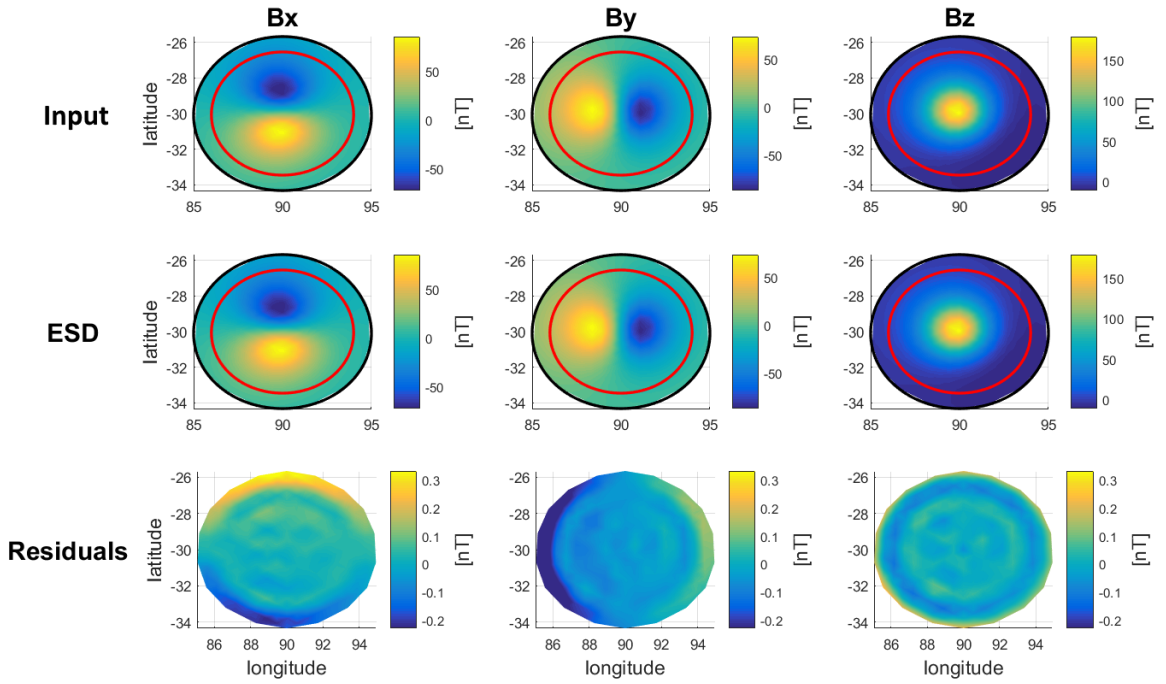

Figure 15: Modeling result of the investigation of a spherical source with a radius of 5 km located at a depth of 20 km. At the top the magnetic field as calculated from the input source is given with its B_x- (left), B_y- (middle), and B_z-component (right). The middle part shows the magnetic field components from the determined ESD model and the bottom part shows the residuals between input and the model.

dipoles was generated. The anomaly was located at 0° N and 180° E and all dipoles had a uniform orientation with I = 90° and D = 0° to make use of the full magnetic field strength in the B_z-component, which is used for the inversion. The magnetic field strength was chosen to be 300 nT at the center of the anomaly and again declined to 10% of the center strength at a distance of 2.5°. For the test random noise of different intensity was added to all components of the magnetic field. In total four noise cases were created, corresponding to background field strengths with 0%, 5%, 10%, and 25% of the maximum field strength (Tab. 3).

Table 3: Results of synthetic tests considering an anomaly at 0° N and 180° E for a paleopole at the same location. The amount of background noise (Noise) is given along with the corresponding minimum misfit (σ_{min}), the maximum field strength (B_{max}), the confidence limit threshold ($\mathbf{I}_{min}$), the inclination and declination (I/D), the signal to noise ratio (SNR), as well as the surface area coverage of admissible locations (Area).

Noise	σ_{min} [nT]	B_{max} [nT]	$\mathbf{I}_{min}$ [nT]	I/D	SNR	Area
0%	0.05	290.7	1.9	90° / 0°	121/1	0%
5%	3.6	304.6	8.6	89° / 356°	35/1	3.4%
10%	16.8	319.8	17.0	86° / 14°	19/1	5.8%
25%	45.9	335.6	47.8	81° / 270°	7/1	23.7%

As is evident from Tab. 3, an increasing background field increases the confidence limit threshold $\mathbf{I}_{min}$ as well as the minimum attainable misfit σ_{min}. The variance in **I**(R) is shown in Fig. 16 and was calculated using the method described in Sec. 3.3.3. In Fig. 16

the lines correspond to the calculated $\mathbf{I}(R)$ of a single anomaly with no (green), 5% (blue), 10% (red), and 25% (cyan) added noise. It can be seen in the figure that the undisturbed magnetic field shows a high gradient within the source region, which strongly decreases the average magnetic field as far as 3.5° from the center. Then continuing with a lower gradient, the average field converges to 0 nT at greater distances. With the addition of noise the level of background field is increased at distances greater than 3°, e.g. for the cases of 10% and 25% convergence is towards 20 nT and 50 nT, respectively. Therefore, the SNR decreases (Tab. 3) and the misfit between the model and the input field is increased in correspondence to the applied noise.

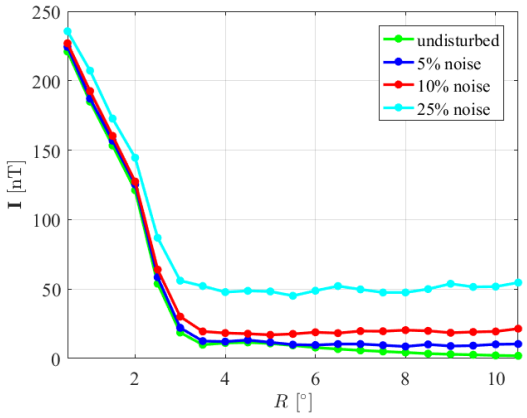

Figure 16: The average field $\mathbf{I}$ as a function of the radius R for the four cases with applied noise. Shown are the results for single anomalies with no (green), 5% (blue), 10% (red), and 25% (cyan) added noise.

As a result, the calculated magnetic orientations are altered and the determined areas of admissible paleopole locations increase significantly once a noise level of 10% is reached. For the case of 25% noise, the areas of admissible paleopole locations extend over 23.7% of the planet and as σ_{min} grows to be of the same order as $\mathbf{I}_{min}$ a fit to the data becomes nearly impossible.

In Fig. 17 the areal coverage of the admissible paleopole locations for the cases of 10% (a) and 25% (b) random noise are shown in a Robinson projection. Whilst for the 10% case the area hardly exceeds a distance of 30° to the equator, covering an area below 6%, the area extents to ±60° distance to the equator, corresponding to an areal coverage of nearly 25% of the planet. Furthermore, the strong random noise leads to a slightly shifted location for the best fit, related to the 9° and 90° misfits in inclination and declination (compare Tab. 3, I/D).

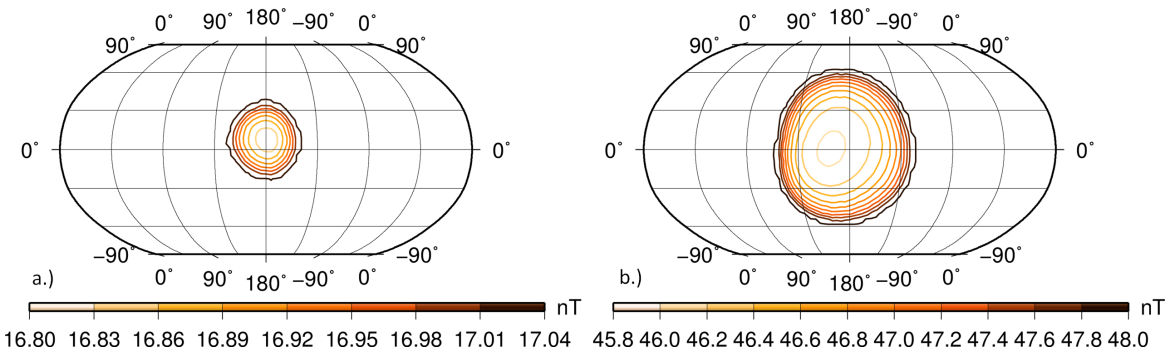

Figure 17: The two Robinson projections show the determined areas of admissible paleopole locations for test cases with additional 10% (a) and 25% (b) noise.

4.3 INVESTIGATION OF NON-ISOLATED SOURCES

As pointed out in the Sec. 4.2, additional noise significantly increases the level of background fields and therefore increases the determined areas of admissible paleopole locations. However, while a background field is most likely present, its strength might not exceed 5% and the resulting signal alteration could be negligible. Under the assumption that geologic units of similar mineral content, but different ages are located next to each other, it seems plausible that magnetic sources of similar magnitude can be preserved within the units. Therefore, the most robust scenario for intense signal alteration is given by perturbation from anomalies in the vicinity of the observation. For this reason another test was generated by placing a second identical distribution of dipoles at distances of 5° and 7.5° to the anomaly described in the previous section. For each distance the same three scenarios were investigated, corresponding to the situations expected to be encountered on Mars (Fig. 18).

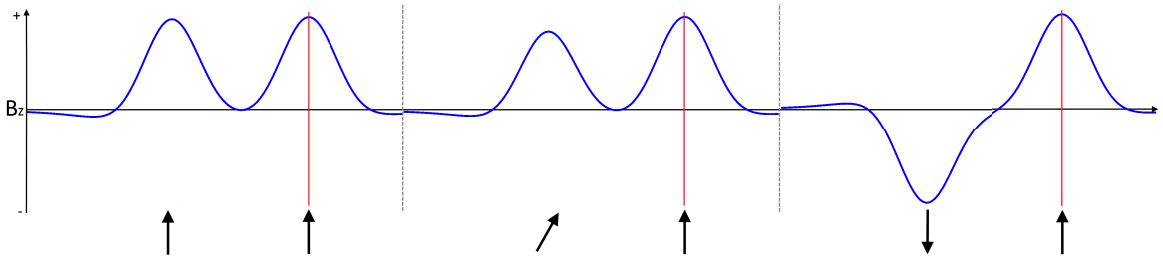

Figure 18: Schematics of the magnetic Down component (B_z) for two anomalies in a distance of 7.5°. From left to right the cases for aligned sources, true polar wander, and opposite orientation are given and indicated by the black arrows. The red vertical line shows the center location of observation.

For the case that both anomalies formed at the same time, or a similar magnetic orientation was present at different times of the dynamo evolution, the orientations of both anomalies are aligned (AL). A 2D-schematic of this case is shown on the left side of Fig. 18, with the blue curvatures showing the B_z-component, the arrows indicating the orientation of the sources and the vertical red line indicating the observed anomaly. For the second case, shown in the middle of Fig. 18, the main magnetic field changed its orientation by 30° prior the formation of the second anomaly, due to e.g. true polar wander and the inclinations of both anomalies therefore vary by 30° (TPW). In the last scenario, which is shown on the right side of Fig. 18, the main magnetic field underwent a polar reversal prior the formation of the second anomaly and both anomalies therefore show opposing magnetic orientation (PR). The results for all scenarios are summarized in Tab. 4 and the calculated areas of admissible paleopole locations for 5° (a) and 7.5° (b) distance and opposing polarity are presented in Fig. 20. As visible in Tab. 4, an anomaly at a distance of 5° strongly alters the measured signal and the model fit (σ_{min}) deteriorates to values of ~ 15 nT, and the confidence limit threshold $\mathbf{I}_{min}$ increases to values of 50 nT. The determined average field values $\mathbf{I}(R)$ for the two different distances and all three cases are shown in Fig. 19. On the left side the three cases for two anomalies at a distance of 5° are shown, with the AL case in red, TPW case in cyan, and the PR case in blue. Additionally, the undisturbed signal is presented in green. On the right side of Fig. 19 a similar graphic is shown for two anomalies at a distance of 7.5°. In comparison to added noise it can be seen in Fig. 19 that an anomaly in the vicinity of the observation is clearly visible in the average field as a second maximum in $\mathbf{I}(R)$. It can be observed that an anomaly at 5° distance raises the average field at a distance of 3° to the center of observation and

decreases the SNR significantly. For a distance of 7.5° $\mathbf{I}(R)$ is similar to the signal of the undisturbed case until 4° is reached and the SNR reaches values of 25/1, or even 30/1. At 4° the SNR therefore indicates the radius to which the observed anomaly is least influenced by the perturbing anomaly and the absolute value of the SNR can be taken as a measure of isolation (compare Sec. 3.3.3).

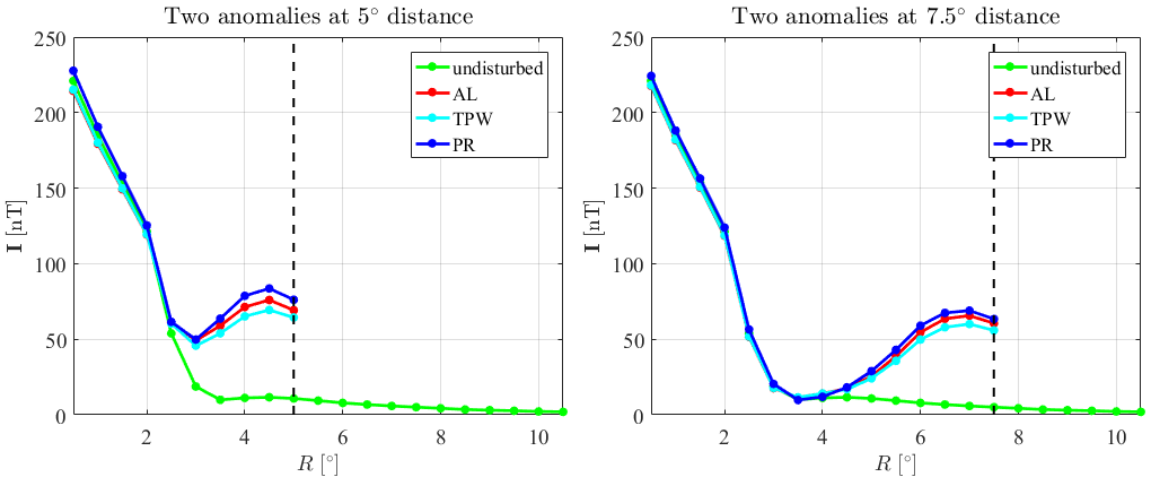

Figure 19: The average field $\mathbf{I}$ as a function of the radius R is shown for an observed anomaly which is perturbed by a second anomaly at 5° (left) and 7.5° (right). Again the green curvature represents the undisturbed signal, while the AL case is shown in red, the TPW case is shown in cyan, and the PR case is shown in blue. The vertical lines indicate the locations of the perturbing anomalies at 5° and 7.5°, respectively.

In consequence of the low SNR and therefore deficient isolation the area of admissible paleopole locations covers over ~ 40% of the planet (Fig. 20), for two anomalies at 5° distance. If the anomalies center locations are separated by 7.5°, corresponding to three times their source radius, admissible paleopole locations can be constrained to ~ 27% of the planets surface. This is due to the, in comparison to 5° distance, five times smaller confidence limit thresholds and corresponding SNRs in combination with a better model fit of $\sigma_{min} \sim 2$ nT.

The obtained results for neighboring anomalies indicate that a separation of at least two times the source radius is necessary to apply the above method and accuracy increases for greater distances. Interestingly, the magnetic orientation of the perturbing anomaly seems to be of secondary importance (compare the AL, TPW, and PR cases in Tab. 4 and Fig. 19). It becomes evident from the Tab. 3 and 4, as well as from Fig. 17 and 20, that an anomaly in close distance to the observation leads to stronger alterations of the determined magnetic orientation than random noise only. In comparison with the investigations of additional random noise it can be further seen that random noise primarily increases the misfit between the observations and the model, while perturbation tends to further increase the confidence limit threshold $\mathbf{I}_{min}$ and therefore the corresponding area of admissible paleopole locations (Fig. 19). This is due to the fact that the inversion algorithm partially fits the perturbing field, but not the randomly distributed noise.

In the above calculations, the magnetic fields Down-component (B_z) was used for the inversions, but investigations of the North- (B_x) and East-component (B_y) obtained similar trends at decreased SNR.

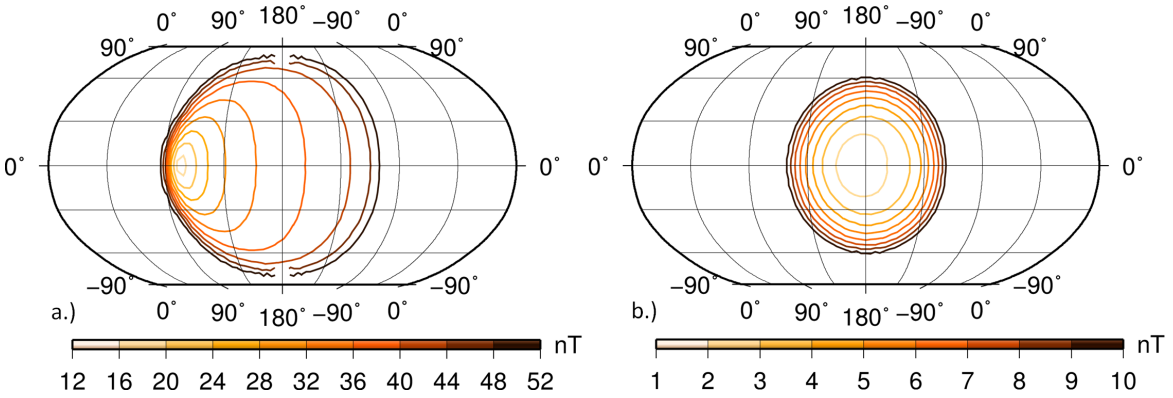

Figure 20: The two Robinson projections show the determined areas of admissible paleopole locations for perturbed anomalies with a second magnetic source of opposing magnetic orientation at 5° (a) and 7.5° (b) distance.

Table 4: Results of synthetic tests considering an anomaly with a size of 2.5° at 0° N / 180° E and $I = 90°$ / $D = 0°$. The distance between primary and perturbing anomaly (Distance) and the magnetic orientation of the perturbing anomaly (Case) are given along with the corresponding minimum misfit (σ_{min}), the maximum field strength (B_{max}), the confidence limit threshold ($\mathbf{I}_{min}$), the inclination and declination (I/D), the SNR, as well as the surface area coverage of admissible paleopole locations (Area).

Distance	Case	σ_{min} [nT]	B_{max} [nT]	$\mathbf{I}_{min}$ [nT]	I/D	SNR	Area
5°	AL	15.6	282.8	49.2	54° / 90°	6/1	42.7%
	TPW	14.6	283.9	45.7	56° / 70°	6/1	42.0%
	PR	14.3	298.6	49.8	21° / 270°	6/1	41.7%
7.5°	AL	2.35	287.5	11.5	87° / 270°	25/1	27.2%
	TPW	2.43	287.9	11.5	86° / 308°	25/1	27.1%
	PR	1.4	294.0	9.7	86° / 272°	30/1	26.3%

4.4 SUMMARY

The tests performed in Sec. 4.1 without perturbation show that using the implemented model a reconstruction of magnetic orientations is possible, independent of the input source. To better reflect natural conditions a Gaussian distribution of the magnetization strength was chosen, with the strongest magnetization in the center of the observed anomaly. This led to decreased residuals for dipole distribution radii which had the same size and at maximum three times the size of the input anomaly. For bigger radii the residuals increased again. Therefore, under optimal conditions, the model is not only capable of determining the magnetic orientation of the input source, but also solve for the lateral extent of the observed source.

After showing that the model is capable of reconstructing a given input orientation, it was of interest how strong signal alterations vary the derived magnetic orientation and STD. From Sec. 4.2 it can be seen that the influence of 5% noise is nearly negligible, but once 10% noise is reached, the magnetic signal is significantly altered and above 10% noise the obtained area of admissible paleopole locations highly increases.

In Sec. 4.3 a second anomaly was placed at a distance of two times the observed anomaly's source radius and the area of admissible paleopole locations was increased to

40% of the planetary surface. It is pointed out that even though the misfit seems rather large, the method is applicable for this constellation and the uncertainty is reflected in the increased area of admissible paleopole locations. For perturbing anomalies it could further be shown that the magnetic orientation of the perturbing anomaly seems to be of no importance to the derived result, especially at greater distances. As shown by the tests, the influence of a perturbing anomaly is rapidly decreased for increasing distances and the stage of isolation can directly be linked to the obtained SNR between the average field in the center of observation and the first minimum in the average field in the surrounding (Sec. 3.3.3). It is hereby stated that a sufficient stage of isolation is reached for a SNR of 10/1, which will be used in the following as boundary condition for paleopole analysis.

In conclusion, all the above investigations help to explain discrepancies from earlier studies with highly different paleopole locations and will in the following help to understand the results obtained for the anomalies investigated in Ch. 5. Furthermore, the above investigations tested the plausibility of possible sources of paleopole variations and showed that the confidence interval with a reasonable boundary condition gives a more robust result as the best fitting location alone. It might be argued that the determined areas of admissible paleopole locations (Fig. 17 and 20) seem rather large and that no significant information can be extracted from the given results. However, in terms of answering the question if Mars underwent a TPW or PR, it is sufficient to constrain admissible paleopole locations to one or the other hemisphere of the planet. The presented method is well capable in determining areas of admissible paleopole locations which cover less than 50% of the planetary surface. In addition, the performed tests show that the uncertainties in the determined paleopole locations were underestimated in previous studies and a single paleopole derived from the best fit gives no robust result.

Part III

RESULTS

In this part it is explained how the anomalies for the paleopole reconstruction and their investigation parameters were selected and the investigation results using the SH-model and the orbital data from MGS and MAVEN are shown.

5

MARTIAN MAGNETIC FIELD ANOMALIES

In the following chapter the previously described method is applied to eight crustal magnetic field anomalies which have been known prior to this thesis, or have been identified using the method described in Sec. 3.3.3. The first three anomalies were detected by Morschhauser et al. (2014) and seemed suitable for paleopole investigations. They are located close to the Green, South, and Tyndall craters and will be denoted as A1, A2, and A3, respectively. The fourth anomaly, linked to the Australe Montes volcano, was already intensively investigated by Plattner and Simons (2015) and it was of interest if the calculated paleopole locations could be confirmed with the method used here. The next two anomalies denoted as P1 and P2 lie close to the Bouguer Crater and within eastern Amazonis Planitia. The mentioned six anomalies were already presented in Thomas et al. (2018) and are discussed in more detail in this chapter. During a global search for new isolated magnetic field anomalies it was possible to identify in total 18 promising magnetic field signals which were investigated in terms of their stage of isolation. Together with the anomalies P1 and P2 16 additional anomalies were found of which # 2 and # 7 will be observed in more detail.
Based on the results obtained in this chapter another method test was performed on the example of anomaly A2, to investigate how varying anomaly parameters, e.g. different center locations alter the results of the paleopole reconstruction.

5.1 SELECTION OF MARTIAN ANOMALIES

The anomaly A1 close to Green Crater

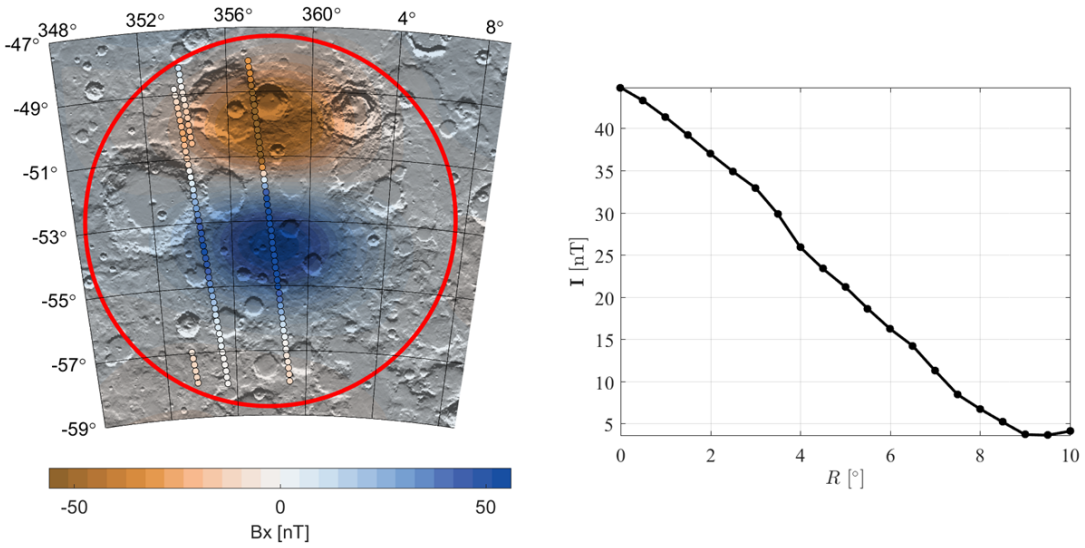

Figure 21: The figure shows two different representations of the magnetic field at the Green Crater anomaly (A1). To the left the magnetic fields B_x-component at 120 km altitude as calculated from the SH-model is shown in combination with the 1 Hz orbital tracks between 90 km and 130 km altitude, on top of a MOLA shaded relief map. Additionally, the derived anomaly radius R_0 is shown as red circle. The right hand side of the figure presents the average field intensity **I** in relation to the distance (R) from the center at 53° S / 358° E.

As mentioned above, the anomaly A1 was identified by Morschhauser et al. (2014) and they located its center at 52° S / 357° E. During the estimation of the confidence limit threshold ($\mathbf{I}_{min}$) it was determined that the center should be relocated to 53° S / 358° E in order to have the highest SNR (Fig. 21 / Tab. 5). As is evident from Fig. 21 the anomaly has a mean center intensity of ~ 50 nT, which steadily decreases to values below 5 nT at $R = 8.5°$. The lowest field values are registered at a radius of $R = 9.5°$ with a remaining field intensity of 3.6 nT. Therefore, the anomaly's radius was defined as $R_0 = 9.5°$ (Fig. 21 / red line). On the left side of Fig. 21 the magnetic fields B_x-component at 120 km altitude as derived from the SH-model is shown on top of a topographic map from the Mars Orbiter Laser Altimeter (MOLA). The figure further shows the available down sampled 1 Hz AB and SPO measurements from MGS in that region at altitudes between $90 - 130$ km. In the respective magnetic field component, the anomaly A1 is presented as a nearly perfect dipole with a stronger maximum magnetic field at ~ 54° S, and a minimum magnetic field at ~ 50° S. The stronger maximum can as well be observed in the along track data which lies in between 353° E and 356° E. Note that at the locations of the tracks maximum and minimum, the SH-model shows a much weaker field.

The anomaly A2 close to South Crater

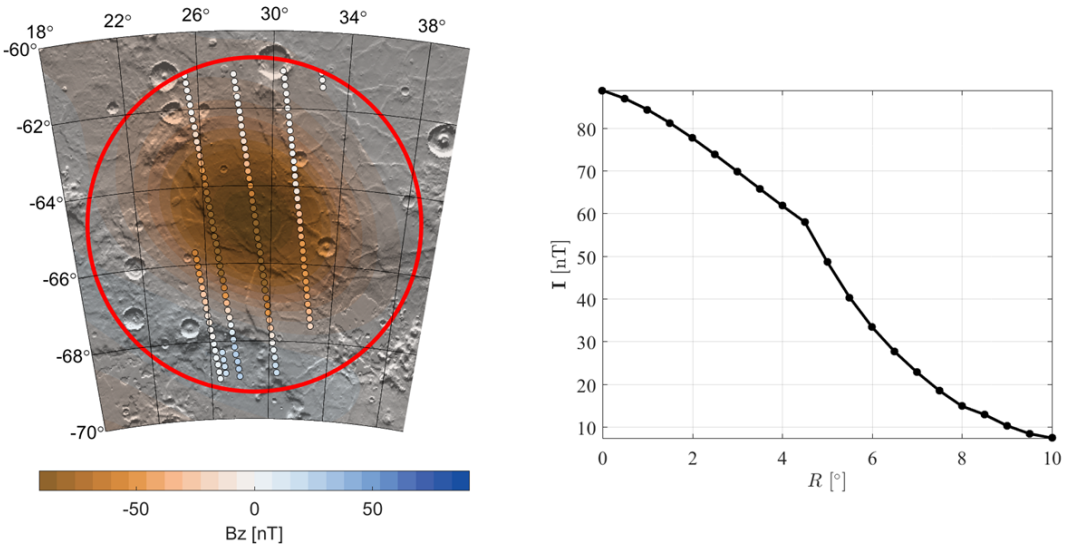

Figure 22: Similar to Fig. 21, but showing the B_z-component of anomaly A2 close to the South Crater with the center located at 64.5° S / 28.5° E.

Similar to the Green Crater anomaly, the anomaly A2 at the South Crater was first identified by Morschhauser et al. (2014) at 64° S / 28° E. Using the method described in Sec. 3.3.3 to estimate the confidence limit threshold it was found that the magnetic signal is reduced to $< 10\%$ of the anomalies center magnetic field (Fig. 22 / right side and B_{max} / Tab. 5), with a center location at 64.5° S / 28.5° E and at a radius of $R = 10°$. At this radius, the highest SNR in this investigation with 13/1 was calculated and therefore it was defined that the anomalys source radius $R_0 = 10°$. At the left side of Fig. 22 the B_z-component of the magnetic field as derived from the SH-model in combination with the AB/SPO orbital tracks down sampled to 1 Hz and between 90 km and 130 km altitude are shown, again with an underlying MOLA shaded relief map. The magnetic Down-component reveals a nearly spherical magnetic anomaly and it was assumed by Morschhauser et al. (2014) that the magnetic orientation must be close to vertical.

Again, the SH-model is in good agreement to the orbital tracks in the center of the anomaly, but residuals increase towards the edges. Here, the SH-model derives a higher magnetic field intensity below 64° S and a lower intensity above 66° S.

The anomaly A3 close to Tyndall Crater

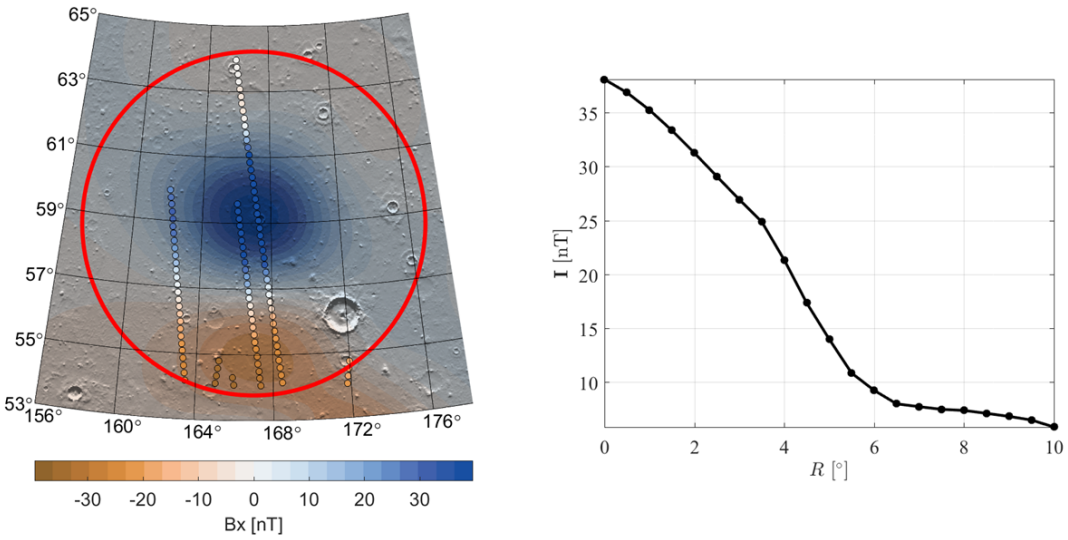

Figure 23: Similar to Fig. 21, but showing anomaly A3 close to the Tyndall Crater with the center located at 58.5° N / 166.5° E.

The last of the anomalies identified by Morschhauser et al. (2014) is the anomaly A3 close to the Tyndall Crater. Its location as identified by Morschhauser et al. (2014) is at 57° N / 167° E and was relocated to 58.5° N / 166.5° E (Tab. 5) were a SNR of 7/1 was determined. In comparison to A1 and A2 the SNR is relatively low, due to the weaker magnetic field, which hardly exceeds 35 nT in the center and the remaining signal of 5.8 nT at 10° distance. The derived confidence limit threshold is therefore ~ 16% of the maximum signal. The main reason for this is an anomaly close by at 49° N / 168° E (Morschhauser et al., 2014), which perturbs the observed signal especially at the southern edge. In comparison to the tests in Sec. 4.4 (Fig. 19) the decreasing gradient is not as inclined and no second maximum is visible. Instead, the mean field decreases steadily up to a distance of 6°. It then converges to ~ 7 nT and further decreases with a low gradient to 5.8 nT at a distance of $R_0 = 10°$. As before, the SH-model fits the AB/SPO-data well in the strong field regions, but in comparison to A1 and A2 good fits are also achieved in regions of low magnetic field intensity.

The Australe Montes anomaly

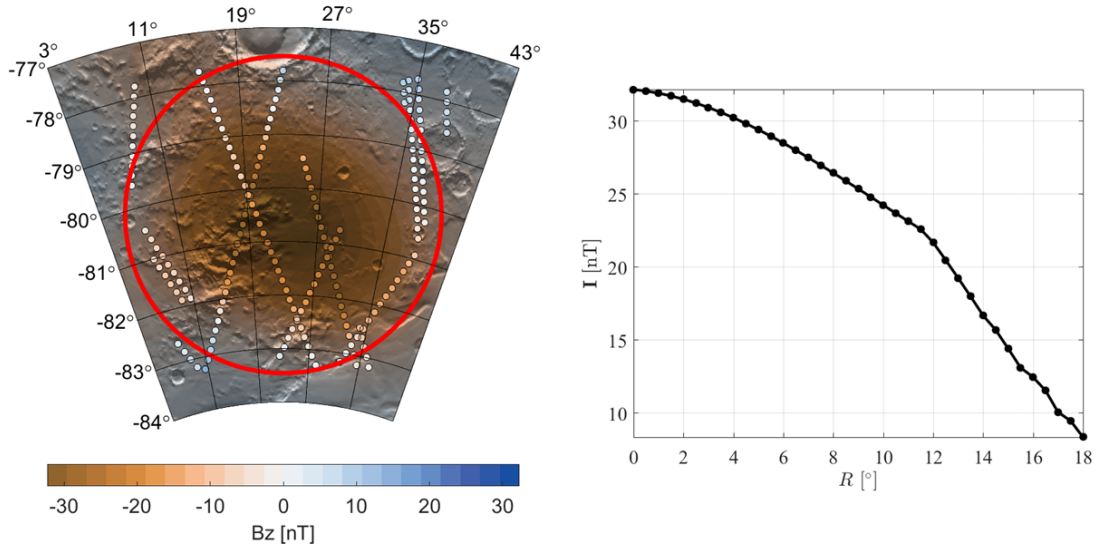

Figure 24: Similar to Fig. 21, but showing the B_z-component of the Australe Montes anomaly at a center location of 80.5° S / 23.4° E and an R_0 increased to 18°.

The forth anomaly in this investigation was already intensively discussed by Plattner and Simons (2015), who used a localized SH-model of degree and order 130 to model the crustal magnetic field of the high southern hemisphere of Mars. One of the features within the modeled magnetic field seemed to be associated with the the Australe Montes volcano at 81° S / 18° E. To model the Australe Montes magnetic field and its magnetic orientation, Plattner and Simons (2015) used a spherical source. Here, it was of interest if the ESD method is capable to verify the results of Plattner and Simons (2015), using the less resolved global SH-model by Morschhauser et al. (2014). During a private communication with Alain Plattner it was revealed that a programming mistake led to a false clustering of paleopole locations (compare Fig. 9 in Plattner and Simons, 2015). Therefore, a robust estimate for a paleopole location associated with the Australe Montes volcano was missing prior to this investigation.

In Fig. 24 a part of the Planum Australe at high southern latitudes of Mars is shown as a shaded topographic map from MOLA-data. The Australe Montes volcano is located at 81° S / 18° E, but the center of the magnetic anomaly as derived from the SH-model by Morschhauser et al. (2014) is located at 80.5° S / 23.4° E. In comparison to the anomalies observed before it was necessary to increase the dipole distribution radius to $R_0 = 18°$ in order to maximize the SNR (Fig. 24 / red circle). However, this only corresponds to 160 km in this high latitudes. In comparison, the radius of 4.5° obtained for anomaly P2 at 35° N has the same extent in kilometers. As in the previous figures, the down sampled orbital tracks from the MGS spacecraft are shown for altitudes between 130 km and 90 km.

Again, the highest residuals between the SH-model and the data are mainly located at the edges, but the orbital track crossing longitude 19° E and 27° E from northwest to southeast results in higher residuals west of 19° E. The generally higher relative residuals are caused by the weak magnetic field observed at the Australe Montes anomaly. The magnetic field's Down-component (B_z) in the center of the anomaly hardly exceeds −30 nT.

This results in a low SNR of only 4/1 (Tab. 5), even though the magnetic field is reduced to ~ 8 nT at $R_0 = 18°$ (Fig. 24 / right). The right side of Fig. 24 is further different to the previous **I**(R) trends, because of a less steep gradient in **I**(R).

The anomaly P1 close to Bouguer Crater

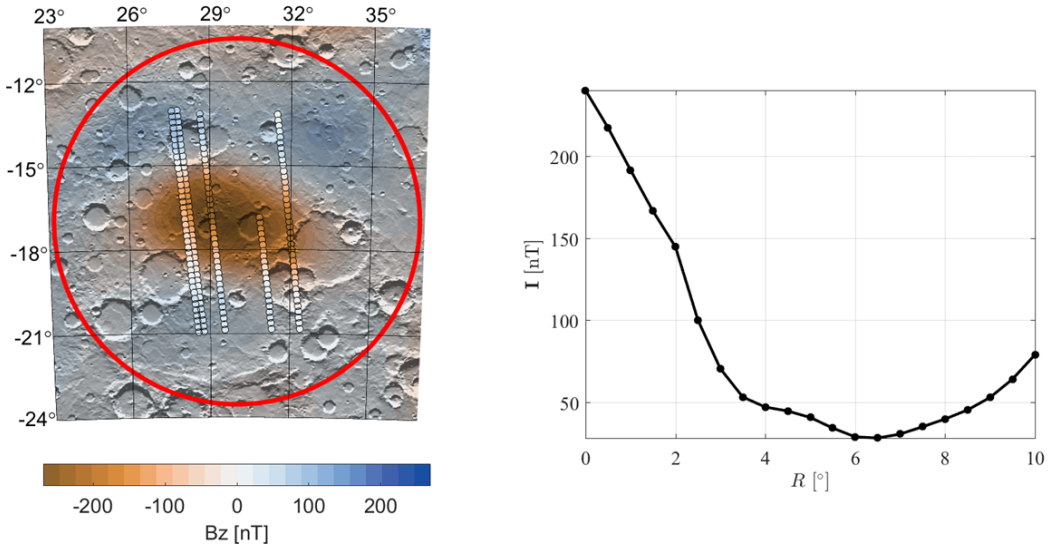

Figure 25: Similar to Fig. 21, but showing the B_z-component of anomaly P1 close to the Bouguer Crater in Terra Sabaea with a center located at 16.5° S / 30° E.

The anomaly denoted as P1 is located at 16.5° S / 30° E in Terra Sabaea, close to the Bouguer Crater (18.7° S / 27.2° E). It is one of the anomalies from our extensive search for more isolated magnetic field anomalies within the Martian crustal magnetic field. In comparison to the other anomalies published in Thomas et al. (2018) it is by far the strongest magnetic anomaly. Its Down-component reaches $B_{max} = 261.4$ nT in the center (Tab. 5 / Fig. 25) at an altitude of 120 km. As visible in Fig. 25 the maximum absolute magnetic field intensity forms an ellipse around the center of the anomaly which is surrounded by a weaker field of around 50 nT. This is probably associated with an inclined magnetic orientation. It was possible to find five representative orbital tracks within the down sampled AB/SPO data set. Fits between the SH-model and the tracks are generally good, with increased residuals in the west. For this region the weak field regions are in the order of the maximum field intensity of previously investigated anomalies and therefore they are clearly visible in the orbital tracks.

The highest SNR was calculated at a distance of 6.5° to the center (Fig. 25) at the edge of the low field region and therefore $R_0 = 6.5°$. For increasing radii, **I**(R) rises, suggesting that other perturbing anomalies are close by. With the high gradient in **I**(R), which is observed for $R < 6.5°$ most of the magnetic field in this region originates from the observed anomaly. Therefore, it is expected that the achieved result is in general well constrained and robust.

The anomaly P2 in eastern Amazonis Planitia

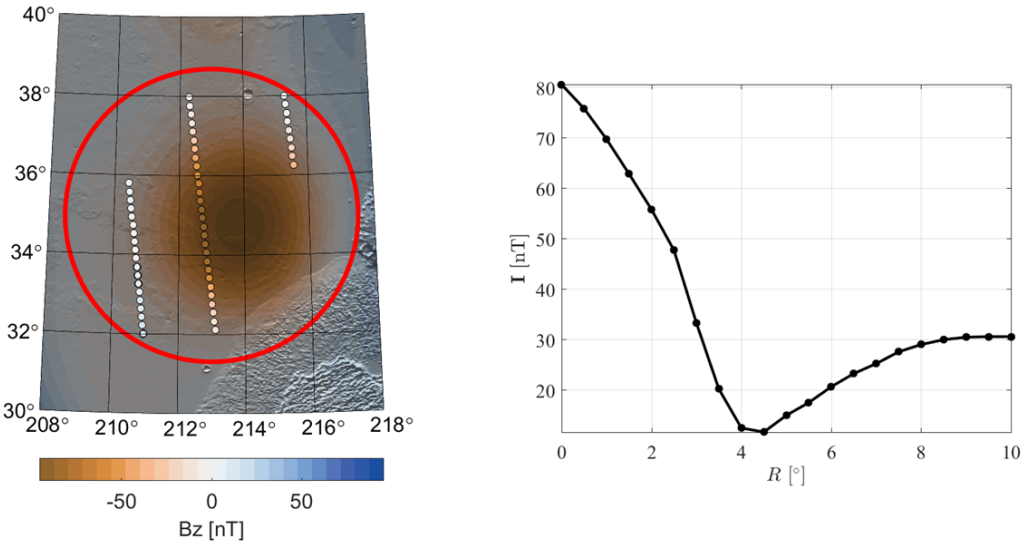

Figure 26: Similar to Fig. 21, but showing the B_z-component of anomaly P2 in eastern Amazonis Planitia with a center located at 35° N / 212.5° E.

In eastern Amazonis Planitia another isolated magnetic field anomaly could be identified and it was denoted P2. It is located at 35° N / 212.5° E in a region which is mostly free of topographic features (Fig. 26 / left). With a magnetic field intensity in the center of 94.5 nT, it is the second strongest anomaly investigated in Thomas et al. (2018), but due to magnetic fields in the vicinity the SNR is only 7/1 (Tab. 5). The left side of Fig. 26 shows a nearly circular magnetic field in the Down-component (B_z) at the altitude of 120 km. The strong magnetic field is clearly visible in the AB/SPO tracks, whereby the track in the center of the image, between 212° E and 214° E is the most representative track for anomaly P2. The assumption that anomalies in the vicinity lead to the low SNR is supported by the observed trend in $\mathbf{I}(R)$ (Fig. 26 / right side). The magnetic signal decreases with a steep gradient up to a distance of 4°, reaches its minimum at 4.5° and then increases again and converges to 30 nT, which corresponds to one third of the central magnetic field strength, respectively. At the minimum the lowest SNR is obtained with $\mathbf{I}_{min} = 11.7$ nT and 4.5° is chosen as the dipole distribution radius R_0 for the inversion. It should be pointed out that the anomaly's center is off-center to the red circle. This implicates that the field strength of P2 is not sufficient to dominate the magnetic measurements in this region. A second anomaly to the east perturbs the measured signal and in order to achieve the highest SNR the center of observation was shifted westward. For this reason the maximum value in $\mathbf{I}(R)$ only reaches 80 nT (Fig. 26), because this value belongs to the center of observation and not to the center of the magnetic field anomaly.

Summary

Table 5 summarizes the magnetic investigations to derive the center locations of the observations (CL) and the estimated source radii (R_0) according to the confidence limit thresholds ($\mathbf{I}_{min}$) and the highest SNR. The table further includes the preferred component for each inversion ($B_{x,y,z}$) as defined by the SNRs and the maximum magnetic field intensity in the center of the anomalies (B_{max}). As already pointed out in Sec. 3.2 the magnetic Down-component usually holds the strongest magnetic signal and it is therefore the preferred component for the inversion. This is confirmed in four out of six cases where the B_z-component led to the highest SNR. For the remaining anomalies the B_x-component was more suitable. From the previous paragraphs and Tab. 5 it is concluded that all but one of the observed anomalies present itself with a sufficient stage of isolation as derived in Sec. 4.4. The most robust inversion results will be achieved for the anomalies A1, A2 and P1 with SNRs of at least 10/1. The calculated confidence limit thresholds for these anomalies ($\mathbf{I}_{min}$) do not exceed 11% of the maximum field strength (B_{max}) and should therefore give well constrained areas of admissible paleopole locations. The anomalies A3 and P2 are not as well constrained, even though A3 has the second lowest confidence limit threshold, but the SNR only reaches 7/1, which is due to the weak maximum field strength of $B_{max} = 39.1$ nT.

It has to be pointed out, that under the restrictive conditions set in Sec. 3.3.3 and 4 the anomalies A3 and P2 are not perfect candidates for paleopole investigations, but in comparison to the Australe Montes anomaly they are still acceptable. The weak magnetic field at the location of Australe Montes and the low gradient in $\mathbf{I}(R)$ (Fig. 24 / right side), which is slightly elevated, leads to a SNR of only 4/1. It is therefore possible that the observed magnetic field in the vicinity of the Australe Montes volcano originates from a number of sources and not necessarily from a single source. However, a single source of magnetization which is influenced by other magnetic features in the neighboring regions could as well be a possible scenario. Either way, the original magnetic signal is most certainly altered and the low SNR should lead to a wide area of admissible paleopole locations which represents the uncertainty given by the weak magnetic field.

Table 5: Summary of the anomaly observations to determine the most suitable center locations and dipole distribution radii. Given are the anomaly name (Anomaly), determined center location (CL), magnetic field component used in the inversion ($B_{x,y,z}$), dipole distribution radius (R_0), maximum field strength (B_{max}), calculated confidence limit threshold ($\mathbf{I}_{min}$), and the signal to noise ratio (SNR).

Anomaly	CL	$B_{x,y,z}$	R_0	B_{max} [nT]	$\mathbf{I}_{min}$ [nT]	SNR
A1	53°S / 358°E	B_x	9.5°	56.0	3.6	12/1
A2	64.5°S / 28.5°E	B_z	10°	90.4	6.9	13/1
A3	58.5°N / 166.5°E	B_x	10°	39.1	5.8	7/1
A. Montes	80.5°S / 23.4 °E	B_z	18°	32.2	8.4	4/1
P1	16.5°S / 30°E	B_z	6.5°	261.4	26.9	10/1
P2	35°N / 212.5°E	B_z	4.5°	94.5	11.7	7/1

5.2 PALEOPOLE INVESTIGATION FROM THE SH-MODEL

With the method presented in Sec. 3.2 the six crustal magnetic field anomalies presented in the previous section were used to determine best fitting paleopole locations and their corresponding areas of admissible paleopole locations. All obtained inversion results are shown in Fig. 27 within a spherical North Pole (a), a spherical South Pole (b) and a Robinson projection of the Martian topography, derived from MOLA data. The marker for the best fitting paleopole locations are chosen to indicate if the corresponding contour line bounds admissible paleopole locations in the northern hemisphere (upward pointing triangle), southern hemisphere (downward pointing triangle), or at mid latitudes (circle). The confidence intervals of each anomaly (compare e.g. Fig. 17) are reduced to the corresponding confidence limits threshold ($\mathbf{I}_{min}$ at Tab. 5 / 6) and all solutions inside the contour line are assumed admissible. Tab. 6 summarizes the determined STDs (σ_{min}), confidence limit thresholds ($\mathbf{I}_{min}$), inclinations and declinations (I/D) together with the paleopole location (PL) of the best fit, as well as the surface coverage of the area of admissible paleopole locations (Area).

Table 6: Results for the inversion of six crustal magnetic field anomalies. Anomaly name (Anomaly), the calculated STD (σ_{min}), the confidence limit threshold ($\mathbf{I}_{min}$) determined inclination and declination (I/D), and corresponding paleopole location (PL) of the best fitting model, as well as the surface area coverage of admissible paleopole locations (Area) are given.

Anomaly	σ_{min} [nT]	$\mathbf{I}_{min}$ [nT]	I/D	PL	Area
A1	3.1	3.6	52° / 188°	68°S / 197°E	9%
A2	1.1	6.9	−78° / 8°	86°N / 159°E	40%
A3	1.8	5.8	−44° / 196°	55°S / 140°E	46%
A. Montes	0.4	8.4	−85° / 26°	87°N / 120°E	57%
P1	23.7	26.9	−61° / 172°	31°S / 203°E	17%
P2	3.6	11.7	−45° / 268°	16°S / 101°E	40%

For A1 a minimum misfit of $\sigma_{min} = 3.1$ nT was calculated, resulting in admissible paleopole locations in the high southern hemisphere (Fig. 27) with a total surface coverage of 9% (white line).

In comparison, the determined STD for anomaly A2 is around three times smaller (Tab. 6), but due to the relatively strong average magnetic field in the vicinity of observation the confidence limit threshold is $\mathbf{I}_{min} = 6.9$ nT and admissible paleopole locations therefore cover an area of 40% in the northern hemisphere of Mars (yellow line). The contour line partly follows the Martian crustal dichotomy boundary and indicates a former magnetic South Pole in that region.

A similar result is obtained for anomaly A3. While the standard deviation is small ($\sigma_{min} = 1.8$ nT), the determined confidence limit threshold is more than three times higher ($\mathbf{I}_{min} = 5.8$ nT), leading to an area of admissible paleopole locations covering 46% of the planet and thereby nearly the whole southern hemisphere (green line). The anomaly A3 therefore indicates a former magnetic South Pole in the southern hemisphere of Mars.

For P2 the former magnetic South Pole location can not be constrained to one or the other hemisphere, because due to the confidence limit threshold of $\mathbf{I}_{min} = 11.7$ nT admissible paleopoles can be located within a 40% big area on the Martian surface, reaching from the South Pole to mid northern latitudes (light green line).

The low SNR found for the Australe Montes anomaly leads to the biggest area of admissible paleopole locations with a total surface coverage of 57% (orange line). Still,

the determined confidence limit threshold constrains paleopole locations to the northern hemisphere, including a large fraction of the Tharsis province. This result is compatible with the obtained paleopole locations by Plattner and Simons (2015), but obtains a wider uncertainty. The calculated STD $\sigma_{min} = 0.4$ nT is comparatively small, indicating that the ESD-model is able to fit the SH-model nearly perfectly.

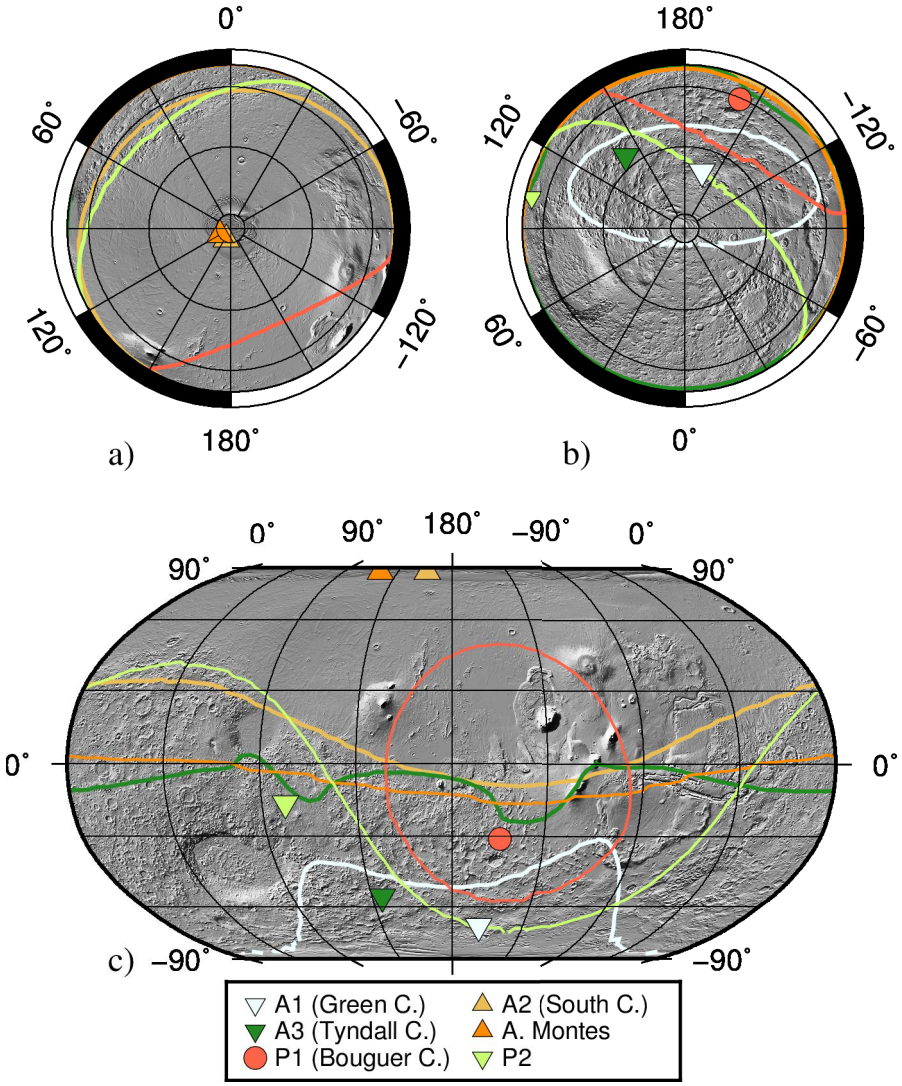

Figure 27: Admissible paleopole locations for the six crustal magnetic field anomalies (Thomas et al., 2018) investigated with the SH-model. Shown are the best fitting locations (compare Tab. 6) indicating whether paleopole locations are located in the northern hemisphere (upward pointing triangles), the southern hemisphere (downward pointing triangles), or are located at mid latitudes excluding the geographic poles (circle). The colored lines bound the areas of admissible paleopole locations as constrained by the confidence limit threshold (Tab. 5 / 6). Part a of the figure shows a spherical North Pole projection of the Martian surface, while b shows a spherical South Pole projection and c shows a global Robinson projection.

Anomaly P1 (red line) is an exception with respect to the position of the area of admissible paleopole locations, as this area excludes the geographic poles of Mars. With a surface coverage of only 17%, including parts of the Tharsis region, Terra Sirenum, Terra Cimmeria, Amazonis Planitia as well as Elysium Planitia. Therefore, a former Martian magnetic pole must have been located in this region spanning from ~ 60° S to ~ 50° N and being separated from the geographic poles by at least 30°. The absolute misfit for anomaly P1 reaches $\sigma_{min} = 23.7$ nT, which corresponds to a relative misfit of ~ 9.0%, due to the

high intensity of the magnetic field with $B_{max} = 261.4$ nT. In comparison, the relative misfits are 5.5% for A1, 1.2% for A2, 4.6% for A3, 1.2% for Australe Montes and 3.8% for anomaly P2, respectively.

In summary, two of the observed anomalies (A1 and A3) indicate a former magnetic South Pole in the southern hemisphere, while two (A2 and Australe Montes) indicate a former magnetic South Pole in the northern hemisphere. This is clear evidence that at least once during the evolution of the Martian dynamo the main orientation performed a full PR. Furthermore, during another stage of the dynamos evolution a TPW appeared, which is indicated by the area of admissible paleopole locations determined from anomaly P2.

5.3 DETERMINED DIPOLE DISTRIBUTIONS FROM THE SH-MODEL

In addition to the calculated areas of admissible paleopole locations, a closer look can be taken at the determined magnetization of the best fitting models (Fig. 28). In Fig. 28, the magnetization strengths M_i of the individual model dipoles for each investigation are plotted on shaded topographic maps, derived from MOLA data, together with the dipole distribution radii R_0 as red circles (compare Tab. 5). Magnetization strengths for all anomalies are in the order of 10^{13} $\frac{A}{m}$ due to ESD assumptions (Sec. 3.1) and hereby particulary the missing volume contribution.

As pointed out in Ch. 3 and 4 the standard model in this investigation uses a distribution of 241 dipoles at surface altitude. The maximum number of dipoles with non-zero magnetization is usually smaller than the number of observation points N (Parker, 1991; Thomas et al., 2018). Taking a detailed look at Fig. 28 it can be seen that this is true and only between 31 and 65 dipoles are different from zero. It further can be seen that the dipoles with non-zero magnetization cluster around the center of observation for anomalies A1, A2, and P1 with decreasing magnetization as a function of center distance. It seems that a centralized localization of dipoles correlates with high SNRs. In this case, the assumption of uniform magnetization can fit the data well.

In comparison, the dipole distribution for anomaly A3 shows a more complex structure. Most of the dipoles are distributed along the northwest-southeast axis, but the strongest magnetization can be found off-center in a band shape crossing along the north-south axis. The off-center localization of the strongest dipoles is another indicator for field contributions from outside the observed anomaly, which was as well quantified by the SNR given in Tab. 5. However, magnetization strength decreases with increasing center distance and the uncertainty given by the area of admissible paleopole locations, which covers 46% of the Martian surface, is not unrealistically small to assume the result shown in Fig. 27 to be underestimated.

For anomaly P2 the distribution of paleopole locations is much more circular, with the strongest magnetization in the center, but the center is shifted towards the eastward direction, to the visual center as observed in Fig. 26. This supports the assumption from Sec. 5.1 that the center of observation is offset to the center of the anomaly. It was assumed from the observed $\mathbf{I}(R)$ (Fig. 26) that a second anomaly in the vicinity of anomaly P2 must be present, which alters the magnetic signal and increases the mean field intensity to the east. This assumption seems plausible taken the two dipoles with $M > 20 \cdot 10^{13}$ $\frac{A}{m}$ east of the 216° meridian into account.

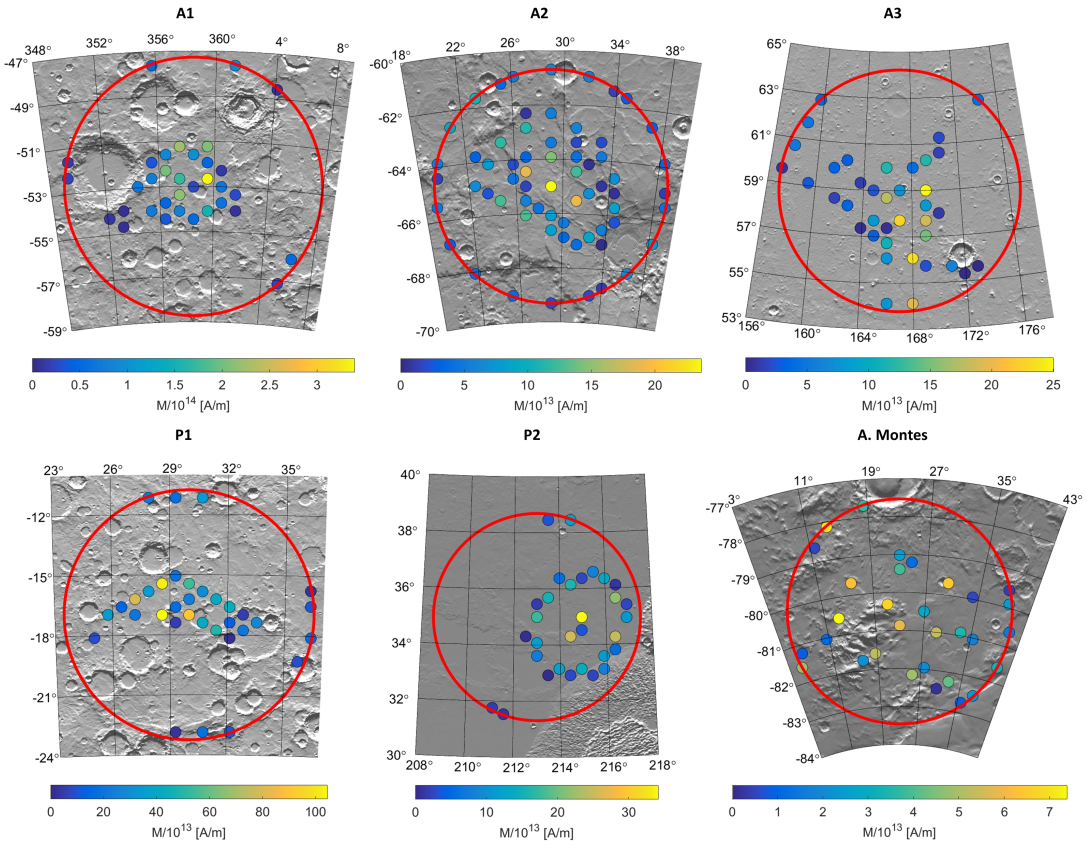

Figure 28: Resulting magnetization distribution for the best fitting models of anomalies A1, A2, A3, P1, P2, and Australe Montes are shown as the dipoles' magnetization strengths $M_i > 0 \frac{A}{m}$, plotted on a MOLA shaded relief topographic map (Thomas et al., 2018). The red circles indicate the respective dipole distribution radii R_0 as summarized in Tab. 5. Note, that every anomaly has its individual color scale for their respective dipole strengths.

As pointed out earlier, the Australe Montes anomaly might be the least suited anomaly for this investigation, due to the weak and spatially extended magnetic field. In Fig. 28 it can be seen that in fact non-zero magnetization spreads over the entire observation area. Still, the strongest magnetization is present in the direct vicinity of the Australe Montes volcano. It is therefore a realistic scenario that most of the signal detected at the location of Australe Montes originates from the magnetic source associated with the Australe Montes volcano.

5.4 PALEOPOLE INVESTIGATIONS FROM ORBITAL TRACKS

5.4.1 *Synthetic track investigation*

To evaluate whether or not the model is capable to determine a paleopole location from orbital track data, it is investigated if synthetic tracks with the components of the magnetic field calculated from the SH-model by Morschhauser et al. (2014) allow for a reconstrution of the results obtained in Sec. 5.2. For this purpose anomaly A1 is chosen, due to the well constrained area of admissible paleopole locations, and two track dispositions are generated. In the first test a single track crosses the center and 42 observation points are distributed $\pm 5°$ from the center of the anomaly. For the other analysis two tracks are separated by 4° in longitude and cross the anomaly $\pm 5°$ in latitude. Again 42 observation points are distributed. Both tracks are inclined with a minimum altitude of 110 km at $+5°$ and a maximum altitude of 135 km at $-5°$ from the center.

Due to the altitude variations in the tracks it is not possible to estimate a confidence limit threshold as described in Sec. 3.3.3 and another method to constrain the number of allowed models needs to be defined. Considering the results of the SH-model investigation and comparing the determined STDs (σ_{min} / Tab. 6) with the calculated confidence limit threshold ($\mathbf{I}_{min}$ / Tab. 5) the confidence limit threshold is set to $\mathbf{I}_{min} = 3 \cdot \sigma_{min}$ for the inversion with track data.

Table 7: Results for the inversion of two track dispositions and varying dipole distribution radii R_0. Given are the amount of distributed tracks (Number of tracks), the calculated STD (σ_{min}), with corresponding confidence limit threshold $\mathbf{I}_{min}$, the determined inclination and declination (I/D), as well as the corresponding paleopole location (PL).

Number of tracks	R_0	σ_{min} [nT]	$\mathbf{I}_{min}$ [nT]	I/D	PL
1	4°	0.8	2.4	4° / 268°	3° S / 268° E
2	4°	1.4	4.2	50° / 186°	67° S / 191° E
1	9.5°	0.4	1.2	−12° / 92°	4° N / 93° E
2	9.5°	2.0	6.0	51° / 172°	68° S / 160° E

For both track dispositions dipole distribution radii of $R_0 = 4°$ and $R_0 = 9.5°$ are chosen and the obtained results are listed in Tab. 7. It can be seen that the determined STDs for single track inversions are smaller than for the two track inversions and therefore result in smaller confidence limit thresholds. However, the determined paleopole locations of the single track inversions vary by 108° in longitude, meanwhile two track inversions show a longitude difference of only 31°. If these best fitting paleopole locations are further compared to the results obtained in Sec. 5.2 (Tab. 6) it can be seen that the single track inversions are not correlated to the best fitting location of A1 (68° S / 197° E), whereas the two track inversions have a maximum variation of 1° in latitude and 37° in longitude.

If furthermore the areas of admissible paleopole locations are investigated in more detail (Fig. 29) a resemblance between the areas of the two tracks (yellow and bright green) and the area shown in Fig. 27 (white line) can be seen. In comparison, similarity fades for the area obtained from the single track inversion with $R_0 = 4°$, but is still present, while for $R_0 = 9.5°$ the area is separated in two areas at mid-latitudes and has no resemblance to the shapes of the other areas.

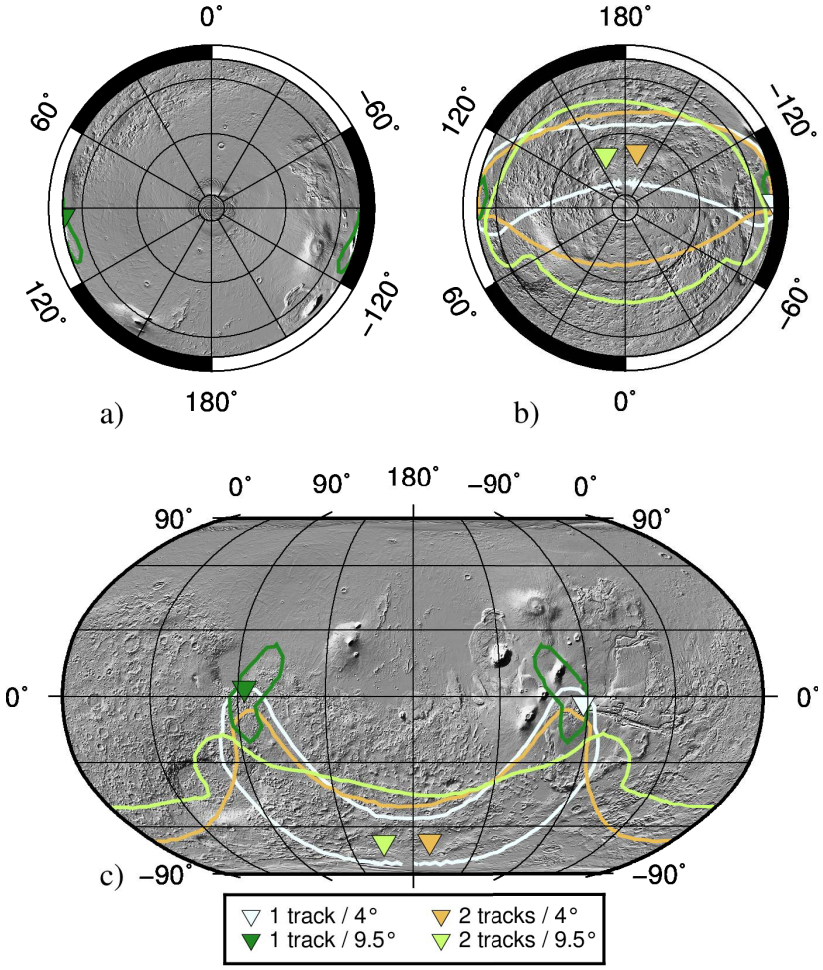

Figure 29: Admissible paleopole locations for two track dispositions with dipole distribution radii of 4° and 9.5°. Shown are the best fitting locations (compare Tab. 7) with colored, inverted triangles and lines of same color bound the corresponding areas of admissible paleopole locations as constrained by the confidence limit threshold (Tab. 7). Part a of the figure shows a spherical North Pole projection of the Martian surface, while b shows a spherical South Pole projection and c shows a global Robinson projection.

As earlier explained it was observed for the anomalies A1, A2, and P1 that the magnetization should decrease as a function of center distance to obtain robust results. Fig. 30 shows the magnetization strength distributions for the track inversions. On the right hand side the resulting distributions for the two track inversions are presented and it can be seen that the strongest magnetization is located at the center of observation and magnetization is decreased at off-center locations for both dipole distribution radii. This is not the case for the single track inversions which are presented on the left hand side of Fig. 30. Here the strongest magnetization ($M = 122.6 \cdot 10^{14} \frac{A}{m}$) for $R_0 = 4°$ can be found at 52° S / 0.3° E, with a slightly smaller magnetization ($M = 116.7 \cdot 10^{14} \frac{A}{m}$) at 52° S / 356.3° E. In comparison, the center magnetization is $M = 94.8 \cdot 10^{14} \frac{A}{m}$. Due to the fact that the maximum magnetization is located at a distance of ~ 2° to the center location, which is already half the dipole distribution radius, this inversion obtains no robust result, because the assumption of uniform magnetization is violated. Even wider is the dislocation of the maximum magnetization for the case with $R_0 = 9.5°$, with the strongest magnetization being located at 52.7° S / 6.2° E. Note that there is a second strong magnetization at the opposite side of the dipole distribution with half the strength of the maximum magnetization. The violation of uniform magnetization becomes more obvious for this inversion and is presented as separated areas of admissible paleopole locations in Fig. 29 (green lines).

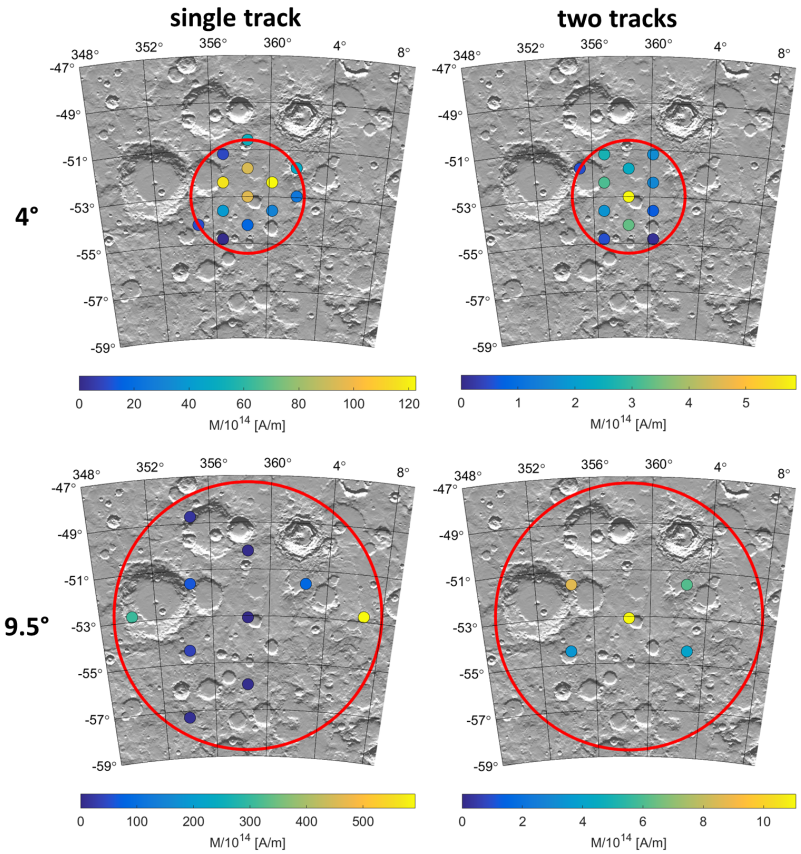

Figure 30: Dipoles' magnetization strengths $M_i > 0$ from track investigations of anomaly A1, plotted over a MOLA shaded relief topographic map. The red circles indicate the respective dipole distribution radii R_0 with 4° (top) or 9.5° (bottom), with maps on the left showing the magnetization maps for a single track analysis and maps on the right hand side of the figure showing the magnetization strengths for inversions with two synthetic tracks above the anomaly.

For the shown investigations it is concluded that an inversion using tracks is possible if at least two lateral separated tracks are present. The synthetic tests revealed high correlation with the results obtained from an equal distanced distribution of observation points, e.g. when using the SH-model. In principle this allows to perform paleopole investigations soon after measurement, without the necessity to generate global, or local models of the magnetic field first. However, in this specific investigation the synthetic tracks rely on the same model as the equal distanced observation points and it is therefore not surprising that results show correlation. Unprocessed, or only slightly corrected real data could have higher residuals to the model, or the real magnetic field and track analysis should be performed cautiously.

5.4.2 *Paleopole investigation from MGS data*

As explained earlier, the SH-model by Morschhauser et al. (2014) is based on the measurements by MGS. It was therefore of interest to test how along track data and the SH-model vary in their determined paleopole reconstructions. However, the comparison of the inversion results using the SH-model (Sec. 5.2) and the results of track data lacks a quantitative measure, due to the differences in the determination of the confidence limit threshold (see Sec. 5.4.1). As explained in Sec. 3.3.3, the confidence limit threshold $\mathbf{I}_{min}$ is determined through the analysis of the magnetic field in the vicinity of the observations center at constant altitude. As explained in Sec. 5.4.1 the inclination of the orbital tracks make it

impossible to determine a confidence limit threshold in this way, so that an estimation is necessary. Taken the results obtained from the SH-model inversions (Tab. 5) the confidence limit threshold was chosen to be three times the derived standard deviation of the best fitting model ($\mathbf{I}_{min} = 3 \cdot \sigma_{min}$). This leaves only a qualitative comparison between the model results and the results obtained from orbital data tracks.

Table 8: Results for the inversions of the six crustal magnetic field anomalies using the MGS orbital tracks. Anomaly name (Anomaly), the calculated STD (σ_{min}), corresponding confidence limit threshold $\mathbf{I}_{min}$, determined inclination and declination (I/D), and corresponding paleopole location (PL), as well as the surface area coverage of admissible paleopole locations (Area) are given.

Anomaly	σ_{min} [nT]	$\mathbf{I}_{min}$ [nT]	I/D	PL	Area
A1	0.2	0.6	40° / 258°	25°S / 271°E	10%
A2	2.6	7.8	−64° / 50°	57°N / 108°E	48%
A3	3.0	9.0	−24° / 94°	13°S / 261°E	43%
A. Montes	2.8	8.4	−81° / 290°	73°N / 282°E	58%
P1	4.3	13.0	−23° / 88°	5°N / 123°E	9%
P2	0.4	1.2	−41° / 90°	13°S / 322°E	25%

The Fig. 21 to 22 in Sec. 5.1 show the available orbital tracks from MGS below the altitude of 130 km for the six crustal magnetic field anomalies A1, A2, A3, Australe Montes, P1, and P2. In the shown regions and below the set altitude only a diminished number of observation points was available. As explained in Sec. 3.2 the number of distributed dipoles is at maximum equal to the number of observation points. Due to the hexagonal equal distanced distribution the number of dipoles are constrained to be either 7, 19, 61, or 241. This series could be continued, but for more than 241 dipoles accuracy is not increased and this value was chosen for the inversions using the SH-model. The orbital tracks left for investigation have in total less than 241 observation points. Therefore, the number of distributed dipoles are at maximum 61, depending on the available data points. For this reason, smaller dipole distribution radii R_0 as listed in Tab. 6 were chosen, otherwise the spacing between the distributed dipoles would have been too large. Note, that large distances between the distributed dipoles can result in models which only rely on a single dipole, while the other dipoles are negligibly small or have a value of zero. In such a model the magnetic orientation is mainly determined from the magnetic field in the direct vicinity of the major dipole which can be different from the mean magnetization of the whole source body.

In Tab. 8 the results for the orbital track inversions are listed, with the anomalies names (Anomaly), the calculated STDs (σ_{min}), the corresponding confidence limit thresholds ($\mathbf{I}_{min}$), the determined inclinations and declinations (I/D) in combination with the calculated best fitting paleopole locations (PL), and the areal coverages of the determined admissible paleopole locations constrained by $\mathbf{I}_{min}$ (Area). The best fitting locations and areas of admissible paleopole locations are further shown in Fig. 31.

In a direct comparison of Tab. 8 and 6, the differences between the results obtained from the SH-model and the MGS data become obvious. There are high variances in either the determined inclination or declination and therefore in the calculated best fitting paleopole locations. The most correlated result is obtained for the Australe Montes anomaly

with only a difference of 4° in inclination. The strong deviation in declination is neglected, due to the high inclination of $I = -80°$.

For three of the six anomalies (A2, A3, and Australe Montes) the determined STD is increased. For the other three (A1, P1, and P2) the ESD model and data fit well with STDs as low as 0.2 nT, leading to comparatively small areas of admissible paleopole locations. The smallest area is determined for P1 with a surface coverage of only 9% (Fig. 31 / red line). Only slightly larger is the area determined for A1 with 10% (Fig. 31 / white line), which is only an increase of 1% when compared to the result using the SH-model. The third smallest area is determined for the two areas of anomaly P2 which cover around 25% (Fig. 31 / light green line) of the surface. For the remaining three anomalies the areas of admissible paleopole locations are in the range of earlier results, with slightly increased areas for A2 (Fig. 31 / yellow line) and Australe Montes (Fig. 31 / orange line) and a reduced area for anomaly A3 (Fig. 31 / dark green line).

Again the best fitting paleopole locations are plotted in Fig. 31 with triangles indicating whether the majority of admissible paleopole locations are located on the northern (upward pointing triangle) or southern hemisphere (downward pointing triangle). For anomaly P1, a circle was again chosen to indicate that all these locations are at mid-latitudes, widely excluding the geographic poles.

As already mentioned, the best fitting paleopole locations obtained from track data do not fit the results obtained from the SH-model. On the contrary, Fig. 27 and 31 show that deviations in the determined areas of admissible paleopole locations are present in terms of size and shape, but the overall distributions of paleopoles persist and are comparable to earlier results. Again, anomalies A1 and A3 indicate former Martian paleopole locations in the southern hemisphere, while anomalies A2 and Australe Montes indicate former paleopole locations in the northern hemisphere and anomaly P1 shows paleopole locations which are constrained to mid-latitudes. As for anomaly P2 the result is again uncertain, because admissible paleopole locations are not constrained to one area, but split into two separated areas, one which is mainly constrained to the southern hemisphere and one indicating paleopole locations at mid-latitudes mostly in the same region as P1. This is due to the fact that model fits of similar STD are determined for several magnetic orientations and corresponding paleopole locations. Therefore, rather than generating one combined area with increasing STDs towards the edges, two areas are obtained including equally admissible paleopole locations.

The qualitative comparison between data inversion and SH-inversion leads to the conclusion that orbital track data can be used directly to determine areas of admissible paleopole locations. However, parameter selection beforehand and interpretation of results might be influenced by the chosen tracks, their distribution and especially their data quality. Furthermore, while data selection and processing takes place and the number of available observation points is reduced, the number of distributable dipoles is decreased which influences the distribution radius (R_0) and the model fit.

In addition, the confidence limit threshold is only an empirical estimate, based on six investigations of crustal magnetic field anomalies on Mars, using estimated confidence limit thresholds (Sec. 3.3.3) as reference. Furthermore, the determined best fits can be biased and the confidence limits thresholds as shown in Tab. 8 and Fig. 31 could therefore be too optimistic, leading to underestimated sizes of the areas of admissible paleopole locations. A robust paleopole investigation is therefore best performed with processed data, optimally of constant altitude, or as shown in Sec. 5.2 with a model of the measured magnetization. However, as explained above, deviations in the best fitting paleopole locations exist and are expected, but the regional constraints on the areas of admissible paleopole

locations are similar. This shows again that the determined areas of admissible paleopole locations give the most robust results and it gives further explanation for the origin of the wide spread of paleopole locations found in earlier studies.

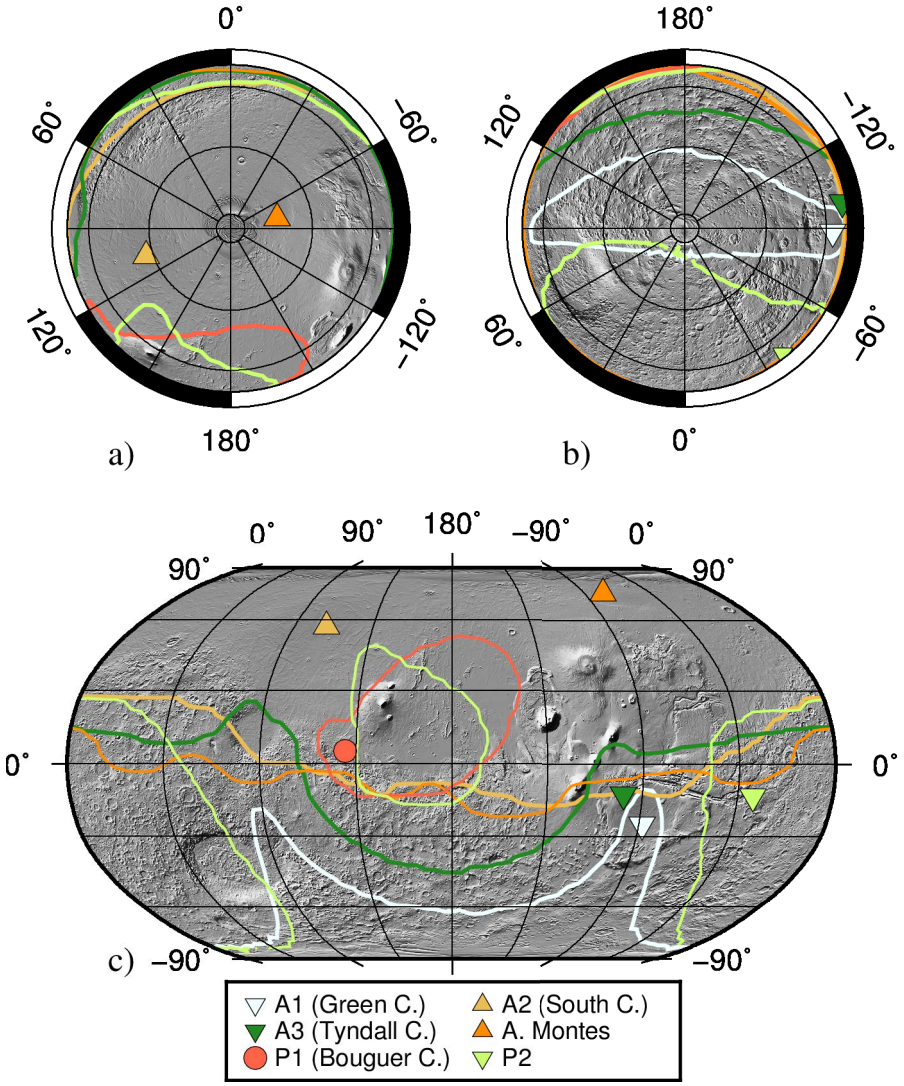

Figure 31: Admissible paleopole locations for the six crustal magnetic field anomalies presented in Sec. 5.1 plotted on a MOLA shaded relief map in spherical projection of the North (a) and South Pole (b) and Robinson projection (c). The shown contour lines enclose the admissible paleopole locations as determined from the inversion of the magnetic field as measured by the MGS spacecraft. Similiar to the prior investigation using the SH-model anomalies A2 and A. Montes indicate admissible paleopole locations in the northern hemisphere (upward pointing triangles), whilst A1 and A3 indicate admissible paleopole location in the southern hemisphere (downward pointing triangles) and anomaly P1 encloses admissible paleopole locations at mid-latitudes (circle). For anomaly P2 two separated areas of admissible paleopole locations are presented. The downward pointing triangle was chosen for this anomaly, because major parts of the area of admissible paleopole locations lie in areas south of 30° N.

5.4.3 *Data selection from MAVEN*

As mentioned in Sec. 2.2.1, the high ellipticity of the orbit of the MAVEN spacecraft made it possible to measure low altitude data. Therefore, the MAVEN data set now shows a much better spatial resolution for altitudes below ~ 400 km than MGS (Mittelholz and Johnson, 2017). In the observations of the MGS data tracks it was possible to detect representative tracks at altitudes below 130 km for the anomalies A1, A2, A3, Australe Montes, P1, as well as P2. Due to the better resolution five anomalies are in the following observed using MAVEN data and the upper limit for the orbital tracks was set to an altitude of 180 km to achieve a higher data density. As evident from Fig. 9, there is no MAVEN data available at latitudes above $\pm 70°$. MAVEN has not yet measured the magnetic field of Planum Australe and no comparative investigation can be performed in this thesis for the Australe Montes anomaly.

Available data was first sorted by distance to the chosen center location with a defined search distance. Then all tracks above the chosen upper limit of the track altitude were deleted from processing. In a last step the time stamps of the tracks were selected and sorted to distinguish between different orbits. In the following Fig. 32 to 36, the selected MAVEN data tracks are shown and at least one of the tracks is presented in detail by comparing the measured MAVEN data with the magnetic field derived from the SH-model at the same locations (latitude, longitude and altitude) of the MAVEN data.

The anomaly A1 close to Green Crater

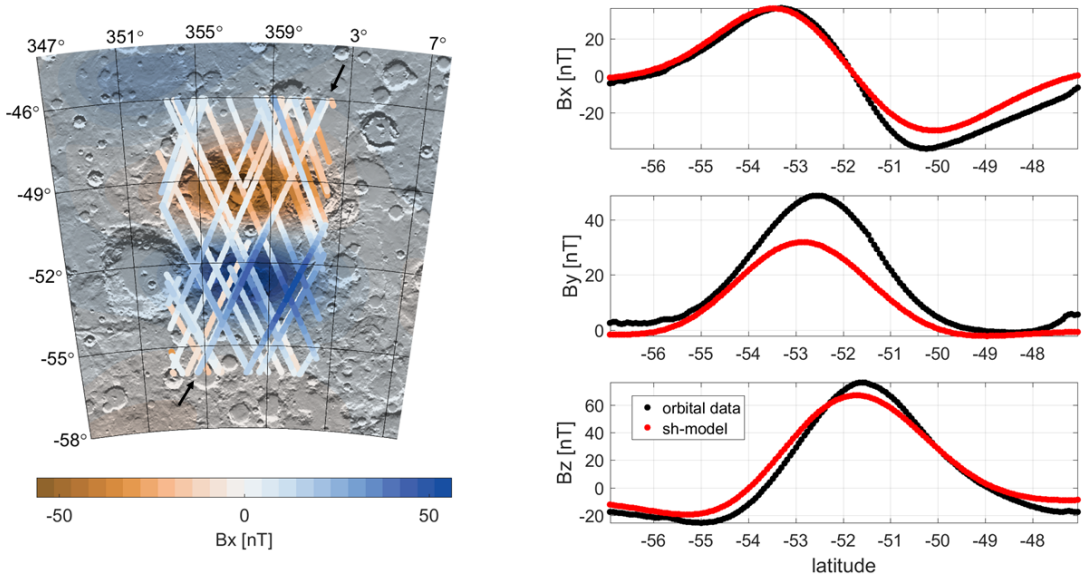

Figure 32: Magnetic fields B_x-component for anomaly A1 at an altitude of 120 km derived from the SH-model, shown on top of a MOLA shaded relief map. MAVEN data tracks in between 116 km and 180 km altitude are plotted on top. The right hand side shows the model (red dotted line) fit to the orbital data (black dotted lines) of the MAVEN spacecraft for one selected track, which is indicated by the black arrows on the left hand side of the figure.

At the location of anomaly A1 39 tracks were selected, with a total of 3160 data points within a square of 10° by 10° around the center of the anomaly (Tab. 5). The lowest data obtained by the MAVEN spacecraft was taken at ~ 116 km altitude. All of the 39 tracks are presented in Fig. 32 on top of the magnetic field derived from the SH-model at 120 km altitude and a shaded topographic map derived from MOLA data. The investigated component is again the magnetic East-component (B_x). The dipole anomaly as identified from the SH-model can clearly be seen in the MAVEN tracks. A detailed analysis of each track reveals that the model fit to the data is generally good at regions of high field intensity, with low relative residuals. As an example the three components of the magnetic field for one track is presented on the right side of Fig. 32, with the tracks location indicated with black arrows on the left side of the same figure. The track starts at 56.9° S / 354° E at an altitude of 116 km and ends at 47° S / 359.5° E at an altitude of 161 km. It can be seen that absolute residuals for the B_x- and B_z-component are usually below 10 nT. The worst fit can be found in the B_y-component with slightly increased residuals up to ~ 15 nT. In comparison, residuals for the B_x-component used in the inversion are below 5 nT (see Sec. 5.2)

The anomaly A2 close to South Crater

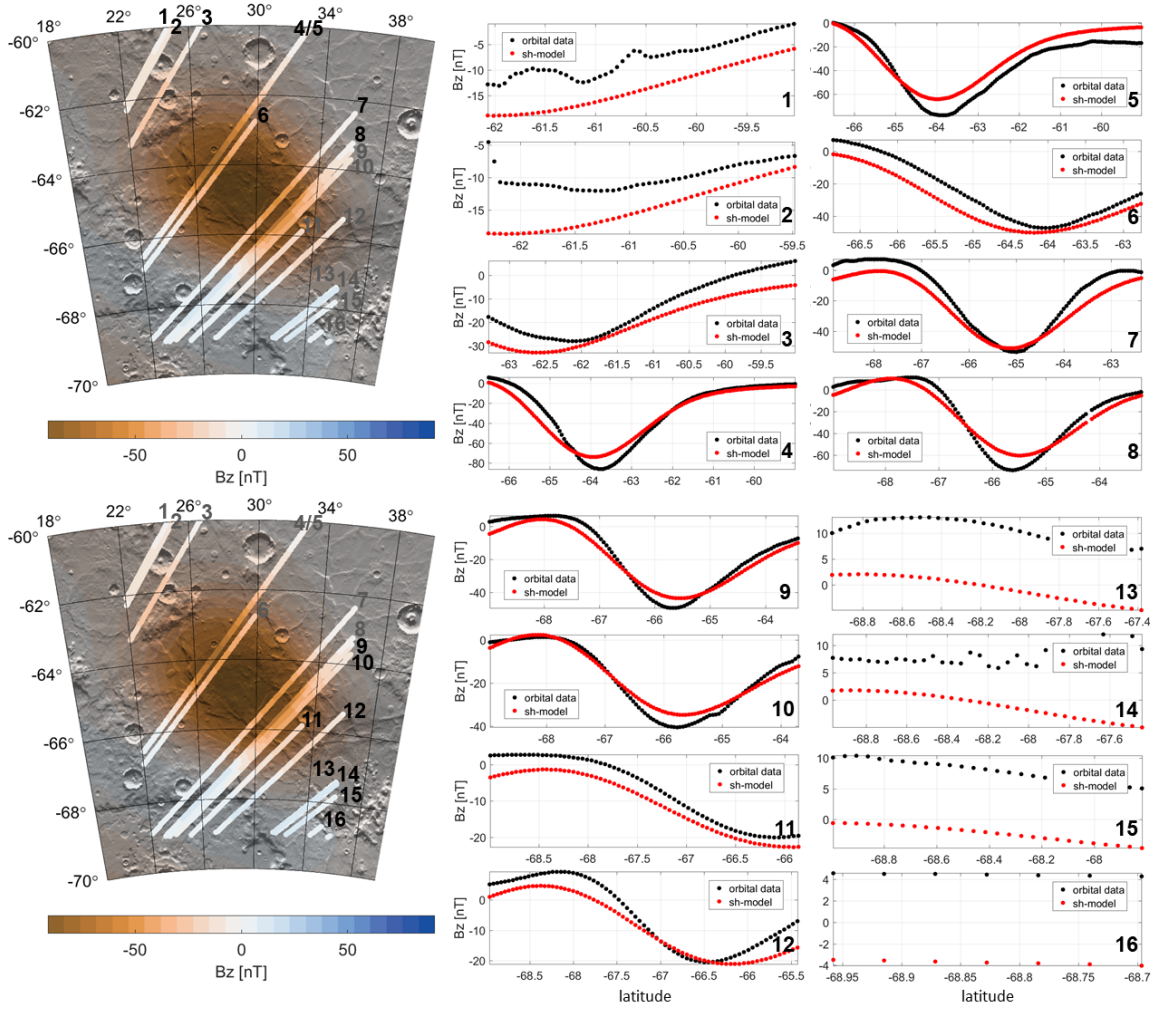

Figure 33: To the left the magnetic fields B_z-component at an altitude of 120 km derived from the SH-model is shown for anomaly A2 on top of a MOLA shaded relief map in combination with 16 orbital tracks measured by the MAVEN spacecraft. The tracks indicated with the black numbers are shown on the right hand side of the figure. The data measured by the MAVEN spacecraft is shown as black dotted line and the magnetic field at the same locations derived from the SH-model is shown in red. It can be seen that the relative misfit increases for regions of low field intensity outside the anomaly, e.g. for tracks 1 to 3 and 13 to 16.

Representative for the investigation of the track misfit inside and outside the anomalies, this section presents all detected tracks in the vicinity of the A2 anomaly and below the altitude of 180 km. This anomaly fits that purpose, because the majority of tracks can visually be separated in a two dimensional graphic and all of the visible tracks cross the anomaly from southwest to northeast (Fig. 33). In total 16 tracks were found with 1255 data points within altitudes of 180 km to ~ 108 km. Starting from the northwest in Fig. 33 the first two tracks (denoted 1 and 2) outside of anomaly A2 clearly show the already mentioned high relative misfit. Within these tracks the MAVEN spacecraft detected only a weak magnetic field between -13 nT and ~ -2 nT (Fig. 33 / black dotted lines). The total misfit to the SH-model is, apart from the two outliers south of $-62°$ at track 2, at maximum 10 nT. This corresponds to a relative misfit of 41% between the SH-model and the orbital data. If now the tracks 4 to 7, which directly cross the anomaly, are investigated

it can be seen that the general misfit of ~ 10 nT persists, but due to the stronger signal in the center of the anomaly the relative misfit decreases.

The strongest field is measured at tracks 4 and 5, reaching −85 nT. Note that track 5 was measured in a higher altitude than track 4 and therefore the maximum field strength is slightly reduced. At the maximum signal of the MAVEN data the calculated magnetic field from the SH-model has residuals of 10 nT at track 4 and ~ 15 nT at track 5. This corresponds to a relative misfit of ~ 12% and ~ 19%, respectively. Comparable relative misfits are calculated for tracks 8, 9, and 10 (Fig. 33), where intensities in between −65 nT and −40 nT are reached. From track 11 and further southeast the relative misfit increases again and changes in polarity appear in the lowest field regions (compare tracks 13 to 16 in Fig. 33). This shows that the fit inside of observed anomalies with high magnetic field intensities are generally good, while misfits increase for regions of low field intensity, but are relatively constant at misfits of ~ 10 nT.

The anomaly A3 close to Tyndall Crater

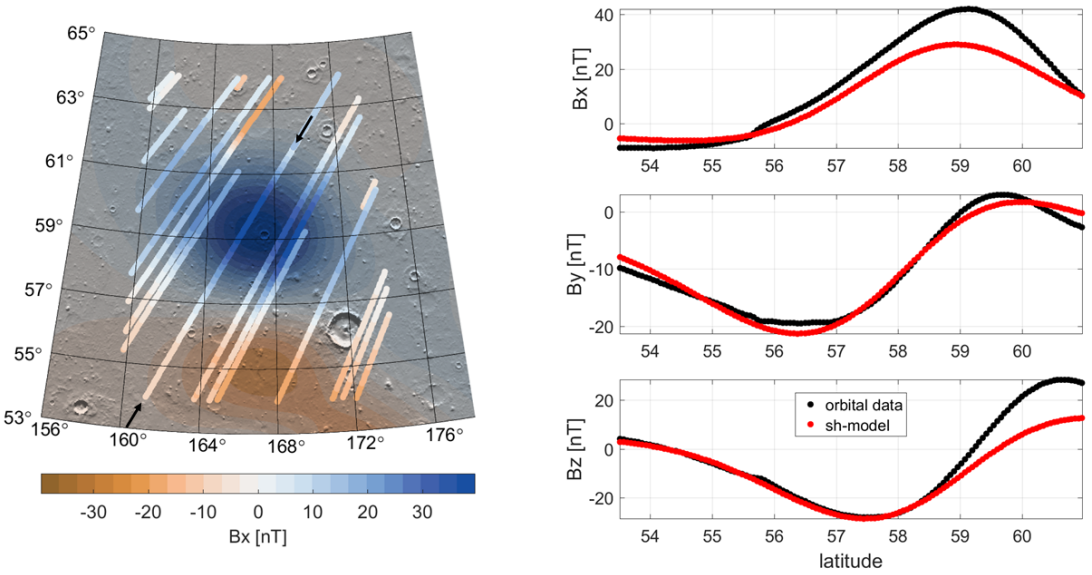

Figure 34: Similar to Fig. 32 but showing the MAVEN measurements close to the Tyndall Crater (A3) at altitudes between 130.5 km and 180 km.

At Tyndall Crater 31 tracks were selected around the center of anomaly A3, of which only 18 can be visually separated. Measurements were taken down to an altitude of 130.5 km with a total of 2777 data points below the altitude of 180 km. Fig. 34 (left) again shows a topographic map of the region as derived from MOLA data and the magnetic field at an altitude of 120 km calculated from the SH-model. On top are the 31 MAVEN tracks, crossing the anomaly from southwest to northeast. Black arrows indicate the location of the track with the three components of the magnetic field shown in detail on the right hand side of the figure. The track starts at 53.5° N / 160.9° E at an altitude of 158 km and ends at 60.9° N / 168.5° E at an altitude of 141.8 km. As for the previous anomalies, the SH-model agrees well with the measured MAVEN data and discrepancies are mostly in amplitude. The relative misfit again is increased in the region of low magnetic field intensity and the absolute misfit is in the range of 10 nT. Different to the anomalies A1 and A2 the smallest misfit is achieved for the B_y-component, while B_x- and B_z-components

show bigger misfits, especially at the edges of the selected tracks. The good correlation of the B_y-component proofs the robustness of the model by Morschhauser et al. (2014), but in fact no new information is gained using this component of the magnetic field. Therefore, the B_x-component is used in the following investigation, just like before with the SH-model.

The anomaly P1 close to Bouguer Crater

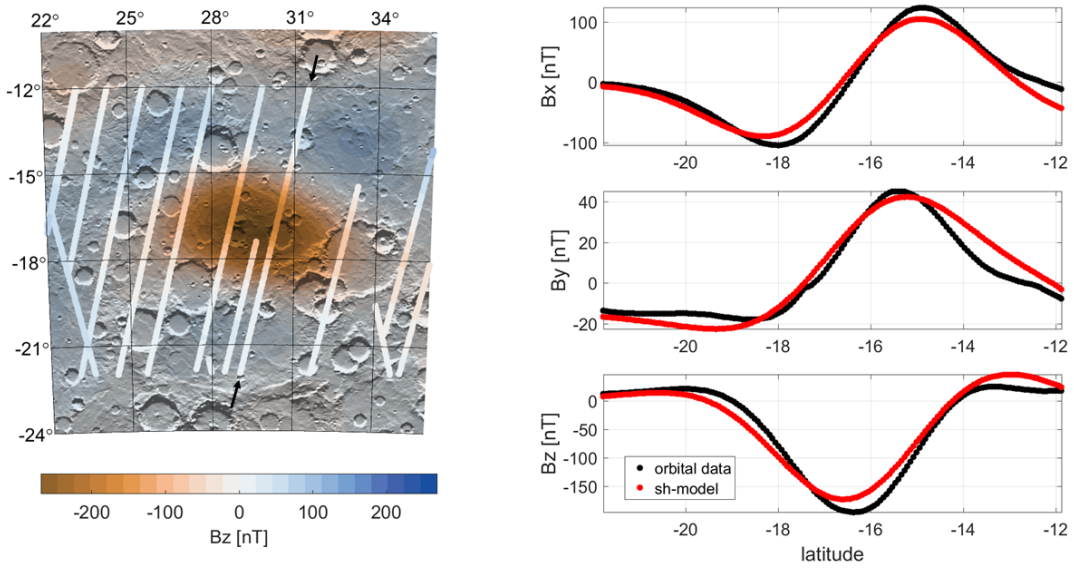

Figure 35: Similar to Fig. 32 but showing a Part of Terra Sabaea at the Bouguer Crater (P1) and the magnetic fields B_z-component. MAVEN data tracks were measured in between 175 km and 132.6 km altitude.

For the anomaly P1 in the vicinity of the Bouguer Crater 2994 data points below the altitude of 180 km were found. The lowest data was measured at the northern edge of the anomaly (11.8° S) at an altitude of ~ 132 km. In the two dimensional presentation of the orbital tracks (Fig. 35 / left hand side) only 14 out of 30 tracks are visible. Additionally to the tracks, Fig. 35 again shows the cratered landscape of Terra Sabaea as calculated from the MOLA data, with the Bouguer Crater at 18.7° S / 27.2° E. The black arrows indicate the track starting from −21.7° / 29.0° E, with an altitude of 175 km and ending at −11.9° / 31.5° E at an altitude of 132.6 km. The three components of the magnetic field of the indicated track are shown on the right hand side of the figure. At latitude −16.3° the orbital data reaches its maximum intensity of −195 nT at an altitude of 147 km (Fig. 35 / black dotted line). The calculated magnetic field from the SH-model only reaches −168.9 nT at this location (Fig. 35 / red dotted line), leading to an absolute misfit of 26.1 nT. This is more than double the misfit calculated for the earlier observed anomalies, but relatively this misfit only corresponds to a difference of 13.4%, which is exactly in the range of previous anomalies. Therefore, the SH-model is in satisfactory agreement to the measured data by the MAVEN spacecraft.

The anomaly P2 in eastern Amazonis Planitia

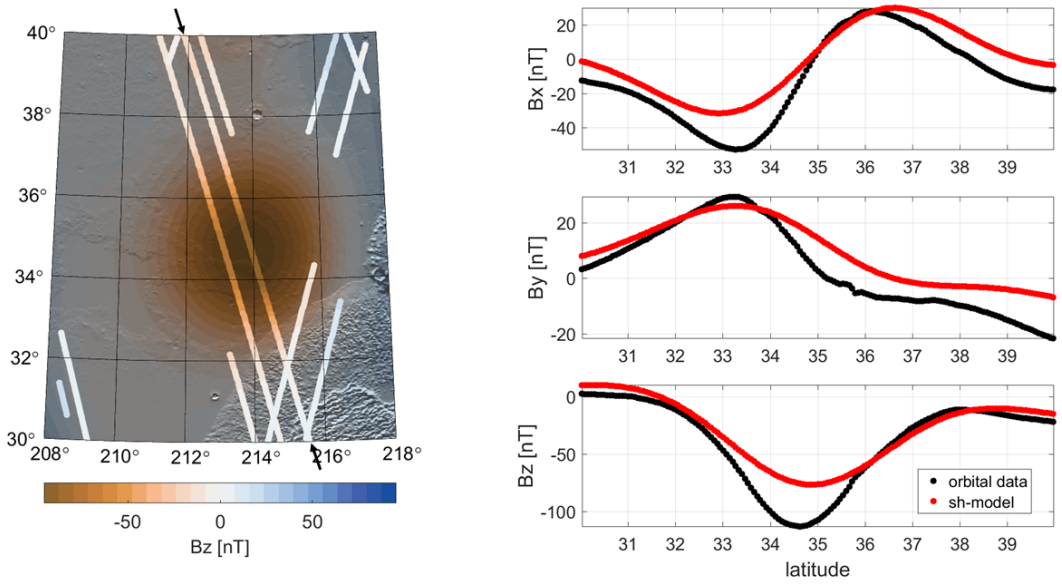

Figure 36: Similar to Fig. 32 but showing anomaly P2 at eastern Amazonis Planitia and the magnetic fields B_z-component. The orbital tracks of the MAVEN spacecraft vary in between altitudes of 180 km to 125 km.

The MAVEN spacecraft passed the eastern Amazonis Planitia and 674 data points were obtained below the altitude of 180 km in the vicinity and directly on top of the anomaly denoted as P2. The tracks are shown on the left hand side of Fig. 36 on top of a MOLA shaded relief map and the magnetic field of the whole region at an altitude of 120 km derived from the SH-model. Within the 12 tracks, data is available down to an altitude of 125 km above the surface. One of this tracks is indicated with black arrows starting at 39.9° N / 211.7° E at an altitude of 137 km and ends at 30.4° N / 215.4° E at an altitude of 140 km. The three components of the vector magnetic field are shown on the right hand side of Fig. 36. Again, it can be seen that the measured magnetic field and the magnetic field derived from the SH-model agree well in terms of the magnetic signal's trend, but high misfits occur between the amplitudes of the compared magnetic fields. For example at 34.6° N the B_z-component as measured by MAVEN has a minimum of -112.9 nT (Fig. 36 / black dotted line). In comparison, the signal derived from the SH-model has a misfit of 37.2 nT and has an intensity of -75.7 nT (Fig. 36 / red dotted line). This corresponds to the highest relative misfit in this study for a region of high field intensity with 33%. Furthermore, a nearly stable offset beginning at $\sim$ 35° N which is mostly in between 10 nT to 12 nT is derived for the B_y-component. Similar offsets can be detected at the edges to the north and south in the trend of the B_x-component. This again shows that differences in between the measured and modeled magnetic fields are stronger in regions of low magnetic field intensity.

Summary

In comparison to MGS the MAVEN data set shows a better spatial resolution below the altitude of 400 km and even 180 km on a global scale, but especially in the regions of the observed anomalies, low altitude data was available prior to the MAVEN mission due to the AB- and SPO-phase of MGS. Moreover, the representative MGS tracks shown in Fig. 21 to 26 are usually below the minimum altitudes reached by the MAVEN spacecraft. Therefore they hold detailed information about the magnetic signals and already obtain good constraints for generating the SH-model. From the detected tracks and calculated misfits between the MAVEN data and the SH-model it can be observed that absolute misfits for all anomalies usually do not exceed 20 nT, but relative misfits increase towards regions of low magnetic field intensity. The highest discrepancies are found at the edges of the observed anomalies. Due to the good fit between the model and MAVEN data it is questionable if inversions will give new insight on the observed anomalies, but it can be expected that the inversion results will agree with the results obtained with the SH-model, depending on the quality of the track fit. The regions of strong magnetic field intensity, which show high correlation, are expected to have the largest influence on the derived magnetic orientations even though misfits towards the edges of the anomalies increase and changes in polarity are present (compare anomaly A2 / Fig. 33).

It was of interest to directly compare the results obtained from the inversions using the SH-model with the inversion results from the MAVEN data, but high altitude variations within the orbital tracks of MAVEN make it impossible to estimate the confidence limit threshold ($\mathbf{I}_{min}$) as explained in Sec. 3.3.3. For this reason, as explained in Sec. 5.4.1, the confidence limit threshold is set to ($\mathbf{I}_{min} = 3 \cdot \sigma_{min}$), which is further used to constrain the modeling results achieved in Sec. 5.4.4. For better comparison between the inversion results of the MAVEN tracks and the SH-model, the magnetic field at the track locations were derived using the SH-model and paleopole investigations were performed for both data sets (Sec. 5.4.4).

5.4.4 *Paleopole investigation from MAVEN data*

As pointed out in Sec. 5.4.3 and by Mittelholz and Johnson (2017), the SH-model shows a generally good correlation to the MAVEN track data with relative misfits below 20% for regions of high magnetic fiel intensity. It can therefore be assumed that performing an inversion on the track data would most likely derive similar paleopole locations and areas of admissible paleopole locations as obtained for a hexagonal distribution of observation points at constant altitude (Sec. 5.2). However, the comparison between MAVEN and the SH-model showed an increasing relative misfit towards the edges of observation for all observed anomalies. This might lead to alterations of the calculated magnetic orientations and to different results for the SH-model and the MAVEN data.

The most insightful comparison would be between the results obtained from the SH-model and the MAVEN track inversions, but as explained in Sec. 5.4.1 and 5.4.3 it is impossible to derive a confidence limit threshold ($\mathbf{I}_{min}$) from the MAVEN tracks, as it was done for the SH-model investigation, due to the altitude variations in the tracks. For this reason, the confidence limit threshold was chosen to be ($\mathbf{I}_{min} = 3 \cdot \sigma_{min}$), similar to the approach shown in Sec. 5.4.1 and 5.4.3. Furthermore, the MAVEN track inversions were repeated using the SH-model to calculate the magnetic field at the locations of the MAVEN tracks. This was done to check if the observation point distribution is responsible for variations in the determined results (compare Sec. 5.5) and to clearly show resulting

deviations between the SH-model and the MAVEN data. In the following Fig. 37 - 41, the derived areas of admissible paleopole locations from the MAVEN tracks are shown as white lines and the best fitting paleopole locations are shown as triangles or inverted triangles of the same color. The corresponding results from the SH-model on the MAVEN track locations are shown in green. All obtained results are summarized in Tab. 9, which lists the anomaly's name (Anomaly), the chosen data (data), the dipole distribution radius (R_0), the STD (σ_{min}), and corresponding confidence limit threshold ($\mathbf{I}_{min}$), as well as the inclination and declination (I/D), best fitting paleopole location (PL) and the surface coverage of the area of admissible paleopole locations (Area).

The anomaly A1 close to Green Crater

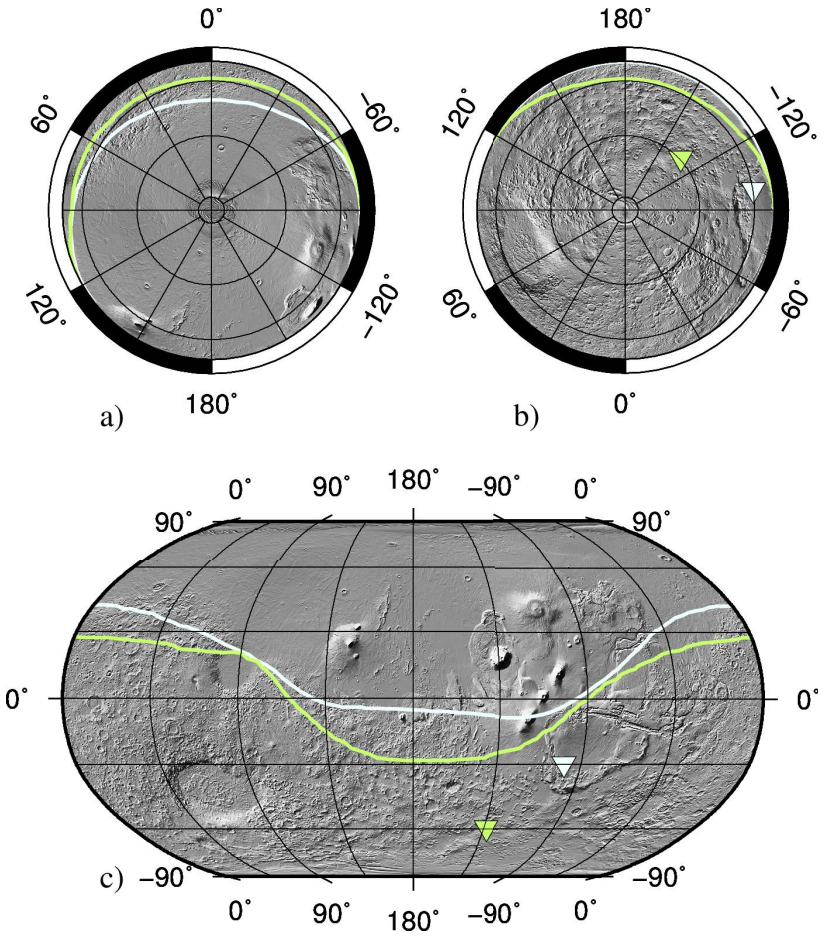

Figure 37: Areas of admissible paleopole locations for anomaly A1 at Green Crater, bound by the confidence limit threshold from MAVEN data (white line) and from the SH-model (green line). The inverted triangles are the locations of the best fitting paleopoles of both investigations and further indicate that admissible paleopole locations are bound south of the printed lines. Data is plotted on top of the Martian topography from MOLA data using spherical projections for the North- (a) and South Pole (b) and a Robinson projection (c) for a global view.

For the Area close to Green Crater 39 tracks at altitudes between 180 km and 116 km were available from MAVEN data. As pointed out in Sec. 5.4.3 the tracks in the center of the anomaly with the highest intensities are generally well fitted by the SH-model and it can be expected that inversion results of the SH-model on the MAVEN track coordinates and the inversion results from the MAVEN data would be similar. Fig. 37 shows the results of both investigations with the derived area of admissible paleopole locations for the

MAVEN data bound by the white line and the area of the SH-model bound by the green line. As indicated by the inverted triangles the majority of admissible paleopole locations point to a paleomagnetic South Pole in the southern hemisphere of Mars. This is consistent with the result obtained in Sec. 5.2. The direct comparison between the SH-model and the MAVEN data shows a best fitting paleopole as derived from the MAVEN data that lies south of the Tharsis rise varying by 29° in latitude and 35° in longitude from the best fitting location calculated from the SH-model (Tab. 9). The area of admissible paleopole locations for both investigations vary by 9%, with the result from MAVEN covering a wide area within the northern hemisphere and being less well constrained than the result from the SH-model.

The anomaly A2 close to South Crater

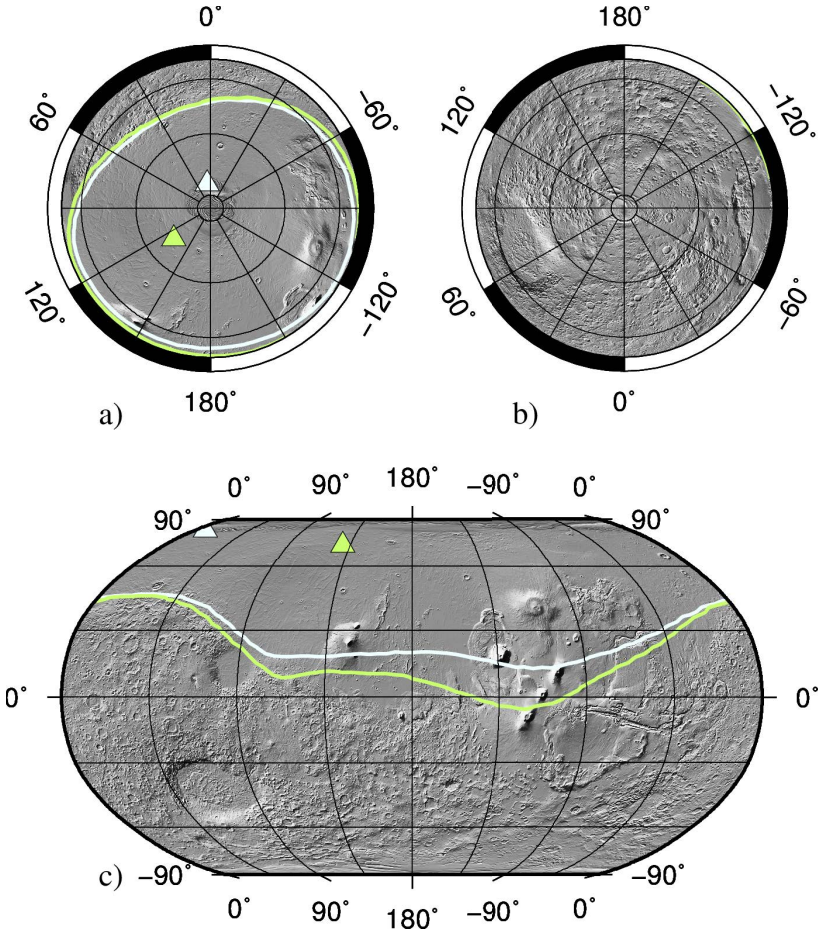

Figure 38: Similar to Fig. 37 but showing anomaly A2 at South Crater and determined admissible paleopole locations in the northern hemisphere.

As presented in Fig. 33 16 tracks were selected for the anomaly A2 close to the South Crater, which cover the anomaly from southwest to northeast at altitudes between 180 km and 108 km. The tracks, denoted 4 - 10, crossing the center of the anomaly have the highest field intensity and the lowest relative misfit (see Sec. 5.4.3). Results from the inversions are listed in Tab. 9. It can be seen that the MAVEN inversion for anomaly A2 is the only one of all anomalies having a lower STD, as well as a better constrained area of admissible paleopole locations, when compared to its corresponding SH-model inversion. The determined area is also the best constrained when compared to any other anomaly, with a surface coverage of only 29%. The areas of admissible paleopole locations are again

shown in white (MAVEN) and green (SH-model) on top of a shaded MOLA topographic relief map (Fig. 38). The upward pointing triangles located at the best fitting paleopole locations (compare Tab. 9) indicate that admissible paleopole locations are located north of the contour lines, which are defined by the confidence limit threshold. For the result obtained for the MAVEN data paleopole locations are therefore constrained to locations north of Ascreus Mons (12° N / 256° E). In comparison, the most southern part of the area of admissible paleopole locations derived from the SH-data nearly reaches Arsia Mons (8° S / 240° E) in the southern hemisphere of Mars.

The anomaly A3 close to Tyndall Crater

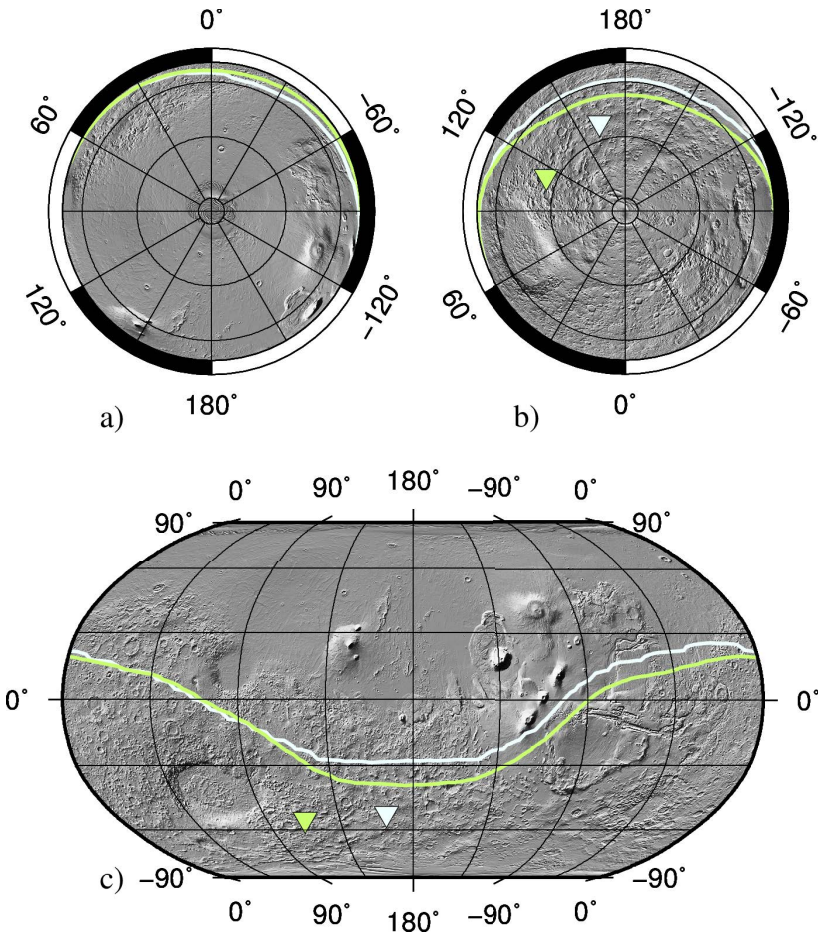

Figure 39: Similar to Fig. 37 but showing anomaly A3 at Tyndall Crater.

As shown in Sec. 5.4.3 the smallest misfit between the MAVEN data and the SH-model was determined for the B_y-component in the central track of the anomaly. This component would therefore gain the least new information. In comparison, the misfit between the MAVEN data and the SH-model is higher for the B_x-component, which is due to the higher intensity of the signal, especially between 58° N and 60° N. This can result in a higher SNR and therefore, similar to the investigation of Sec. 5.2, the B_x-component of the vector magnetic field was used for the inversion with MAVEN data.

The results of the inversions from MAVEN data and the SH-model are shown in Fig. 39 and listed in Tab. 9. The figure shows the derived admissible paleopole locations constrained by the confidence limit threshold on top of a shaded MOLA topographic relief map. In comparison to anomaly A1 the confidence limit threshold again shows

admissible paleopole locations in the southern hemisphere of Mars, but within a smaller range (compare Tab. 9). In total, the area of admissible paleopole locations from A3 is 10% smaller for the MAVEN investigation and 4% smaller for the SH-model investigation when compared to A1. This is in contrast to the results obtained in Sec. 5.2, where the area determined from A1 was 37% smaller than the area from A3. However, if the results of the MAVEN data and the SH-model for anomaly A3 are compared it becomes obvious that the MAVEN data contributes no significant new information for the observed anomaly. The determined best fitting paleopole locations only vary by 3° in latitude and 49° in longitude and the areas of admissible paleopole locations only vary by 3%. Additionally, the determined contour lines in between 0° E and ~ 110° E are congruent and only slightly diverge for increasing longitudes.

The anomaly P1 close to Bouguer Crater

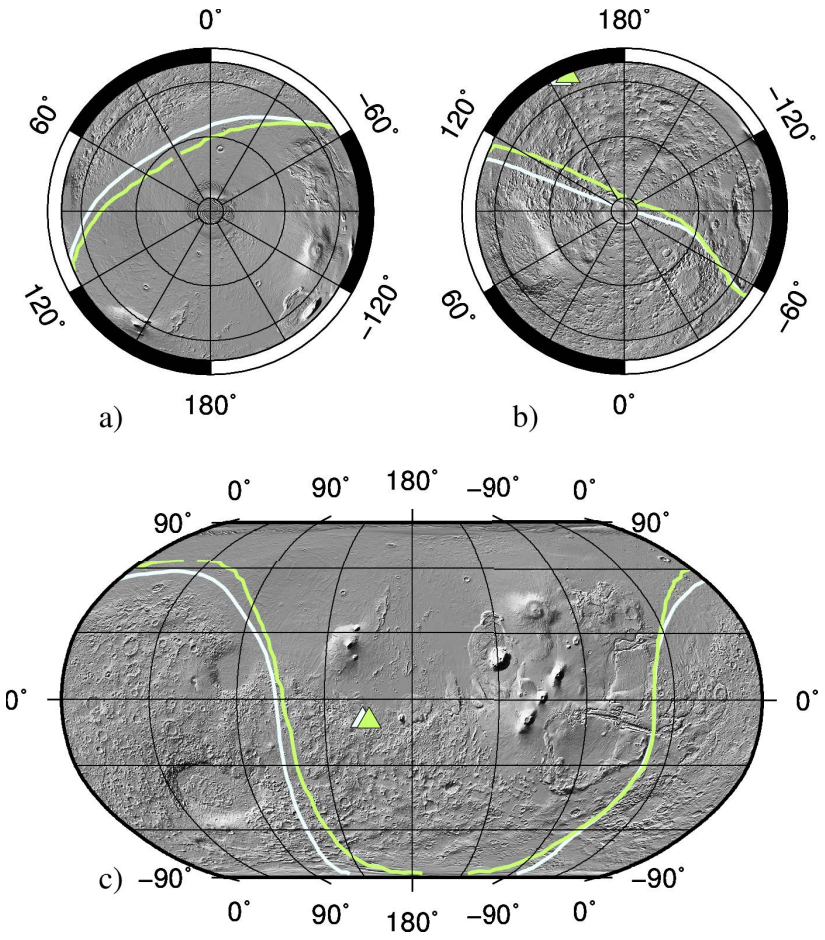

Figure 40: Similar to Fig. 37 but showing anomaly P1 at Bouguer Crater and determined admissible paleopole locations in the northern hemisphere.

Similar to the above investigated anomalies, it was observed for anomaly P1 that the SH-model has high correlation with the MAVEN data. As an example, the central track was shown on the right hand side of Fig. 35. The relative misfit for this track in the B_z-component is only 13.4%. It can therefore be assumed that correlations between the inversion results of MAVEN data and the SH-model exist. In Tab. 9 and Fig. 40 it becomes obvious that high correlations between model and data are indeed present. The determined inclination and declination for both investigations only vary by 3° in inclination and 2° in declination, which leads to nearly the same best fitting paleopole location

at 10° S and 154° E, or 157° E, respectively. The areas of admissible paleopole locations only vary by 2% with the MAVEN result covering 68% of the Martian surface (Fig. 40 / white line) and the result of the SH-model covering 66% of the Martian surface (Fig. 40 / green line). Due to the fact that the whole north polar region from 60° N is included by the confidence limit threshold upward pointing triangles were chosen to indicate that the majority of admissible paleopoles are located in the northern hemisphere, even though the best fitting paleopoles are located in the southern hemisphere. Fig. 40 clearly shows the high correlation between the result obtained for MAVEN data and the SH-model, with congruent contour lines between ~ 280° E and 315° E and only a small increase in the area size for the MAVEN data.

The anomaly P2 in eastern Amazonis Planitia

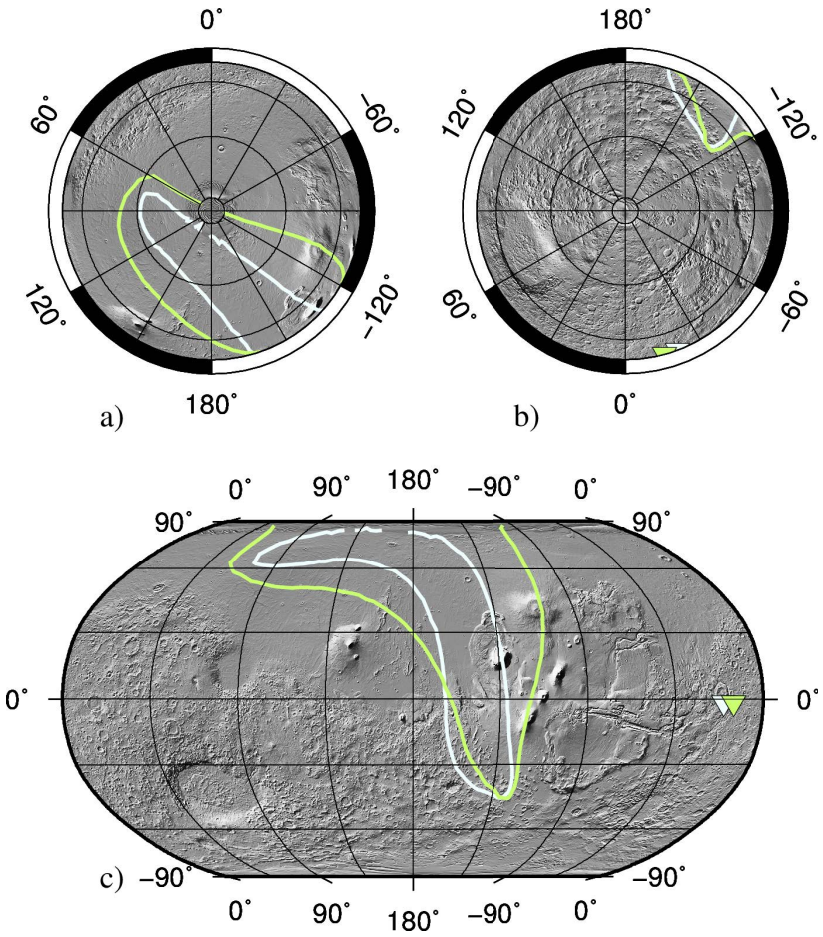

Figure 41: Similar to Fig. 37 but showing anomaly P2 in eastern Amazonis Planitia.

For the anomaly P2 in eastern Amazonis Planitia 12 MAVEN tracks were available in between altitudes of 180 km and 125 km. Additionally, only two tracks fully cross the anomaly within the defined altitude range. One of the tracks, which is presented on the right hand side of Fig. 36, has the highest relative misfit (33%), between the MAVEN data and the SH-model, of all observed anomalies. This could be caused by new information in the MAVEN data and hence could lead to different results from those shown in Sec. 5.2.

The determined inclination and declination and the corresponding paleopole location are shown in Tab. 9 and are very similar for the data and the model. The inclination and declination vary only by 4° and the obtained paleopoles show a difference of 5° in longitude. The determined confidence limit thresholds show a relatively small difference which

leads to areas of admissible paleopole locations of 85% for the MAVEN data and 80% for the SH-model. Anomaly P2 hence results in the least constrained area of admissible paleopoles where only minor regions of the Northern Lowlands and the Tharsis region are excluded as possible paleopole locations. The given areas are contrary to the expected result and it is believed that the less well constrained areas might result from the sparse spatial coverage of the tracks.

Summary

As expected from the similarity of the SH-model and the MAVEN data (Sec. 5.4.3) the direct comparison between inversions of the track data and the model verified that at this stage of research there is no new information to gain from the MAVEN data. The determined areas of admissible paleopole locations for model and track data show high correlation for all observed anomalies. Mostly, the MAVEN results are less well constrained and show areas of admissible paleopole locations which can be 9% bigger than the corresponding areas determined from the SH-model. Only the results obtained for anomaly A2 give better constraints on the area using the MAVEN data.

It can therefore be assumed that an integration of the MAVEN data into a new SH-model would help to further constrain the determined confidence limit threshold when using the method described in Sec. 3.3.3 and thus obtain a smaller area of admissible paleopole locations in the northern hemisphere. The same might apply for anomaly P2. With the integration of the MAVEN data into a SH-model it would be possible to create a more dense spatial coverage for the inversion, which might lead to a better constrained area of admissible paleopole locations here.

The given observations show the robustness of the model by Morschhauser et al. (2014) and they confirm the results obtained in Sec. 5.2 having two anomalies (A1, A3) clearly indicating a former magnetic South Pole in the southern hemisphere and one anomaly (A2) clearly showing a former pole in the northern hemisphere and therefore give evidence that at least once in the evolution of the Martian dynamo a PR took place.

Furthermore, the given calculations from Sec. 5.4.2 using the MGS tracks and this section using the MAVEN data tracks shows the applicability of the presented method for orbital track data. The method can be applied to any orbital data set to reconstruct paleopole locations, but it should be pointed out that the distribution of the data tracks have a high influence on the obtained results and to constrain results a systematic and quantitative method needs to be found.

For this reason, using a planar distribution of data for the inversion, e.g. calculated from a SH-model, should be favoured at this stage.

Table 9: Results for the inversions performed with MAVEN track data and the SH-model at the track locations. Given are the anomaly notation (Anomaly), the used data, the dipole distribution radius (R_0), the calculated STD (σ_{min}), the confidence limit threshold ($\mathbf{I}_{min}$), the determined inclination and declination (I/D), corresponding paleopole location (PL), as well as the area of admissible paleopole locations (Area).

Anomaly	data	R_0	σ_{min} [nT]	$\mathbf{I}_{min}$	I/D	PL	Area [%]
A1	MAVEN	5°	10.5	31.5	35° / 246°	30° S / 261° E	53
A1	SH	5°	2.9	8.7	47° / 206°	59° S / 226° E	44
A2	MAVEN	5°	3.0	9.0	−71° / 354°	80° N / 8° E	29
A2	SH	5°	4.2	12.6	−75° / 42°	71° N / 130° E	35
A3	MAVEN	5°	4.0	12	−33° / 182°	52° S / 163° E	43
A3	SH	5°	3.1	9.3	−48° / 212°	55° S / 114° E	40
P1	MAVEN	3°	22.8	68.4	−49° / 112°	10 S / 154° E	68
P1	SH	3°	13.2	39.6	−52° / 114°	10° S / 157° E	66
P2	MAVEN	4.5°	11.5	34.5	−50° / 68°	2° S / 340° E	85
P2	SH	4.5°	10.5	31.5	−54° / 64°	2° S / 345° E	80

5.5 THE INFLUENCE OF PARAMETER VARIATION

As mentioned in Sec. 1.4, Arkani-Hamed and Boutin (2004) observed in their studies that variations in the chosen source geometry can alter the derived paleopole location up to 15°. Therefore, it was of interest to study if variations in the distribution of the ESDs would influence the resulting paleopole locations and areas of admissible paleopole locations. In fact, the alteration of the paleopole location was first observed during inversions of anomaly A2, using different starting parameters. For this reason various inversions of anomaly A2 were investigated in detail to observe how strong the chosen center location and investigation radius influences the resulting paleopole locations and misfits. The derived center location in dependence of the best SNR (compare Tab. 5) is at 64.5° N / 28.5° E. In the following, dipole distribution radii (R_0) of 3°, 5°, and 10° were tested for this location and for selected locations in the west, north and southeast. For the locations to the west, the center was first shifted 1° W to 64.5° S / 27.5° E and then 2° W to 64.5° S / 26.5° E. For the location to the north, the center was shifted 1° N to 63.5° S / 28.5° E and then 2° N to 62.5° S / 28.5° E, respectively. For the southeast shift the center location was varied by 1° S and 1° E to 65.5° S / 29.5° E (compare Tab. 10).

The first obvious difference in the inversions with different parameters is that the confidence limit threshold depends on the chosen dipole distribution radius (Tab. 10). Here we observe a decrease in $\mathbf{I}_{min}$ with increasing radii. This is a direct consequence of the centralized magnetic field anomaly in combination with the weak field surrounding it. However, the decrease is not surprising given the fact that it was a criteria for selecting the anomalies for paleopole investigations (see Sec. 3.3.3).

Alongside the confidence limit threshold, the derived STDs decrease with increasing R_0 for location alterations to the north. Interestingly, for the center locations in the west and southeast the STD is minimized at $R_0 = 5°$ and increased to nearly twice the minimum at $R_0 = 10°$.

The derived inclinations and declinations and paleopole locations from the best fitting models clearly show the strong differences in the determined results when the center location is varied. For the center locations at 2° N and 1° S / 1° E the derived inclination of the dipoles varies by up to 20°, with the least inclined magnetic orientation at $R_0 = 3°$. For a center location variation of 1° N and the original location (64.5° S / 28.5° E) the inclination varies at maximum 12° between the three R_0-radii and is most stable for the original center location. Even though the declinations are listed in Tab. 10 there is no robust information to gain off them. This is due to the fact that the horizontal components of the magnetic field (B_x and B_y) only weakly contribute to the observed signal, which is evident from the SNR and the derived inclinations. The closer the inclination comes to the value of ±90°, the less the declination can be properly evaluated from the model, because model fits become more or less similar. Furthermore, small changes in declination do not alter the actual location of the paleopole as much as for less inclined magnetic orientations.

However, the differences in the magnetic orientation lead to a wide spread of best fitting paleopole locations. The most northern locations with 88° N are calculated for the original location and 1° S / 1° E of it, with $R_0 = 5°$ and $R_0 = 10°$, respectively. For 2° N center shift and $R_0 = 3°$ a nearly equatorial paleopole location is calculated with 14° N / 219° E, which results in a variation of 68° in latitude when compared to the inversion result from $R_0 = 10°$ at the exact same location and a difference of 74° when compared to the highest latitudes.

Table 10: Results for variation of center location and dipole distribution radius (R_0). The table lists the dislocation from the derived center location of anomaly A2 (compare Sec. 5.1) at 64.5° S / 28.5° E in west, north and southeast direction. Additionally, it lists the average field in the center of observation B_{max}, the confidence limit threshold $\mathbf{I}_{min}$, and corresponding SNR, the derived STD σ_{min}, the inclination and declination (I/D), as well as the paleopole location of the best fitting model (PL) and the areal surface coverage (Area) of all admissible paleopoles.

Dislocation	R_0	B_{max}	$\mathbf{I}_{min}$ [nT]	σ_{min} [nT]	SNR	I/D	PL	Area [%]
0°	3°	90.4	69.8	2.3	1.3/1	−80° / 4°	84° N / 196° E	67
0°	5°	90.4	48.6	0.75	1.9/1	−76° / 4°	88° N / 91° E	65
0°	10°	90.4	6.9	1.1	13.1/1	−78° / 8°	86° N / 159° E	40
1° N	3°	77.9	65.7	2.7	1.2/1	−76° / 196°	38° N / 217° E	63
1° N	5°	77.9	47.6	1.0	1.6/1	−88° / 206°	60° N / 212° E	63
1° N	10°	77.9	6.04	0.59	12.9/1	−81° / 352°	81° N / 223° E	38
2° N	3°	50.7	51.0	3.2	0.9/1	−60° / 194°	14° N / 219° E	60
2° N	5°	50.7	45.8	1.5	1.1/1	−72° / 192°	30° N / 216° E	61
2° N	10°	50.7	7.6	0.38	6.7/1	−80° / 358°	82° N / 213° E	42
1° W	3°	84.4	68.7	2.3	1.2/1	−74° / 40°	71° N / 123° E	67
1° W	5°	84.4	48.9	0.76	1.7/1	−72° / 26°	75° N / 99° E	65
1° W	10°	84.4	6.8	1.3	12.4/1	−79° / 4°	83° N / 161° E	40
2° W	3°	77.3	65.2	2.4	1.2/1	−67° / 52°	59° N / 113° E	67
2° W	5°	77.3	49.0	0.83	1.6/1	−70° / 40°	68° N / 108° E	65
2° W	10°	77.3	7.6	1.4	10.2/1	−78° / 24°	80° N / 141° E	40
1° S / 1° E	3°	66.4	59.1	2.1	1.1/1	−57° / 356°	62° N / 23° E	54
1° S / 1° E	5°	66.4	49.3	0.83	1.3/1	−62° / 356°	68° N / 22° E	54
1° S / 1° E	10°	66.4	12.8	1.6	5.2/1	−76° / 0°	88° N / 30° E	49

Contrary to the changing best fitting locations it can be observed that the shapes of the determind areas of admissible paleopole locations, constrained by their corresponding confidence limit thresholds, are similiar and nearly independent from the chosen parameters (Fig. 42 / 43). The major differences between the parameters appear for the chosen radii R_0. It can be seen in Tab. 10 that σ_{min} and $\mathbf{I}_{min}$ decrease for increasing R_0, resulting in smaller areas of admissible paleopole locations. However, as earlier mentioned the shapes of the determined areas of admissible paleopole locations (Fig. 42 / 43) show only minor changes. This gives further evidence that the determined areas of admissible paleopole locations are the most robust results for the given investigations.

It can further be seen in Tab. 10, Fig. 42, and Fig. 43 that for the investigations with $R_0 = 10°$ latitudes of at least 80° are always determined. The actual center location seems to be of secondary importance, as long as a radius is chosen which covers the whole anomaly and extensive parts of its surroundings. However, the radius is constrained by the presence of perturbing anomalies close by and for small radii it is impossible to neglect the impact of the chosen center location on the determined best fitting location.

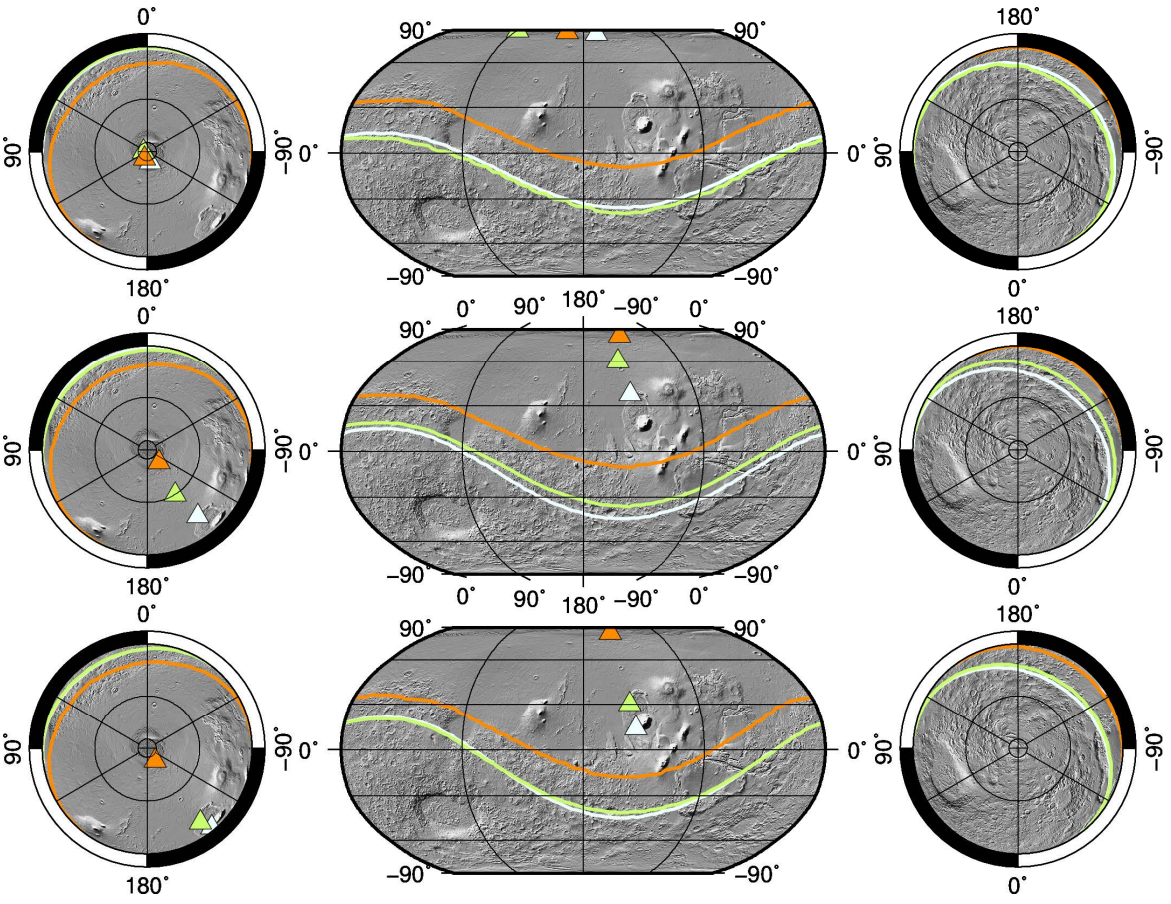

Figure 42: Results of the parameter variations for 0° change (top), 1° change to the north (middle), and 2° change to the north (bottom). In white the area of admissible paleopole locations for a dipole distribution radius of $R_0 = 3°$ is shown. The green and orange contour line bound the areas of admissible paleopole locations for $R_0 = 5°$ (green) and $R_0 = 10°$ (orange), respectively. The triangles further show the locations of the corresponding best fitting paleopoles.

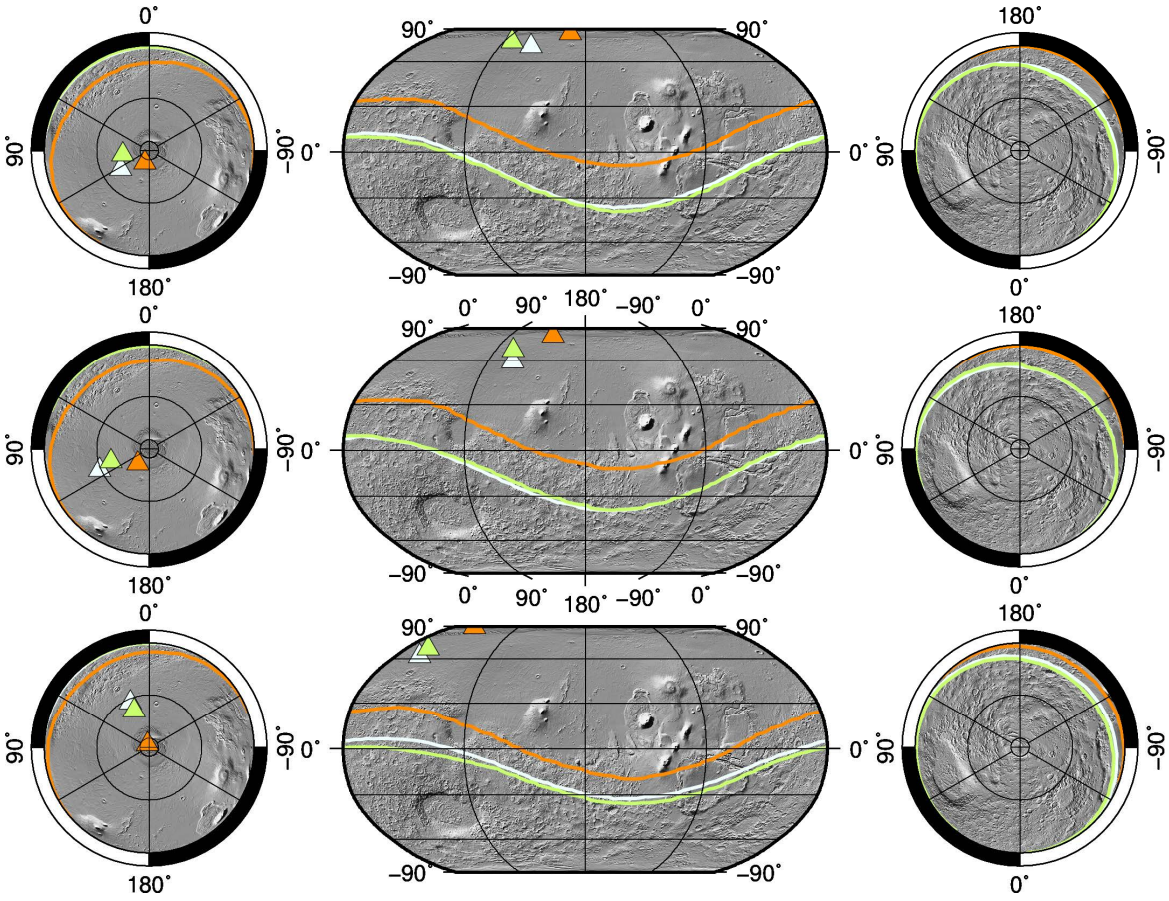

Figure 43: Similar to Fig. 42 results of the parameter variations for 1° change to the west (top), 2° change to the west (middle), and the change of 1° S / 1° E (bottom) are presented.

5.6 ADDITIONAL MAGNETIC FIELD ANOMALIES

For further analysis of the Martian magnetic field a global magnetic field map was generated and visually scanned for potential magnetic field anomalies. In total 18 anomalies were found and their corresponding SNRs were calculated to determine their stage of isolation (see Sec. 3.3.3). Two of these anomalies (P1 and P2) were investigated in more detail in Sec. 5.1 and 5.2. The remaining potential anomalies are listed in Tab. 11. It can be seen that most anomalies do not exceed a SNR of 5/1 and are therefore insufficient candidates for the paleopole inversion. Two anomalies (# 6 and # 12) show a SNR of 6/1, anomaly # 8 has a SNR of 7/1. The highest SNR of 8/1 is determined for # 7, which makes it an appropriate candidate for paleopole investigation according to the investigated anomalies listed in Tab. 5 (Sec. 5.1). For comparison, anomaly # 2 with a SNR of 3/1 was chosen to show the disadvantages of non-isolated anomalies with low SNRs.

Table 11: Summary of observations to determine additional magnetic field anomalies according to their SNR. Listed are the number of the anomaly (#), the location (Location), the dipole distribution radius (R_0) and the respective SNR.

#	Location	R_0	SNR
1	45° N / 65.5° E	9.0°	4/1
2	53.5° N / 313.5° E	9.0°	3/1
3	16.5° S / 14.5° E	3.0°	2/1
4	62° N / 212° E	9.0°	3/1
5	33.5° N / 163° E	4.5°	4/1
6	8.5° N / 75° E	4.0°	6/1
7	5.5° S / 216.5° E	8°	8/1
8	23° S / 39.5° E	4.0°	7/1
9	55.5° S / 18.5° E	7.5°	2/1
10	10.5° S / 138.5° E	5.0°	2/1
11	33.5° N / 214° E	6.5°	5/1
12	47.5° S / 235° E	5.0°	6/1
13	28.5° N / 250.5° E	7.0°	3/1
14	21.5° N / 162.5° E	6.0°	5/1
15	9.7° S / 172.9° E	4.5°	3/1
16	47° N / 166.5° E	4.0°	2/1

Similar to the inversions of Sec. 5.2 the inversions for anomalies # 2 and # 7 were performed as explained in Sec. 3.2, using 241 dipoles distributed at the surface above the anomaly and 241 observation points derived from the SH-model (Morschhauser et al., 2014) at an altitude of 120 km. The magnetic fields B_z-components of both anomalies, at 120 km altitude, are shown in Fig. 44 and 45, respectively. On the left side of Fig. 44 a negative magnetization in an inverted bean-shape with an intensity of around -360 nT in the center of the anomaly can be seen. The figure further shows the downsampled orbital tracks of the MGS-spacecraft between altitudes of 180 km and 90 km and the radius R_0 as red circle. The corresponding average magnetic field values ($\mathbf{I}(R)$) at increasing distance

to the center (see Sec. 3.3.3) are shown on the right hand side of the same figure and it can be seen that a minimum average field is determined at a distance of 8° and the value $\mathbf{I}(8°) = 43.7$ nT defines the confidence limit threshold $\mathbf{I}_{min}$.

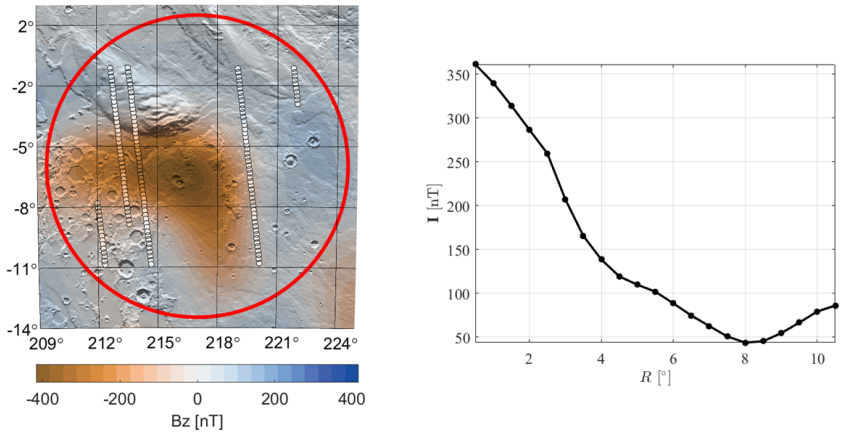

Figure 44: Two different representations of the magnetic field at location 5.5° S / 216.5° E (# 7 / Tab. 11). To the left the magnetic fields B_z-component at 120 km altitude as calculated from the SH-model is shown in combination with the 1 Hz orbital tracks between 90 km and 180 km altitude, on top of a MOLA shaded relief map. Additionally, the dipole distribution radius is shown as red circle. The right side of the figure presents the average magnetic field at distance from the center.

A similar representation is given for anomaly # 2 in Fig. 45. The observed anomaly is much weaker as anomaly # 7 with an intensity of ~ 23 nT at the center of observation. On the right hand side of Fig. 45 it can be seen that a minimum average field of $\mathbf{I}(9°) = 6.9$ nT is determined at a distance of 9°, which is in the following taken as the value for the confidence limit threshold $\mathbf{I}_{min}$.

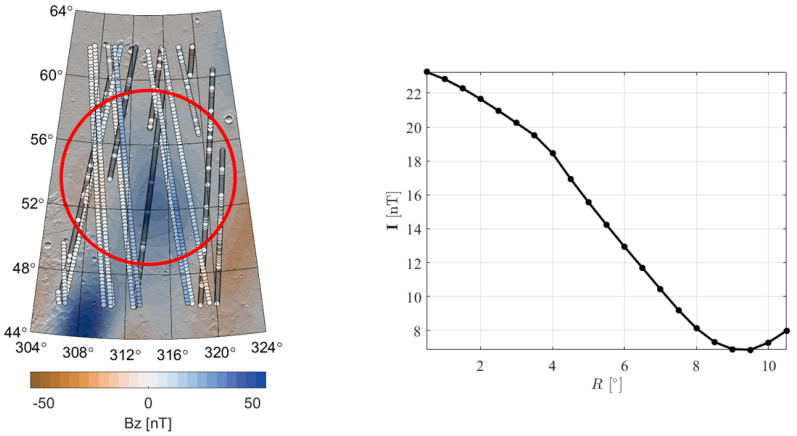

Figure 45: Similar to Fig. 44 but for location 53.5° N / 313.5° E (# 2 / Tab. 11).

The inversion results are listed in Tab. 12. It can be seen that anomaly # 2 has a low misfit to the SH-model with a $\sigma_{min} = 1.8$ nT, but the confidence limit threshold reaches 30% of the anomalies magnetic field intensity and therefore the area of admissible paleopole locations covers 52% of the Martian surface. In comparison, anomaly # 7 has a ten

times higher STD with $\sigma_{min} = 18$ nT, but due to the strong magnetic field the confidence limit threshold corresponds to 12% only, leading to an area of admissible paleopole locations of 23%. The inclination and declination of the best fitting model (Tab. 12) define best fitting paleopole locations for # 2 in the high latitudes of the northern hemisphere and at mid-latitudes for anomaly # 7.

Table 12: Results for the inversion of the crustal magnetic field anomalies # 2 and # 7 of Tab. 11. The calculated STD (σ_{min}), the confidence limit threshold $\mathbf{I}_{min}$, determined inclination and declination (I/D), and corresponding paleopole location (PL), as well as the surface area coverage of admissible paleopole locations (Area) are given.

#	σ_{min} [nT]	$\mathbf{I}_{min}$ [nT]	I/D	PL	Area
2	1.8	6.9	71° / 26°	75°N / 26°E	52%
7	18	43.7	−53° / 238°	23°S / 87°E	23%

Similar to the results obtained in Sec. 5.3 the magnetization strengths M_i of the distributed dipoles can be investigated for anomalies # 2 and # 7. Again, there are less dipoles with a magnetization different from zero than observation points N. Anomaly # 2 has 63 dipoles with a magnetization different from zero (Fig. 46 / left) and anomaly # 7 has 97 dipoles with non-zero magnetization (Fig. 46 / right). The magnetization strength distribution of # 2 shows that the strongest magnetization for this anomaly is far off center at the edge of the dipole distribution. In comparison, anomaly # 7 has its strongest magnetization close to the center with some less strong magnetized dipoles following the shape of the actual anomaly to the west and south (compare Fig. 44 / left side). As pointed out in Sec. 5.3 the centralized localization of dipoles correlates with a high SNR, which is reflected by anomaly # 7 with a SNR of 8/1. On the other hand anomaly # 2 with a SNR of only 3/1 shows the expected off center localization of the strongest magnetization which could already be seen for anomalies P2 and Australe Montes.

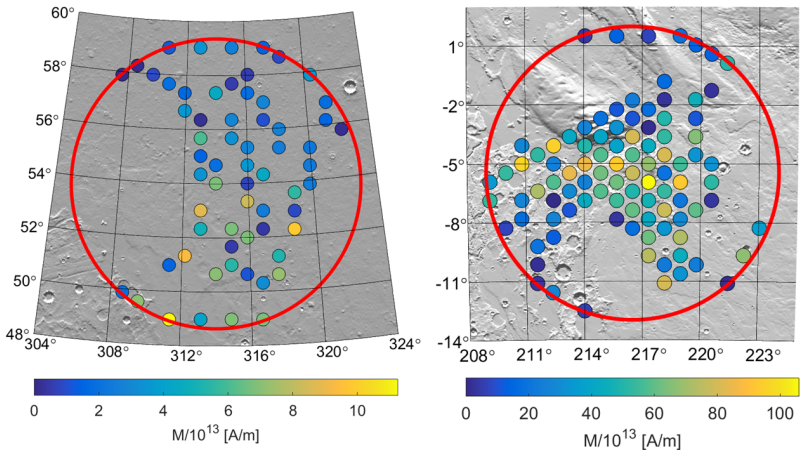

Figure 46: Magnetization strength distributions for anomalies # 2 (left) and # 7 (right), plotted on MOLA shaded relief maps. The red circles indicate the dipole distribution radii (R_0) as listed in Tab. 11. Note that both anomalies have an individual color scale.

The best fitting paleopole locations in combination with the contour lines bounding the areas of admissible paleopole locations for both anomalies are shown in Fig. 47. The white line constrains the area of anomaly # 2 with the best fitting paleopole indicated with

a white triangle. It can be seen that the area covers nearly the whole northern hemisphere as well as a part of the southern hemisphere, up to a latitude of 30° S. It is therefore impossible to constrain the area of admissible paleopole locations for anomaly # 2 to a certain area on the Martian surface and no conclusions can be made regarding PR, or TPW.
On the contrary, the area of admissible paleopole locations constrained by the light-brown line for anomaly # 7 bounds an area in between ~ 65° N and ~ 65° S, excluding the geographic poles of Mars. Similar to the result obtained for anomaly P1 it therefore gives additional evidence for the occurrence of TPW in the history of the Martian dynamo.

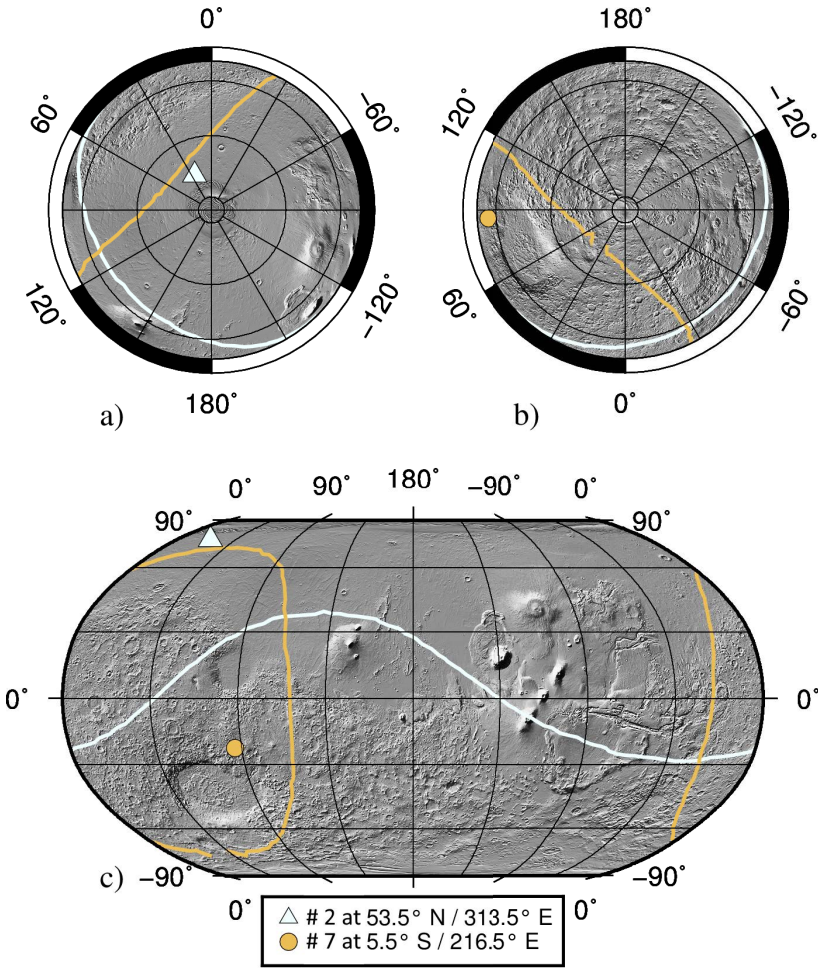

Figure 47: Admissible paleopole locations for anomalies # 2 and # 7. Shown are the area bounding contour lines in white (# 2) and light-brown (# 7) in combination with the best fitting locations (see Tab. 12) in the same color. The white triangle indicates admissible paleopole locations with a preference to the northern hemisphere, while the light-brown circle indicates admissible paleopole locations at mid-latitudes. Part c of the figure shows a global Robinson projection, while a and b show a spherical North and South Pole projection, respectively.

In conclusion, this comparative analysis showed that the resulting area of admissible paleopole locations obtained from anomaly # 2 with low SNR is not applicable for paleopole investigations, because admissible paleopoles cover more than 50% of the planetary surface. It can be assumed that areal coverage decreases for anomalies # 1, # 5, # 6, # 8, # 11, # 12, and # 14 as it was shown by investigating # 7. However, all of the anomalies listed in Tab. 11 have SNRs below 10/1 which was set as an optimal SNR to ensure a certain stage of isolation. Therefore, non of these anomalies, except # 7 and # 8, are worth to investigate in more detail with the available data.

Part IV

INTERPRETATION

In the final part of this thesis the findings from the previous chapters are combined to give an estimate of the Martian dynamo evolution. At the end of this part an outlook for possible upcoming investigations and necessary observations is given.

6

INTERPRETING THE MAGNETIZATION MODELS OF MARTIAN MAGNETIC FIELD ANOMALIES

In this chapter the results of the thesis are discussed and it is explained how an estimate of the reversal period can be made when the crustal magnetic field anomalies are put into a geo-chronological context. Therefore, anomalies are dated based on estimated surface ages at the locations of observation. Finally, an outlook for future campaigns is given to determine source ages and further constrain areas of admissible paleopole locations.

6.1 SUMMARY

As explained in detail in Ch. 1 a terrestrial planet holds the ability to generate a global main magnetic field when dynamo processes are present in the outer core of the planet. There is strong evidence that planet Mars possessed a global main magnetic field in its past (Acuña et al., 1999; Connerney et al., 2001; Gubbins and Herrero-Bervera, 2007; Lillis et al., 2013; Weiss et al., 2002), which deceased around 4.1 Ga ago (Lillis et al., 2013; Vervelidou et al., 2017b). During its lifetime the main magnetic field interacted with magnetizable minerals in the Martian crust. Eventually the magnetic orientation and a fracture of the magnetic intensity of the main field was preserved as remanent magnetization in some minerals within the crust. Today, these minerals hold the only record of the former main magnetic field of Mars and can be observed in order to estimate former magnetic pole locations (paleopoles).

Several investigations were performed (compare Sec. 1.4) to determine magnetic paleopole locations on Mars. The comparison of these investigations showed that paleopole locations appear nearly randomly distributed all over the Martian surface and it was of interest to explain the wide spread of locations and estimate a measure of uncertainty for determined paleopole locations.

More often the measured data provides the uncertainty of a given data set. For this reason in Ch. 2 we looked into magnetic field measurements in general and how the magnetic field of Mars was measured, processed, and used to generate a global SH-model. The latter played a key role for the investigations of this thesis.

For investigating paleopole locations it is necessary to reconstruct the magnetic orientation of the source of the observed magnetic anomaly. Usually the important parameters, such as shape, size, mineral composition and depth of the source body are unknown or vague. Therefore, most paleopole investigations use simple shaped source bodies and vary depth and size in order to determine a best fitting model (compare Tab. 1). However, as explained in Ch. 3 (Sec. 3.1) a certain magnetic signal can be generated by an infinite number of variations of the three parameters size, depth and shape, not even mentioned other major parameters like the mineral content (Blakely, 1996; Telford et al., 1990). It is therefore a reasonable approach to choose a method with less variables and the least constraints possible (Vervelidou et al., 2017a) in order to minimize the impact of the chosen parameters on the results.

For this thesis the method of Parker (1991) was implemented, because no assumptions concerning depth, size or shape of the source body are necessary. Instead, the method uses

a regular distribution of dipoles (ESD) on the surface above the anomaly, which synthesize the magnetic source. It was assumed that the observed anomalies formed within a period with stable main magnetization and therefore all dipoles are uniformly aligned. To avoid constraints originating from a specific dipole distribution all dipoles were distributed on a hexagonal grid, resulting in an equally distanced distribution pattern. By modeling the magnetic field for every possible magnetic orientation a best fitting model can be determined and a confidence interval is automatically generated from the remaining models (Sec. 3.2).

It was an objective of this study to determine a limit for the confidence interval, in order to reduce the number of admissible models, and therefore obtain an area of admissible paleopole locations. In Sec. 3.3 it is shown how such a confidence limit threshold could be simply calculated from the covariance matrix of the given SH-model. However, as explained in Sec. 3.3.1 the covariance matrix obtained either too small constraints, resulting in no model that fitted, or too large constraints, that all models were admissible.

In the next attempt it was observed if an error ellipsoid for the magnetic field components can be determined in order to obtain models that fit the ellipsoid and models that lie outside of the ellipsoid (Sec. 3.3.2). Due to the fact that the generation of the error ellipsoid is based on the covariance matrix it occurred that all models fitted the longest semi-major axis of the ellipsoid, but not the shortest.

It was then analyzed if a confidence limit threshold can be defined from the physical parameters of the observed magnetic field. In fact, no natural magnetic anomaly is perfectly isolated and perturbing fields are always present. In Sec. 3.3.3 it was evaluated if a measure of uncertainty can be found by observing the magnetic field in the vicinity of observation. Therefore, annuli of increasing radii were created around the anomaly and the mean magnetic field within each annulus was calculated. The obtained mean magnetizations were then compared to the magnetization in the center of observation to obtain the SNR of each annulus. The annulus which maximized the SNR defined the radius for the dipole and observation point distribution, under which the observed magnetic source is least influenced by perturbations. The mean magnetization which maximized the SNR was then taken as the confidence limit threshold to constrain the number of admissible models.

Using synthetic anomalies the influence on the measured signal and therefore the determined magnetic orientation from random noise (Sec. 4.2) and perturbation from an anomaly in the vicinity of observation (Sec. 4.3) was tested. It was shown that random noise below 5% can be neglected, while random noise of 10% already increases the area of admissible paleopole locations to 25%. The perturbation test showed that the influence of the perturbing anomaly is decreased with increasing distance to the observed anomaly. Random noise and perturbing magnetic fields are possible influences in orbital magnetic field surveys and the results of the model tests fit the deviations found in earlier investigations. Furthermore, the model uncertainty obtained from perturbation is always reflected as an increase in STD and the obtained confidence limit threshold. Therefore, the presented method is applicable for a broad selection of magnetic field anomalies.

In order to further constrain admissible paleopole locations it is an objective of future studies to focus on isolated anomalies, because only then admissible paleopole locations with a surface coverage below 25% can possibly be determined. To achieve this goal more detailed magnetic field data, preferably measured at low altitudes, is required.

The method to determine suitable magnetic field anomalies for paleopole investigations, was applied to the Martian magnetic field using the SH-model by Morschhauser et al. (2014). The majority of tested anomalies provided insufficient SNRs (Sec. 5.6). However, eight anomalies were investigated in detail in Sec. 5.1, 5.2, and 5.6. The inversion results revealed admissible paleopole locations in the high southern hemisphere for anomaly A1, as well as admissible locations over nearly the entire southern hemisphere for anomaly A3. In contrast, anomalies A2 and Australe Montes constrain admissible paleopole locations to the northern hemisphere of Mars. In addition, the inversion result of anomaly P1 reveals an area constrained to latitudes below $\pm 60°$ and # 7 an area constrained to $\pm 65°$, respectively. The admissible paleopole locations for anomalies P2 and # 2 are the least constrained and spread over wide regions on the southern and northern hemisphere. However, anomalies A1, A2, A3, and Australe Montes give clear evidence for at least one PR prior to 4.1 Ga. Furthermore, the determined areas of admissible paleopole locations from anomalies P1 and # 7 (Sec. 5.6) give evidence for a TPW scenario, which has changed the polar axis by at least 25°. This is in agreement with Kite et al. (2009), suggesting a TPW of less than 60° and is similar to the estimated maximum TPW of 25° by Bouley et al. (2016) and Murray and Malin (1973). Additionally, the 113° difference in longitude between P1 and # 7 implicates a PR after the TPW event.

The determined areas of admissible paleopole locations for the investigated anomalies reflect the wide spread found in earlier studies (Fig. 4) and agree with Arkani-Hamed and Boutin (2004) and Biswas and Ravat (2005), who determined paleopole variations of 15° and up to 50° by parameter variation and natural scatter, respectively (Sec. 1.4). The investigations shown in Sec. 4 support these findings and it is concluded that the spread found in earlier studies can partially be explained by signal alteration due to neighboring fields (coalescence effect).

It was further shown that simple parameter variations, such as choosing a different center location can cause a variation of the derived best fitting paleopole of more then 50° (Biswas and Ravat, 2005). The test presented in Sec. 5.5 gives a clear example for the robustness of the derived confidence interval in comparison to the calculated best fitting paleopole location, which is strongly altered due to e.g. variations in the chosen center location, or dipole distribution radius. In this particular example the latitude of the derived paleopole could vary by 74°, only due to the change of the center location of the investigation. It was observed that the influence of the chosen center location is negligible if a big enough dipole distribution radius can be chosen. But distribution radii are constrained by the magnetic field in the vicinity of observation and radii can not be increased unrestrained.

Furthermore, it was shown in Fig. 42 and 43 that the areas of admissible paleopole locations increase in dependence of the chosen parameters, but the actual geometry remains nearly similar and gives the most robust result. It can therefore be concluded that in order to obtain robust paleopole locations from orbital magnetic field data, reporting a single paleopole location is insufficient, unless a measure of uncertainty is given.

After new low altitude magnetic field data became available from the MAVEN spacecraft it was observed if further insight on the Martian magnetic field anomalies can be gathered from e.g. higher resolutions of regions with low magnetic field intensity. Therefore, it was first tested if the presented method is capable to determine paleopole locations from orbital tracks alone (Sec. 5.4.1). This was done by generating synthetic tracks with the magnetic field derived from the SH-model. The tracks showed an inclination, so that the altitude varied from end to end. Due to the inclination it was not possible to determine

a confidence limit threshold as in Sec. 3.3.3, but based on the results obtained in Sec. 5.2 confidence limit thresholds were estimated to be $\mathbf{I}_{min} = 3 \cdot \sigma_{min}$. It was revelaed that the obtained results from the synthetic track investigations agree with the results obtained in Sec. 5.2 if at least two tracks are available for the inversion. Further tests were performed with the along track data from MGS (Sec. 5.4.2) and apart from anomaly P2 results similar to the results of the SH-model were achieved. This investigations could already show that orbital track data can be used for paleopole investigations. But, the chosen tracks, their distribution and especially their data quality influence the obtained results.

Before the MAVEN data was used for paleopole investigations, the fit between the SH-model and the MAVEN data was observed. It was shown that the relative misfits increase with decreasing field intensity, but in general the model fits the data well. However, using the confidence limit threshold of $\mathbf{I}_{min} = 3 \cdot \sigma_{min}$ track data paleopole investigations were performed (Sec. 5.4.4). For better comparison each anomaly was investigated with the MAVEN data and with the magnetic field calculated from the SH-model at MAVEN's track locations. The obtained results show similar areas of admissible paleopole locations for all anomalies, which leads to the conclusion that no further insight on the Martian magnetic field anomalies can be obtained from MAVEN's track data.

Still, integrating MAVEN data into a SH-model will increase the accuracy in comparison to the model by Morschhauser et al. (2014) and could lead to further constraints on the areas of admissible paleopole locations. Generating a SH-model from MGS and MAVEN data should therefore be the next step in future investigations.

6.2 POLE MOVEMENT OF THE FORMER MARTIAN MAGNETIC FIELD

In order to estimate the ages of the investigated magnetic sources a reliable correlation between, e.g. a datable crater or volcanic structure to a magnetic anomaly would be the optimal scenario. From the investigated anomalies shown in Sec. 5.1 non can be linked to a topographic feature. Even though anomaly Australe Montes is named after the Australe Montes volcano it is uncertain if the measured magnetic field signal is related to the volcanic edifice. Given the magnetic anomaly in Fig. 24 and the derived dipoles in Fig. 28 it seems likely that the anomaly is a result of various sources underneath the surface.

The only estimate for the source ages of all observed anomalies can therefore be given by the ages of the surface layer above the anomaly. From the geologic map of Tanaka et al. (2014) (App. B) it can be inferred that anomaly A1 is located underneath a middle Noachian ($3.95 - 3.84$ Ga) highland unit at Noachis Terra. Anomaly A2 is located underneath a late Noachian ($3.84 - 3.7$ Ga) volcanic unit in Malea Planum. The anomalies A3 and Australe Montes are both located underneath Hesperian units, but the surface age of A3 can be constrained to the late Hesperian ($3.4 - 3.0$ Ga), while the surface at Australe Montes belongs to the Hesperian polar edifice unit, which can only roughly be dated from early to late Hesperian ($3.7 - 3.0$ Ga). Located underneath the middle Noachian ($3.95 - 3.84$ Ga) highland unit, within Terra Sabaea, lies anomaly P1. It is surrounded by an early Noachian highland unit, as well as Amazonian and Hesperian impact units in the southeast and late Noachian highland units in the north and northwest. The anomaly # 2 is located in Acidalia Planitia, under the Late Hesperian Lowland unit ($3.4 - 3.0$ Ga), but it will not be taken into account in following, due to its uncertain result. Anomaly # 7 is located in Daedalia Planum with an Amazonian and Hesperian unit in the center and to the east, the Amazonian and Hesperian transition undivided unit to the north and a middle Noachian highland unit to the west. If the source age of this anomaly is somehow

related to the surface age, it can only be dated between ~ 3.8 Ga to ~ 3.0 Ga. Due to the wide range in age it will also not be taken into account in the following. The youngest surface age corresponds to anomaly P2, which is located underneath Amazonian and late Amazonian (3.0 Ga till today) volcanic units.

Taken the surface ages and excluding # 2 and # 7, the chronological order of the investigated anomalies from oldest to youngest would be: 1. A1, P1; 2. A2; 3. Australe Montes; 4. A3; 5. P2. With the determined paleopole locations Mars would have had a magnetic South Pole on the southern hemisphere between $3.95 - 3.84$ Ga ago, maybe followed by a TPW event or vice versa. Then a PR occured between $3.84 - 3.7$ Ga ago, followed by a period of stagnant orientation while the Australe Montes anomaly formed ($3.7 - 3.0$ Ga). Then another PR occured in the time between $3.4 - 3.0$ Ga and the magnetic orientation is lost for anomaly P2 in the Amazonian.

As discussed in Sec. 1.2.1, there is strong evidence for a decrease in the magnetic field strength prior to 4.1 Ga (Lillis et al., 2013; Vervelidou et al., 2017b). A relation between the surface ages and source ages of the investigated anomalies is therefore implausible. Unlike Earth, where detailed marine magnetic surveys and sample investigations revealed that polarity changes can appear with frequencies of 20k years (Gubbins and Herrero-Bervera, 2007) it is not possible to make an estimate for a magnetic reversal period for Mars from the available data. Furthermore, after Garland (1979) the proof of an alternating field lies in the correlation of magnetized samples from different areas, different ages and different magnetic orientations. However, the constraints within this statement are only valid for Earth, because on Earth a magnetization of opposing orientation can be achieved by tectonic movement. Mars has no plate tectonics (Spohn et al., 2014), therefore a reversed magnetization is only possible due to a full reversal of the main magnetic field (Garland, 1979; Tarling, 2007) and the results obtained in this thesis give evidence for at least one full reversal of the Martian magnetic field.

6.3 OUTLOOK

A key objective for future investigations is to provide constraints for estimating the source ages of magnetization. A possible scenario could be the detection of weak magnetization within low altitude data at dateable topographic structures, such as volcanoes, or craters. For this investigations it is necessary to measure low altitude magnetic field data for example with an automatized drone or a rover. Both vehicles would need to perform measurements covering a specific area and not only measure single tracks on their way over the Martian surface.

A more accurate procedure to measure the magnetic orientation and intensity of a magnetic anomaly is to directly measure these parameters in a rock sample of the anomaly's source material. For this purpose a sample would be collected at a site, with a detailed record of its orientation in space. Then a so called spinner magnetometer (Tarling, 2007) could be used to determine the magnetic orientation and finally an isotope analysis would provide the age of the sample.

A spinner magnetometer in general consists off a rotating platform surrounded by a pick-up coil. The rock sample is placed on the platform and spun, leading to a current which is induced in the pick-up coil. The amplitude of the signal depends on the intensity of the sample's magnetization and on the magnetization perpendicular to the rotational axis, in particular. The magnetic orientation in the perpendicular plane to the rotational axis is then determined from the phase angle. In dependence of the magnetic

moment it takes 2 to 20 min to obtain the magnetic orientation and intensity of the remanent magnetic field of the sample and with standard systems, e.g. using fluxgate ring pick-up coils, it is possible to measure the absolute value of the magnetic moment down to $|\vec{m}| = 5 \cdot 10^{-10} \mathrm{Am}^2$. The sensitivity and measurement time can be further increased using cryogenic magnetometers, such as **SQUID**s (**S**uperconducting **QU**antum **I**nterference **D**evice).

Using this technique at different locations on Mars could reduce the areas of admissible paleopole locations, from some 10 percent of the Martian surface, to maybe 1% and below. This would help to obtain further constraints on the Martian dynamo and its evolution. However, such an investigation is cost- and power-intensive, because the necessary tasks can only be performed by astronauts, or complex rovers. A rover would need to carry a device to extract a rock sample, the spin magnetometer as well as an isotope counter for the age estimation. Furthermore, in order to obtain a geo-evolutionary context, the rover or the astronauts need to collect data at different sites all over the planet. Therefore, this kind of detailed investigation will most probably not be performed in the near future.

Part V

APPENDIX

A

NONNEGATIVE LEAST SQUARE FIT IN PSEUDO CODE

Most of the calculations in this thesis were performed using MATLAB language. In some cases it was possible to save time because scripts already existed which were able to perfom the needed tasks. One example is the implemented function to solve nonnegative least squares (lsqnonneg.m). The complex program will in the following be explained in steps using pseudo code (Lawson and Hanson, 1974) to highlight important features of the calculation. For calculation the matrix $\mathbf{G}_2$ (Eq. 3.2.10) with the size K by N and the magnetic field vector $\mathbf{B}$ with length K are used. Further, a K-vector f and two N-vectors $\mathbf{w}$ and $\mathbf{z}$, which provide working space, are defined.
The algorithm is then initialized by first defining two index sets $P = 0$ and $Z = \{1, 2, ..., N\}$ which will be modified while the code is executed.

1. Set $P = 0$ / $Z = \{1, 2, ..., N\}$ / $\mathbf{M} = 0$
2. Compute the N-vector $\mathbf{w} = \mathbf{G}_2^T (\mathbf{B} - \mathbf{G}_2\mathbf{M})$
3. If Z is empty, or $\mathbf{w}_j \leqslant t$ for all $j \in Z$ go to step 12
4. Find an index $t \in Z$ that $\mathbf{w}_j = \max\{\mathbf{w}_j\}$ for $j \in Z$
5. Add t to P and remove it from Z
6. Let now $\mathbf{G}_P$ denote the K by N matrix defined by

$$\text{Column } j \text{ of } \mathbf{G}_P = \begin{cases} \text{column } j \text{ of } \mathbf{G}_2 & \text{if } j \in P \\ 0 & \text{if } j \in Z \end{cases}$$

   compute another N-vector $\mathbf{z}$ as a solution of the least squares problem $\mathbf{G}_P = f$. Only the components $\mathbf{z}_j$ for $j \in P$ are determined by this problem and $\mathbf{z}_j = 0$ for $j \in Z$
7. If $\mathbf{z}_j > 0$ for all $j \in P$ set $\mathbf{M} = \mathbf{z}$ and go to step 2
8. Find an index $q \in P$ that $\mathbf{M}_q/(\mathbf{M}_q - \mathbf{z}_q) = \min$ with $\mathbf{z}_j \leqslant 0$ and $j in P$
9. Set $\alpha = \mathbf{M}_q/(\mathbf{M}_q - \mathbf{z}_q)$
10. Set $\mathbf{M} = \mathbf{M} + \alpha(\mathbf{z} - \mathbf{M})$
11. Move from set P to set Z for all indices $j \in P$ for which $\mathbf{M}_j = 0$ and go to step 6.
12. Computation is complete

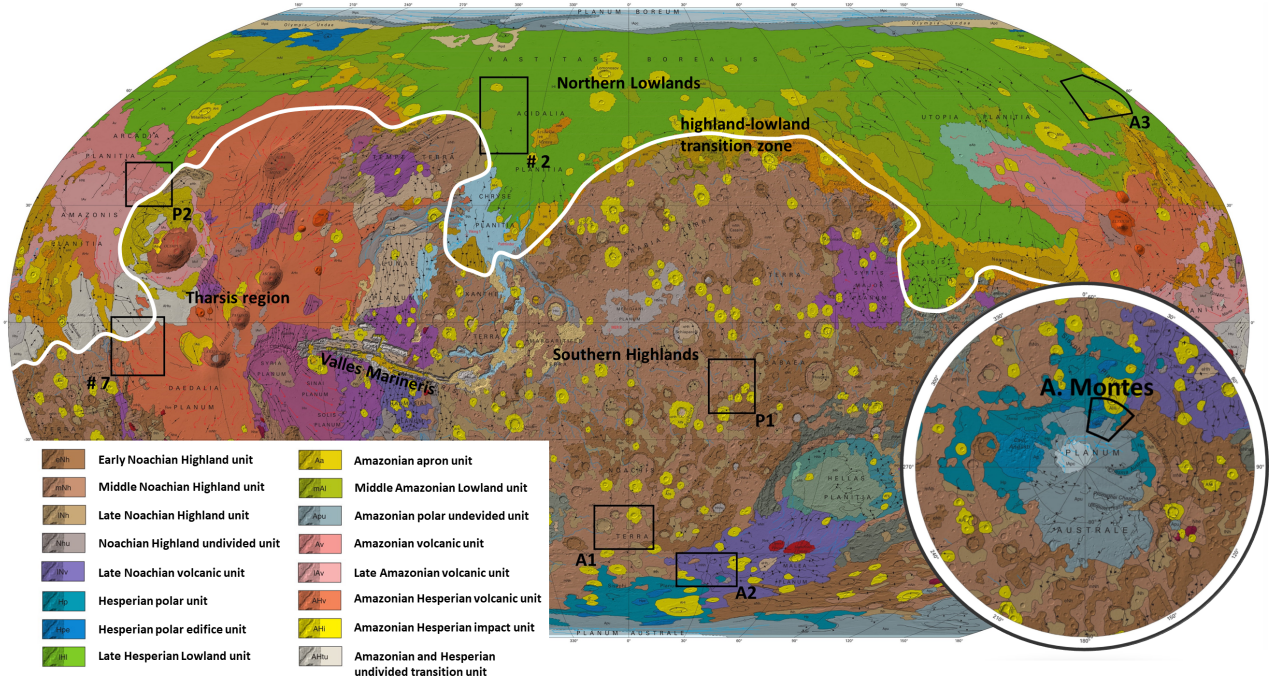

Figure 48: Clip of the geologic map of Mars from Tanaka et al. (2014). Areas of observation for the anomalies A1, A2, A3, Australe Montes, P1, P2, as well as # 2 and # 7 are bound with black lines. The Martian dichotomy is roughly indicated with the white line.

BIBLIOGRAPHY

Acuña, M. H., J. E. P. Connerney, P. Wasilewski, R. P. Lin, K. A. Anderson, C. W. Carlson, J. McFadden, D. W. Curtis, H. Rème, and A. Cros (1992). "Mars Observer magnetic fields investigation." In: *J. Geophys. Res.* 97, pp. 7799–7814.

Acuña, M. H., J. E. P. Connerney, N. F. Ness, R. P. Lin, D. Mitchell, C. W. Carlson, J. McFadden, K. A. Anderson, H. Rème, C. Mazelle, D. Vignes, P. Wasilewski, and P. Cloutier (1999). "Global Distribution of Crustal Magnetization Discovered by Mars Global Surveyor MAG/ER Experiment." In: *Science* 284, pp. 790–793.

Acuña, M. H., J. E. P. Connerney, P. Wasilewski, R. P. Lin, D. Mitchell, K. A. Anderson, C. W. Carlson, J. McFadden, H. Rème, C. Mazelle, S. J. Bauer D. Vignes, P. Cloutier, and N. F. Ness (2001). "Magnetic field of Mars: Summary of results from aerobraking and mapping orbits." In: *J Geophys. Res.* 106, pp. 23403–23418.

Akalin, F., D. D. Morgan, D. A. Gurnett, D. L. Kirchner, D. A. Brain, R. Modolo, M. H. Acuna, and J. R. Espley (2010). "Dayside induced magnetic field in the ionosphere of Mars." In: *Icarus* 206, pp. 104–111.

Andrews-Hanna, J. C., M. T. Zuber, and W. B. Banerdt (2008). "The borealis basin and the origin of the Martian crustal dichotomy." In: *Nature* 453, pp. 1212–1215.

Arkani-Hamed, J. (2001a). "A 50-degree spherical harmonic model of the magnetic field of Mars." In: *J. Geophys. Res.* 106(E10), pp. 23197–23208.

— (2001b). "Paleomagnetic Pole Positions and Pole Reversals of Mars." In: *Geophys. Res. Lett.* 27(17), pp. 3409–3412.

— (2002). "An improved 50-degree spherical harmonic model of the magnetic field of Mars derived from both high-altitude and low-altitude data." In: *J. Geophys. Res.* 107(E10), p. 5083.

— (2004). "A coherent model of the crustal magnetic field of Mars." In: *J. Geophys. Res.* 109 (E09005).

Arkani-Hamed, J. and D. Boutin (2004). "Paleomagnetic poles of Mars." In: *J. Geophys. Res.* 109 (E03011).

Aster, R. C., B. Borchers, and C. H. Thurber (2013). *Parameter Estimation and Inverse Problems*. 2nd. Oxford, UK: Elsevier.

Berckhemer, H. (1997). *Grundlagen Der Geophysik*. 2nd. Darmstadt, GER: Wissenschaftliche Buchgesellschaft.

Biswas, S. and D. Ravat (2005). "Why Meaningful Paleopoles Can't Be Determined Without Special Assumptions From Mars Global Surveyor Data?" In: *Lunar Planet. Sci. Con.* XXXVI, # 2192.

Blakely, R. J. (1996). *Potential Theory in Gravity and Magnetic Applications*. 1st. Cambridge, UK: University Press.

Bouley, S., D. Baratoux, I. Matsuyama, F. Forget, A. Séjourné, M. Turbet, and F. Costard (2016). "Late Tharsis formation and implications for early Mars." In: *Nature* 531, pp. 344–347.

Boutin, D. and J. Arkani-Hamed (2006). "Pole wandering of Mars: Evidence from paleomagnetic poles." In: *Icarus* 181, pp. 13–25.

Brain, D. A., F. Bagenal, M. H. Acuna, and J. E. P. Connerney (2003). "Martian magnetic morphology: Contribution from the solar wind and crust." In: *J. Geophys. Res.* 108 (No. A12, 1424).

Butler, R. F. (1992). *Paleomagnetism: Magnetic Domains to Geologic Terranes*. 1st. Oxford: Blackwell Science.

Cain, J. C., B. B. Ferguson, and D. Mozzoni (2003). "An n = 90 internal potential function of the Martian crustal magnetic field." In: *J. Geophys. Res.* 108 (No. E2, 5008).

Citron, R. I. and S. Zhong (2012). "Constraints on the formation of the Martian crustal dichotomy from remanent crustal magnetization." In: *Physics of the Earth and Planetary Interiors* 212, pp. 55–63.

Connerney, J. E. P., M. H. Acuna, P. J. Wasilewski, G. Kletetschka, N. F. Ness, H. Rème, R. P. Lin, and D. L. Mitchell (2001). "The global magnetic field of Mars and implications for crustal evolution." In: *Geophys. Res. Lett.* 28 (21), pp. 4015–4018.

Connerney, J. E. P., J. R. Espley, P. Lawton, S. Murphy, J. Odom, R. Oliversen, and D. Sheppard (2015a). "The MAVEN Magnetic Field Investigation." In: *Space Sci Rev* 195, pp. 257–291.

Dietrich, W. and J. Wicht (2013). "A hemispherical dipole model: Implications for the Martian crustal magnetization." In: *Physics of the Earth and Planetary Interiors* 217, pp. 10–21.

Dunlop, D. J. and J. Arkani-Hamed (2005). "Magnetic minerals in the Martian crust." In: *J. Geophys. Res.* 110 (E12).

Echer, E., W. D. Gonzalez, B. T. Tsurutani, and A. L. C. Gonzalez (2008). "Interplanetary conditions causing intense geomagnetic storms (Dst $\leqslant$ -100 nT) during solar cycle 23 (1996-2006)." In: *J. Geophys. Res.* 113 (A05221).

Echer, E., B. T. Tsurutani, and W. D. Gonzalez (2013). "Interplanetary origins of moderate (-100 nT < Dst < -50 nT) geomagnetic storms during solar cycle 23 (1996-2008)." In: *J. Geoph. Res.* 118, pp. 385–392.

Frawley, J. J. and P. T. Taylor (2004). "Paleo-pole positions from Martian magnetic anomaly data." In: *Icarus* 172, pp. 316–327.

Garland, G. D. (1979). *Introduction to Geophysics*. 2nd. Toronto, CA: W. B. Saunders Company.

Gubbins, D. and E. Herrero-Bervera (2007). *Encyclopedia of Geomagnetism and Paleomagnetism*. 1st. Dordrecht, NL: Springer.

Hood, L. L. and K. Hartdegen (1997). "A crustal magnetization model for the magnetic field of Mars: a preliminary study of the Tharsis region." In: *Geophys. Res. Lett.* 24, pp. 727–730.

Hood, L. L. and A. Zakharian (2001). "Mapping and modeling of magnetic anomalies in the northern polar region of Mars." In: *J. Geophys. Res.* 106, pp. 601–609.

Hood, L. L., N. C. Richmond, E. Pierazzo, and P. Rochette (2003). "Distribution of crustal magnetic fields on Mars: Shock effects of basin-forming impacts." In: *Geophys. Res. Lett.* 30(6), p. 1281.

Hood, L. L., C. N. Young, N. C. Richmond, and K. P. Harris (2005). "Modeling of major Martian magnetic anomalies: Further evidence for polar reorientations during Noachian." In: *Icarus* 177, pp. 144–173.

Hood, L. L., N. C. Richmond, K. P. Harris, and R. J. Lillis (2007). "East west trending magnetic anomalies in the Southern Hemisphere of Mars: Modeling analysis and interpretation." In: *Icarus* 191, pp. 113–131.

Jacobshagen, V., J. Arndt, H. J. Götze, D. Mertmann, and C. M. Walfass (2000). *Einführung in die geologischen Wissenschaften*. 1st. Stuttgart, GER: Verlag Eugen Ulmer.

Jakosky, B. M., R. P. Lin, J. M. Grebowsky, D. F. Mitchell J. G. Luhmann, G. Beutelschies, T. Priser, M. Acuna, L. Andersson, D. Baird, D. Baker, R. Bartlett, M. Benna, and S. Bougher et al. (2015). "The Mars Atmosphere and Volatile Evolution (MAVEN) Mission." In: *Space Sci. Rev.* doi: 10.1007/s11214-015-0139-x.

Kertz, W. (1985). *Einführung in die Geophysik II*. 2nd. Mannheim, GER: Hochschultaschenbücher.

Kite, E. S., I. Matsuyama, M. Manga, J. T. Perron, and J. X. Mitrovica (2009). "True Polar Wander driven by late-stage volcanism and the distribution of paleopolar deposits on Mars." In: *Earth and Plan. Sci. Lett.* 280, pp. 254–267.

Kletetschka G., and J. E. P. Connerney, N. F. Ness, and M. H. Acuna (2004). "Pressure effects on Martian crustal magnetization near large impact basins." In: *Meteor. Planet. Sci.* 39, pp. 1839–1848.

Kopitzki, K. (1989). *Einführung in die Festkörperphysik*. 3. Stuttgart, GER: Teubner Studienbücher: Physik.

Langlais, B. and M. E. Purucker (2006). "A polar magnetic paleopole associated with Apollinaris Patera, Mars." In: *Planet. Space Sci.* 44, pp. 270–279.

Langlais, B., M. E. Purucker, and M. Mandea (2004). "Crustal magnetic field of Mars." In: *J. Geoph. Res.* 109 (E02008).

Lawson, C. L. and R. J. Hanson (1974). *Solving Least Squares Problems*. 1st. Englewood Cliffs, New Jersey: Prentice-Hall, pp. 160–165.

Lewis, K. W. and F. J. Simons (2012). "Local spectral variability and the origin of the Martian crustal magnetic field." In: *Geoph. Res. Lett.* 39 (L18201).

Lillis, R. J., S. Robbins, M. Manga, J. S. Halekas, and H. V. Frey (2013). "Time history of the Martian dynamo from crater magnetic field analysis." In: *J. Geoph. Res., Planets* 118, pp. 1488–1511.

Lowrie, W. (2007). *Fundamentals of Geophysics*. 2nd. Cambridge, UK: University Press, pp. 281–359.

Marinova, M. M., O. Ahoronson, and E. Asphaug (2008). "Mega-impact formation of the Mars hemispheric dichotomy." In: *Science* 453, pp. 1216–1219.

Mayhew, M. A. (1979). "Inversion of satellite magnetic anomaly data." In: *Geophys. J.* 45, pp. 119–128.

Meschede, D. (2005). *Fundamentals of Geophysics*. 23rd. Berlin Heidelberg, Germany: Springer, pp. 353–398.

Milbury, C. and G. Schubert (2012). "Search for the global signature of the Martian dynamo." In: *J. Geophys. Res.* 115 (E10010).

Mittelholz, A. and C. L. Johnson (2017). "Crustal Magnetic Fields on Mars from MAVEN Data." In: *Lunar and Planet. Sci. Con.* XLVII, #1674.

Mohit, P. S. and J. Arkani-Hamed (2004). "Impact demagnetization of the Martian crust." In: *Icarus* 168, pp. 305–317.

Morschhauser, A., V. Lesur, and M. Grott (2014). "A spherical harmonic model of the lithospheric magnetic field of Mars." In: *J. Geophys. Res., Planets* 119, pp. 1162–1188.

Murray, B. C. and M. C. Malin (1973). "Polar wandering on Mars." In: *Science* 179, pp. 997–1000.

Musmann, G. and Y. Afanassiev (2009). *Fluxgate Magnetometers for Space Research*. 1st. Norderstedt: Books on Demand GmbH, pp. 10–12.

Nimmo, F. and M. S. Gilmore (2001). "Constraints on the depth of magnetized crust on Mars from impact craters." In: *J. Geophys. Res.* 106(E6), pp. 12315–12324.

Nimmo, F., S. D. Hart, D. G. Korycansky, and C. B. Agnor (2008). "Implications of an impact origin for the Martian hemispheric dichotomy." In: *Nature* 453(7199), pp. 1220–1223.

Oliveira, J. and M. A. Wieczorek (2017). "Testing the axial dipole hypothesis for the Moon by modeling the direction of crustal magnetization." In: *J. Geophys. Res. Planets* 122, pp. 383–399.

Parker, R. L. (1975). "The Theory of ideal Bodies for Gravity Interpretation." In: *Geophys. J. R. astr. Soc.* 42, pp. 315–334.

— (1991). "A Theory of ideal Bodies for Seamount Magnetism." In: *J. Geophys. Res.* 96, pp. 16101–16112.

Plattner, A. and F. J. Simons (2015). "High-resolution local magnetic field models for the Martian South Pole from Mars Global Surveyor data." In: *J. Geophs. Res., Planets* 120, pp. 1543–1566.

Quesnel, Y., B. Langlais, and C. Sotin (2007). "Local inversion of magnetic anomalies: Implication for Mars' crustal evolution." In: *Planet. Space Sci.* 55, pp. 258–269.

Quesnel, Y., C. Sotin, B. Langlais, S. Costin, M. Mandea, M. Gottschalk, and J. Dyment (2009). "Serpentinization of the Martian crust during Noachian." In: *Earth Planet. Sci. Lett.* 277, pp. 184–193.

Rochette, P., G. Fillion, R. Ballou, F. Brunet, B. Ouladdiaf, and L. Hood (2003). "High pressure magnetic transition in pyrrhotite and impact demagnetization on Mars." In: *Geophys. Res. Lett.* 30(13), p. 1683.

Rochette, P., J. Gattacceca, V. Chevrier, V. Hoffmann, J. P. Lorand, M. Funaki, and R. Hochleitner (2005). "Matching Martian crustal magnetization and magnetic properties of Martian meteorites." In: *Meteoritics & Planetary Science* 40(4), pp. 529–540.

Ruiz, J. (2009). "The very early thermal state of Terra Cimmeria: Implications for the magnetic carriers in the crust of Mars." In: *Icarus* 203, pp. 454–459.

Ruiz, J., P. J. McGovern, and R. Tejero (2006). "The early thermal and magnetic state of the cratered highlands of Mars." In: *Earth Planet. Sci. Lett.* 241, pp. 2–10.

Spohn, T., D. Breuer, and T. V. Johnson (2014). *Encyclopedia of the Solar System*. 3rd. Oxford, UK: Elsevier.

Stanley, S., L. Elkins-Tanton, M. T. Zuber, and E. M. Parmentier (2008). "Mars' Paleomagnetic Field as the Result of a Single-Hemisphere Dynamo." In: *Science* 321, pp. 1822–1825.

Tanaka, K. L., J. A. Skinner, J. M. Dohm, R. P. Irwin, E. J. Kolb, C. M. Fortezzo, T. Platz, G. G. Michael, and T. M. Hare (2014). "Geologic Map of Mars." In: *U.S. Geological Survey Scientific Investigations Map 3292* scale 1:20,000,000.

Tarling, D. H. (2007). *Palaeomagnetism: Principles and Applications in Geology, Geophysics and Archeology*. 2nd. New York, USA: Chapman and Hall, pp. 181–190.

Telford, W. M., L. P. Geldart, and R. E. Scheriff (1990). *Applied Geophysics*. 2nd. Cambridge, UK: University Press, pp. 522–531.

Thomas, P., M. Grott, A. Morschhauser, and F. Vervelidou (2018). "Paleopole reconstruction of Martian magnetic field anomalies." In: *J. Geophys. Res.: Planets* 123, pp. 1140–1155.

Vervelidou, F., V. Lesur, A. Morschhauser, M. Grott, and P. Thomas (2017a). "On the accuracy of paleopole estimations from magnetic field measurements." In: *Geophys. J. Int.* 211, pp. 1669–1678.

Vervelidou, F., V. Lesur, A. Morschhauser, and R. Lillis (2017b). "Constraining the date of the Martian dynamo shutdown by means of crater magnetization signatures." In: *J. Geophys. Res.* 122 (E005410).

Weiss, B.P., H. Vali, F. J. Baudenbacher, J. L. Kirschvink, S. T. Stewart, and D. L. Shuster (2002). "Records of an ancient Martian magnetic field in ALH84001." In: *Earth Plan. Sci. Lett.* 201, pp. 449–463.

Wilhems, D. E. and S. W. Squyres (1984). "The Martian hemispheric dichotomy may be due to a giant impact." In: *Nature* 309, pp. 138–140.

LIST OF FIGURES

LIST OF TABLES

ABBREVIATIONS

AB	Aerobraking
AL	aligned
Ch.	Chapter
CL	center location
CRM	chemical-remanent magnetization
DLR	Deutsches Zentrum für Luft- und Raumfahrt
DRM	detrital-, or depositional-remanent magnetization
EMF	electromotive force
ESD	Equivalent Source Dipole
Fig.	Figure
MAG	Magnetometer
MAVEN	Mars Atmosphere and Volatile Evolution
MGS	Mars Global Surveyor
MOLA	Mars Orbiter Laser Altimeter
MPO	Mapping Phase Orbit
PDS	Planetary Data System
PL	paleopole location
PR	polar reversal
Sec.	Section
SH	spherical harmonic
SNR	signal to noise ratio
SPO	Science Phase Orbit
SQUID	Superconducting Quantum Interference Device
SRM	shock-remant magnetization
STD	standard deviations
Tab.	Table
TPW	true polar wander
TRM	thermo-remanent magnetization